

A Densified Binder-jet Printed Powder System Via Viscous-Rearrangement Assisted Sintering

by

Chuyuan Zheng

B.S., University of Pittsburgh, 2016
B.S., Sichuan University, China, 2016

Submitted to the Graduate Faculty of the
Swanson School of Engineering in partial fulfillment
of the requirements for the degree of
Doctor of Philosophy

University of Pittsburgh

2022

UNIVERSITY OF PITTSBURGH

SWANSON SCHOOL OF ENGINEERING

This dissertation was presented

by

Chuyuan Zheng

It was defended on

April 4, 2022

and approved by

Jung-Kun Lee, Ph.D., Professor, Department of Mechanical Engineering and Materials Science

Markus Chmielus, Ph.D., Associate Professor, Department of Mechanical Engineering and
Materials Science

Anthony Rollett, Ph.D., Professor, Carnegie Mellon University

Dissertation Director: Ian Nettleship, Ph.D., Associate Professor, Department of Mechanical
Engineering and Materials Science

Copyright © by Chuyuan Zheng

2022

A Densified Binder-jet Printed Powder System Via Viscous-Rearrangement Assisted Sintering

Chuyuan Zheng, Ph.D.

University of Pittsburgh, 2022

Binder-jet 3D printing (BJ3DP) is a non-beam based additive manufacturing technology that can fabricate stress-free metal and ceramic parts with great production efficiency. One of the major challenges for BJ3DP is the consolidation of as-printed green bodies. In preliminary work, gas-atomized Inconel 625 alloy was binder-jetted and isothermal sintered under subsolidus and supersolidus temperatures. Quantitative analyses on 2D sections suggested that under supersolidus sintering, rapid particle rearrangement occurred with the help of a viscous liquid phase, which collapsed large printing defects and facilitated densification. Based on the preliminary results, a new two-step viscous liquid rearrangement assisted (VRA) sintering process was proposed to efficiently densify printed 625 alloy while preventing heavy elemental segregations caused by liquid phase formation in supersolidus sintering. Three-dimensional analyses were performed using X-ray micro-computer tomography (μ CT) to quantify the evolution of the microstructure during sintering. This revealed pore defect structures that were attributed to both powder spreading and jetting of the binder. Subsolidus sintering was able to remove those defects attributed to jetting but not all the defects attributed to powder spreading. In contrast, supersolidus sintering in the first step of the VRA process was able to remove all the defects. However, the second step of the VRA process was not able to fully prevent the formation of grain boundary phases on cooling. To further support the attribution of the pore structures to powder spreading and binder-jetting, “skin” structures were printed. These samples contained a “core” in which the powder was spread but not

jetted surrounded by a “skin” that was both spread and jetted. μ CT analysis revealed differences in densification behavior between the “skin” and the “core” that resulted in differential sintering. The microstructure heterogeneity caused by differential sintering could also be repaired by supersolidus sintering.

Table of Contents

Preface.....	xvi
1.0 Introduction.....	1
2.0 Background	5
2.1 Binder-jet 3D Printing (BJ3DP) in Powder Metallurgy	5
2.1.1 Introduction to Binder-jet 3D Printing.....	5
2.1.2 Particle Packing and Printing Defects in BJ3DP	9
2.1.3 Impact of Defects on Material Properties.....	14
2.2 Consolidation of Densifying Porous Systems.....	17
2.2.1 Sintering.....	17
2.2.2 Microstructure Evolution in Heterogeneous Porous Structures	20
2.2.3 Supersolidus Liquid Phase Sintering (SLPS) and Differential Sintering	24
2.3 Microstructure Characterizations and Analysis Strategies	29
2.3.1 Quantitative Stereology	29
2.3.2 Field Measurements vs. Feature Measurements	31
2.3.3 Statistical Approaches	33
2.4 Three-dimensional Characterization via Micro-computer Tomography (μ CT) ...	35
2.4.1 Advantages of Three-dimensional Characterizations	35
2.4.2 Introduction to Computer Tomography (CT).....	38
2.4.3 Applications of Micro-computer Tomography in PM and Sintering.....	40
2.5 Rationale for This Work	41
3.0 Hypothesis.....	48

4.0 Objectives.....	49
5.0 Experimental Methods	51
5.1 Synthesis of Samples.....	51
5.1.1 Binder-jet Printing of Regular 625 Alloy Green Samples.....	51
5.1.2 Sintering of Printed Green Bodies.....	52
5.1.3 Printing and sintering of “Skin” and “Crucible” samples	54
5.2 Microstructure Characterizations	55
5.2.1 Two-dimensional Characterization	55
5.2.2 Three-dimensional Characterization	56
5.3 Other Characterizations	56
5.3.1 Density Measurements.....	56
5.3.2 Chemical Segregation via SEM-EDS	57
5.4 Statistical Analyses	58
5.4.1 Feature Measurements	58
5.4.2 2D and 3D Microstructural Pathways	59
5.4.3 Data Analysis and Visualization	59
6.0 Results and Discussions	61
6.1 Regular Binder-jettted Structures	61
6.1.1 Density and Porosity	61
6.1.2 2D Characterizations and Stereology.....	63
6.1.3 CT Results.....	68
6.1.4 Statistical and Orientation Analysis	77
6.1.5 Comparison between 2D and 3D Results	87

6.1.6 Three-dimensional Microstructure Pathway	89
6.2 “Skin” Samples	94
6.2.1 Experimental Design and Methods	94
6.2.2 Density	96
6.2.3 CT Results.....	97
6.2.4 Discussion.....	109
6.3 “Crucible” Samples	110
6.3.1 Experimental Design and Methods	110
6.3.2 Results	111
6.3.3 Discussion.....	116
7.0 Conclusions.....	118
8.0 Future Work.....	121
Appendix A Stereological Parameters, Topological Measurements and Microstructural Pathways.....	122
Bibliography	126

List of Tables

Table 1 Time durations for SS, SLPS and VRA group samples during isothermal sintering	
.....	54

List of Figures

Figure 1	The “playing field” of P/M where it shows advantages. Figure adopted from [4] ..	6
Figure 2	Schematic illustration of BJ3DP.	7
Figure 3.	Packing efficiency of binary particles with different sizes. Figure adopted from [25]	
	11
Figure 4.	Random packing efficiency of a single log-normal distributed particles.	12
Figure 5.	Demonstration of printing lines on sample surfaces made by BJ3DP. (a) Photo of an as-printed silicon carbide cube; (b) Surface profile of the printed SiC using optical microscopy.....	14
Figure 6.	A 2D slice of CT-scanned as-printed 625 alloy sample. The linear defects along the printing direction (printing lines) can be readily seen.	14
Figure 7.	A simple two-sphere model of sintering (initial stage).	18
Figure 8.	Left: A sketch of particle shape changes in different stages of sintering. (a) Before sintering; (b) At the end of initial stage; (c) Intermediate stage and (d) final stage. Right: DeHoff’s space-filling polyhedra[45].....	19
Figure 9.	A one-dimensional model of the combined-stage sintering model. [49]	21
Figure 10.	A sketch of remnant large pores in final stage sintering. The effective diffusion distance, in this case, is two times the grain size[55].....	24
Figure 11.	The capillary force acting between two spheres connected by a liquid bridge as a function of interparticle distance. Value C corresponds to the ratio of adjacent particle sizes. [57]	26
Figure 12.	Schematic illustrations of structures undergo differential sintering.[60]	27

Figure 13. Reconstructed pore network in a sintered α -alumina granules. Image adopted from [61] 28

Figure 14. A sketch of pore boundary tessellation..... 33

Figure 15. The CA-SAF plot for sintered alumina[74], showing the two systems took different pathways during sintering..... 34

Figure 16. Sectioning a sphere with a plane that does not pass through the geometric center. 36

Figure 17. A basic setup of μCT . Image adopted from [93] 38

Figure 18. A CT-scanned silicon carbide pellet. (a) side projection; (b) a reconstructed slice. 40

Figure 19. Visualization of soda-lime glass grains under sintering colored mesh shows grain growth and coalescence at different sintering times (red – 20 min, blue – 90 min, yellow – 120 min)..... 41

Figure 20. Optical Micrographs for binder-jetted 625 alloy sintered at (a) 1270 °C and (b) 1285 °C, both for 12 h. 42

Figure 21. Archimedes densities for 625 samples sintered 0 – 12 h. (a) 1270 °C; (b) 1285 °C. In this study, refer to powder W for 16-63 μm PSD. [112]..... 43

Figure 22. Pore area frequency distribution for (a) (b) subsolidus and (c) (d) supersolidus sintered 625 alloy. (a) (c) show relative frequency distributions whereas (c) (d) show absolute pore number count in the microstructure. Figure edited from [112] 44

Figure 23. A schematic illustrating densification and particle rearrangement mechanisms for (a) SS and (b) SLPS. Adopted from [112]..... 46

Figure 24. SEM-EDS elemental maps for (a) (b) subsolidus and (c) (d) supersolidus sintered 625 alloy. Figure adopted from [112].	47
Figure 25. PSD measured for gas- and water-atomized 625 alloy powder. Figure adopted from [114]	52
Figure 26. Workflow for 3D image processing and analyses.	59
Figure 27. Density and Open porosity measured by Archimedes method. (a) SS, (b) SLPS, and (c) VRA sintering	61
Figure 28. OM images (100X) for SS (left) and SLPS (right) sintered samples. The images are taken on the XOZ-plane therefore interlayer defects (vertical) and printing lines (horizontal) may be visible.	64
Figure 29. SEM images of VRA samples under different SS-time.	66
Figure 30. Liquid Area Fraction (LAF) of SLPS and VRA – sintered samples. The LAF data was calculated from SEM images using ImageJ[118].	66
Figure 31 A Ni-Nb isopleth showing phase formations of the 625 alloy. Dashed line shows a Nb composition of 3.7 wt.%. Image adopted from [116].	68
Figure 32. Reconstructed μCT images for SS (left) and SLPS (right) samples, anatomical view. SLPS 0.75 h and 1 h samples were excluded due to their high density and difficulty in X-ray penetration.	70
Figure 33. SAF variation along Z-direction for SS and SLPS samples.	71
Figure 34. Sphere fitting of an enclosed object. Dashed lines indicate skeletonized axes. Image adopted from [120].	73
Figure 35 An illustration of applying structure thickness/separation analysis on a porous structure. Figure edited based on [55]	75

Figure 36. Structure thickness and separation distributions..... 76

Figure 37. Mean and standard deviation of pore areas observed by OM. 77

Figure 38. Distribution frequency plot for pore volumes measured in 3D, unit in μm^3 . Top figures show the distributions counted by absolute number; bottom figures show relative frequencies. 78

Figure 39. An example of applying intercept measurements on a reconstructed CT slice. The image has been segmented such that white objects reflect pores. 80

Figure 40 The line intercept analysis using a stack of images in the SS 0 h sample. A “half-wavelength” of the images were chosen in the analysis..... 82

Figure 41. Line intercept test results. Blue markers represent horizontal intercepts, orange markers vertical intercepts, and grey the average. X axis shows the relative z-height in the “mini-stack” (minima-maxima from left to right, with respective 2D SAF values)..... 84

Figure 42. Comparison among Archimedes density, optical micrograph SAF and CT results. Left: SLPS samples; Right: SS Samples. 87

Figure 43. Average pore volume as a function of density. (a) all samples; (b) SLPS; (c) SS. 89

Figure 44. Pore surface to volume ratio as a function of density. (a) all samples; (b) SLPS; (c) SS..... 91

Figure 45. Structure thickness and separation evolution as a function of density. The coordinates of the balloons correspond to the mean of STTH/STSP, and the radii represents standard deviation..... 92

Figure 46. Standard deviation of SAF variation as a function of density..... 93

Figure 47. A cross-sectional view of CAD model for skin samples. Note that the hollow “core” shown in the CAD model will be filled with spread powders during actual printing. 95

Figure 48. Archimedes density for skin samples sintered under SS and SLPS temperatures. For SLPS sintering, the time durations are 0, 0.25, 0.5 and 1 h. 96

Figure 49. Reconstructed μ CT images for SS (left) and SLPS (right) skin samples, anatomical views. SLPS 1 h sample were excluded due to their high density and difficulty in X-ray penetration. SLPS 0.25 h and 0.5 h samples are cut into smaller sizes with WEDM to ensure X-ray attenuation. 98

Figure 50. SAF variation along Z-direction for skin samples, sintered under SS and SLPS temperatures. (a) overall ROI, (b) SAF for core, (c) SAF for shell. For VRA sample, the core and shell are no longer distinguishable due to high final density, therefore data were not included in (b) and (c). 100

Figure 51. 3D Solid volume fraction of skin samples calculated from segmented CT images. (a) SLPS sintered, (b) SS sintered. 102

Figure 52. Average closed pore volume. (a) SLPS sintered, (b) SS sintered. 103

Figure 53. Closed pore surface to volume ratio. (a) SLPS sintered, (b) SS sintered. 105

Figure 54. Closed pore number density (per unit volume). (a) SLPS sintered, (b) SS sintered. 106

Figure 55. 3D structure thickness and separations. (a) (b) SLPS sintered, (c) (d) SS sintered. Error bars show the standard deviation of structure thickness and separation..... 107

Figure 56. CAD model of a crucible sample. The inner diameter, outer diameter, and height is 2 mm, 4 mm, and 10 mm respectively. 110

Figure 57. Sintered density for crucible samples. 111

Figure 58. Comparison of densities for crucible, skin and regular samples. (a) SLPS sintering from 0 h to 1 h; (b) SS sintering from 0 h to 8 h. 112

Figure 59. Reconstructed μ CT images for SS (left) and SLPS (right) crucible samples.... 113

Figure 60. SAF variation along Z-direction for crucible samples, sintered under SS and SLPS temperatures..... 114

Figure 61. A proposed schematic (XOZ-view) of the differential sintering and rearrangement during SLPS sintering of the crucible samples. The size of the red arrows shows the relative magnitude of sintering stresses. 117

Preface

I would like to thank my family for their unreserved love and support for me during my pursuit of the doctorate degree. I would also like to thank my friends from my high school and college who accompanied me all the time throughout my graduate career until the very end. I would like to express my appreciation in particular to my girlfriend, Qi Chen, MSW, and wish her all the best in the studies towards her PhD.

I would like to express my gratitude and respect towards my dissertation committee members, Drs. Jung-Kun Lee, Markus Chmielus and Anthony Rollett. A special thanks to Dr. Chmielus for all the equipment, lab supplies and bright ideas that he had to offer generously. I would also like to thank the colleagues in all the facilities and labs that helped my research, including NFCF, MMCL and many others. All your efforts have made Benedum Hall a little vivid neighborhood that I enjoyed living in. I appreciate the help from the undergraduate students, Yixiao He and Mingcheng Han, who helped on this research project. Also, there are many other students who worked in the ceramics processing lab on different projects – thank you as well.

The majority of this research is sponsored by the Pennsylvania Manufacturing Fellows Initiative (PMFI). I am sincerely grateful of the support from the Manufacturing PA Innovation Program.

Manners maketh man. Lastly, I would like to say a special thanks to my Advisor, Dr. Ian Nettleship. The five years that I spent working with you was the most joyful time in my life. Not only did I learn from you the knowledge and skills necessary for my research, but also the gentleness, the personal charm, and the noble willingness to serve for the welfare for the entire human being. You have set up a role model in my heart that I would refer to become a better man.

1.0 Introduction

Additive manufacturing (AM), as a novel technology, has gained increasing attention in powder metallurgy (P/M). Compared to beam-based AM technologies, binder-jet 3D printing (BJ3DP) provides better shape precision and can produce residual stress-free parts. However, as printed parts made from binder-jet printing tend to be more defective. In BJ3DP, the part is printed in a layer-by-layer manner, creating packing defects at the layer boundaries. In addition, the jetting of the resin into the powder bed can displace powder particles creating even more powder packing defects. Hence the green density of binder-jet printed metals is lower than the green densities achieved by traditional compacted P/M parts. The relatively large packing defects introduced during printing are likely to remain in the final microstructure as remnant porosity, which is highly detrimental to mechanical properties of the finished parts, especially fatigue strength. Traditionally the remnant pore removal can be done in post-sintering operations such as hot isostatic pressing (HIP-ping). Unfortunately, HIP-ping is expensive, likely to lead to part distortion and is not capable of removing pores and cracks connected to the surface without encapsulation. This will negate the shaping advantages of BJ3DP processing.

In a previous study, nickel-based superalloy Inconel 625 (abbreviated as “625 alloy” or “625”) was printed using BJ3DP with different particle size distributions (PSDs), and subsequently sintered at subsolidus and supersolidus temperatures. It was found that the powders with wide PSD resulted in improved powder packing during printing and higher green densities. Supersolidus sintering of such sample promoted extensive densification and finally reached full density (>99%). However, due to the presence of liquid phase, it can be expected that the alloying elements were partially segregated to particle boundaries which can degrade high temperature mechanical

properties such as creep resistance. Subsolidus sintering was unable to reach final stage densification even after 12 hours of sintering. Additionally, supersolidus sintering of samples printed with narrow PSDs reached lower final densities (~97%). In the preliminary work of this proposal, quantitative feature analyses were performed on polished sections of sintered samples. Pore size distributions showed that in wide PSD – supersolidus sintered samples, large pores were preferentially removed within the first hour of sintering. This is indicative of desirable particle rearrangement (viscous deformation) under the surface tension of a wetting liquid. After 2 hours of sintering, pores were small with respect to the grain size and were thought to densify via contact flattening in conventional liquid phase sintering. Separate preliminary studies using micro-computer tomography (μ CT) scans of consolidated SiC and Ni-Mn-Ga alloy have demonstrated that 3D imaging could be applied to the study of sintering of binder-jet printed powders including sintered Ni alloys. 3D analysis, including pore volume, orientation distribution and topological parameter calculations, circumvents the ambiguity of 2D characterizations and reflects the microstructural evolution in a more objective way.

Based on preliminary results, a viscous liquid rearrangement assisted (VRA) sintering process is proposed in this work. This process will consist of two steps: first, as-printed alloy samples are sintered above the solidus temperature for a short period of time. This will facilitate particle rearrangement, and in this step large pores due to packing defects should collapse. The second step is solid-state sintering by lowering the temperature under the solidus temperature. In this step, remaining finer pores were expected to be fully eliminated via the dominant densification mechanism in the solid state. At the same time, segregated alloying elements would be allowed to homogenize through diffusion back into the grains. This hypothesis was tested. Additionally, two novel types of green structures were designed to separate the effect of powder spreading and

binder-jetting, namely the regular, the “skin” and the “crucible” samples. The objectives of this work were: 1) to demonstrate that VRA sintering is able to densify printed 625 alloy and also allow chemical homogenization; 2) to demonstrate the utility of 3D characterizations in study of both green (packing defects) through to final state (closed pore population) of samples; 3) to develop a quantitative method of representing microstructure evolution of porous materials during sintering via statistical approaches; and 4) To observe the evolution of the population of packing defects created by binder-jet printing during sintering and to determine how these defects correlate with the spreading and jetting processes.

Throughout the sintering processes, a set of interrupted characterizations were conducted. These characterizations include density measurements on green and sintered bodies, optical microscopy on polished sections, 3D characterization using μ CT, and SEM/EDS mapping at the grain and pore boundaries. The measurements extracted included density and porosity, 2D/3D pore size distribution, pore shape and orientation descriptors, structure thickness and separations, and spatial chemical composition. These data were to be analyzed and visualized using statistical approaches and microstructure maps. More importantly, it was proposed that for the first time a combination of quantitative 2D and 3D characterization methods could be used to describe the microstructural evolution of binder-jet printed metal powders from green state of the sample to the final microstructure. It was anticipated that coupling 2D and 3D characterizations of microstructure populations in sintering could be used to give a description of microstructure evolution in subsolidus and supersolidus sintering and clearly distinguish their differences, explaining why supersolidus sintering is more capable in sample densification. Using similar approaches, the microstructure evolution of the skin and crucible samples are also quantitatively investigated to reveal the capability of repairing different types of printing defects with the

presence of viscous liquid. It is possible that between interlayer defects and printing lines, one defect type may be more difficult to remove during sintering than the other, and hence more detrimental to the final microstructure and resulting mechanical properties.

It ought to be point out that the expected outcome of this work does not only apply to the Inconel 625 alloy system, but is anticipated to provide guidance on sintering a variety of prealloyed powder systems being used in BJ3DP. The densification mechanism and the observed microstructural descriptors, along with the analysis methodology, should also apply to other densifying metal systems that may form a secondary liquid phase when sintered above their solidus temperatures. The microstructural pathway and 3D microstructural parameters should also be generally applicable to these systems as a means of microstructure control. Moreover, the comparison of 2D microscopy and μ CT results should demonstrate the feasibility of 3D microstructure characterization in P/M applications.

2.0 Background

2.1 Binder-jet 3D Printing (BJ3DP) in Powder Metallurgy

2.1.1 Introduction to Binder-jet 3D Printing

Powder Metallurgy (P/M), as a subset of metalworking technologies, in essence “takes a metal powder with specific attributes of size, shape, and packing, then converts it into a strong, precise, high performance shape”[1]. Basic steps of P/M include powder production, green part formation and consolidation. Compared with other metalworking technologies, parts made by P/M have several unique advantages. For mass production of low-cost engineering metals, P/M can be more cost effective at making small, shaped components than other technologies such as casting and machining due to the rate of material utilization and recyclability of the powder feedstocks. For P/M processed parts, little machining or other treatment is required to obtain good surface finish or control of the part shape and dimensions within reasonable ranges of tolerance. Some metals or alloys that are difficult to process, such as refractory metals, can only be processed via powder metallurgy. Using prealloyed powders, P/M processes can be carried out below the melting temperature, by eliminating the sources of macrosegregation or defects formed during solidification, as one would usually encounter during casting.[2] Such advantages can make P/M the first choice, if not the only one, in fabricating refractory metals and some superalloy components. Recently, in the nickel-based superalloy industry, the shift in material’s performance requirements has promoted the application of P/M to an even larger extent. For instance, modern design of turbine engine disks has an increasing focus on the control of material failure rather than

merely increased strength. Such a shift in focus has driven the processing of superalloys from ingot casting towards P/M, as the latter provides a more uniform microstructure with less chemical segregation and results in better fatigue behavior.[3] A figure showing the “playing field” of P/M is illustrated in Figure 1.

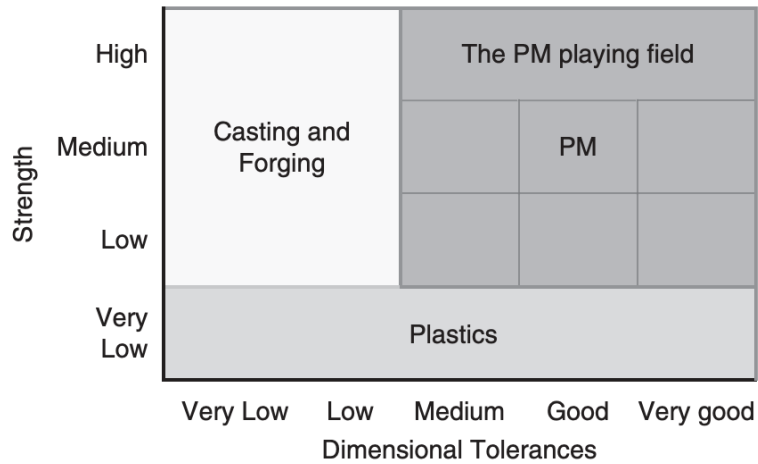


Figure 1 The “playing field” of P/M where it shows advantages. Figure adopted from [4]

While being able to avoid many issues associated with other metalworking technologies, P/M has its own inherent shortcomings. Typical limitations of P/M include high initial investment, including design and manufacturing of molds and die sets, as well as the need for hot isostatic pressing facilities for full consolidation. The complexity and degrees of freedom in shape design is also significantly constrained. Some of these issues can be addressed by additive manufacturing.

Additive manufacturing (AM, or 3D-printing) refers to “process of joining materials to make parts from 3D model data, usually layer upon layer, as opposed to subtractive manufacturing such as machining and formative manufacturing methodologies.”[5] Since the invention in 1993 by Sachs et al[6], additive manufacturing has been developing rapidly as a manufacturing method competing with traditional machining, casting, molding, and other techniques for making complex shapes. Binder-jet 3D printing (BJ3DP) is one of the mainstream AM technologies which can be applied to metals and also to some ceramics[7–9].

The printer configuration is shown in Figure 2. The binder, which is usually made of aqueous or solvent-based polymer solutions, is injected into a loose powder bed from a printhead. Many individual jet nozzles are aligned in parallel inside the printhead and hence are able to inject the binder simultaneously. After the printhead scanned through the building area, the bed is moved towards a heat source to partially cure the binder, which bonds the powder particles into the shape of the CAD model. Then, the piston underneath the powder bed moves downward by the thickness of one layer. A new layer of powder is fed into the top of the powder, and a roller/recoater is used to flatten the bed. Then another cycle of powder deposition process is executed, and the part is eventually built up layer-by-layer in this way. Finally, the part is removed from the powder bed via a depowdering process and ready for post-processing treatments.

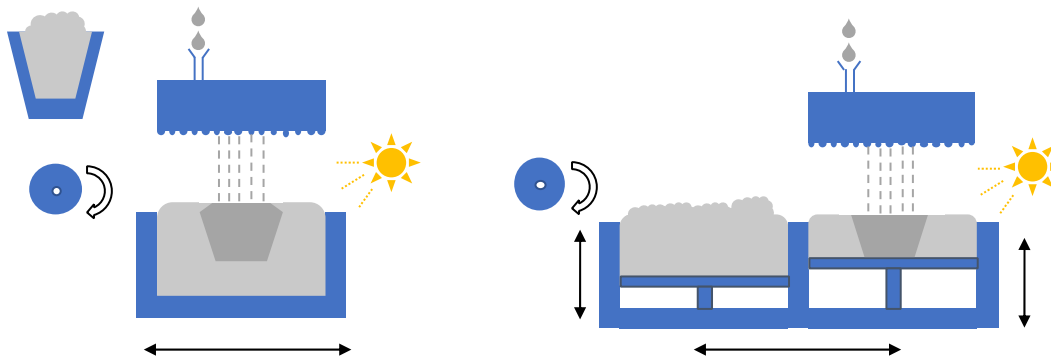


Figure 2 Schematic illustration of BJ3DP.

There are many other AM technologies aside from BJ3DP that are applicable to metals. Two of the most widely used technologies are Selective Laser Melting (SLM) and Directed Energy Deposition (DED). The two typical systems representing these technologies are EOS (EOS GmbH, Germany) and LENS (Optomec, USA). SLM uses a setup that is somewhat similar to BJ3DP, where it houses a powder bed and a recoater, but the binding of loose powders is carried out by a high-energy laser scan that melts the deposited metal powder. The laser first scans through the contour of the cross-section in a single slice, and then scans back-and-forth to cover the entire

cross-sectional area. Then the powder bed substrate moves downward and the recoater deposits a new layer of loose powders on top of the printed layer. Such printing cycles are executed until the part is built. The part is removed, first via a depowdering process, followed by the removal process from the substrate, commonly using a wire-EDM machine. No post-processing is necessary given the fact that the laser beam provides substantial power to weld the powder particles, although a variety of defects may exist and detract from the mechanical properties. The DED process uses a nozzle that connects to one or multiple powder feeders to deposit the powder at the exact spot where the energy (laser or electron beam) is applied. In other words, the powder deposition moves along with the laser/E-beam. In this case no post-processing is required except the part removal from the substrate.

Comparing with these AM technologies, BJ3DP has its own advantages and drawbacks. Among the three metal AM technologies discussed above, BJ3DP is the only method that binds the loose powder without intense energy input, which means that the residual stress in the as-printed parts is diminished. On the contrary, for SLM method, the mismatch in thermal expansion coefficients between the substrate and printed parts and the differential cooling through the parts are the main causes of severe residual stress and distortions. To tackle the problem, significant amount of time and effort must be devoted to Design of Additive Manufacturing (DFAM) [10–12], and in many cases compromises in the designed shape are inevitable. Similar issues also occur in the DED process, and even more work needs to be done to fully investigate these problems[13]:[14]. On the other hand, such distortion is much less pronounced in BJ3DP-fabricated materials[15]. Another advantage for BJ3DP over other laser-based methods, is that the printing speed of BJ3DP is significantly higher than laser-based methods, given the fact that many binder nozzles are arranged in parallel (e.g., in the X-1 Lab there are 128 nozzles) that injects

binder simultaneously. In this way the loose powder is not fixed line-by-line but in a layer-by-layer manner. As a consequence, the printing efficiency of the BJ3DP machines, or the build speed in seconds per layer, can be tens of times faster than that of the SLM machines.

There has been substantial number of attempts applying BJ3DP on a variety of material systems, such as stainless steel[16], TiC/steel composite[17], Fe-Mn-Ca/Mg alloys[18], Ni-Mn-Ga shape memory alloy[19], Inconel 718[20] and 625[21], to name a few. On the other hand, there are limitations for the material systems that can be used in BJ3DP. For example, it is difficult to produce monolithic ceramic parts using BJ3DP. To ensure flowability of the powder spread, the powder feedstock used in BJ3DP is much larger than the particles used in normal ceramic processing. As a consequence, these powders have very low surface energy which is extremely detrimental for sintering for ceramics. An alternative method for green body consolidation is by infiltration, but for many systems the effect of infiltration is far from ideal[22] [23]. Other issues include some pure reactive metal powders that oxidize easily even at binder curing temperatures, such as copper.

2.1.2 Particle Packing and Printing Defects in BJ3DP

The potential for mesoscale defects, or porosity, has always accompanied powder metallurgy processes. The green part density after shape forming typically depends on the attributes of the powder feedstocks, including particle size distribution (PSD), particle shape and density, binder content, etc.[24]. Since the packing efficiency of powder particles is low under gravity, in traditional powder metallurgy processes such as powder pressing, pressure is applied to increase the green density of parts. As pressure increases, packed metal powders undergo a series of processes: first, the particles rearrange to eliminate large packing defects, and increase in

particle coordination. Then the particles will bear the pressure and begin to deform elastically. Once the yield strength is reached, particles will undergo plastic deformation at the particle contacts such that the shape of a particle will accommodate its neighbor and fill up the interstitial spaces. For brittle materials or strain hardened ductile materials fragmentation may occur. A higher green density will allow the subsequent sintering process to initiate at a higher bulk density so that the time and energy required for sintering is drastically reduced.

In P/M, the traditional methodology of modeling the packing of particles in the green body is based on the random packing model of hard spheres. McGeary[25] demonstrated that the maximum reachable density by random packing of one-size spheres is 62.5% theoretical density of the material. However, the interstices between random packed particles can be filled up with particles of smaller sizes. McGeary showed that a maximum of 86% theoretical density can be reached via mixing a binary distribution of particles as shown in Figure 3. He also pointed out that for smaller particles to successfully fill in the interstices between large particles, the size ratio of large particles to small particles must be at least 7:1. This ratio usually serves as a rule of thumb in powder feedstock design in P/M. However, it is impractical to prepare a truly bimodal powder system, as the as-received powder, regardless of the means of synthesis, will have a continuous distribution.

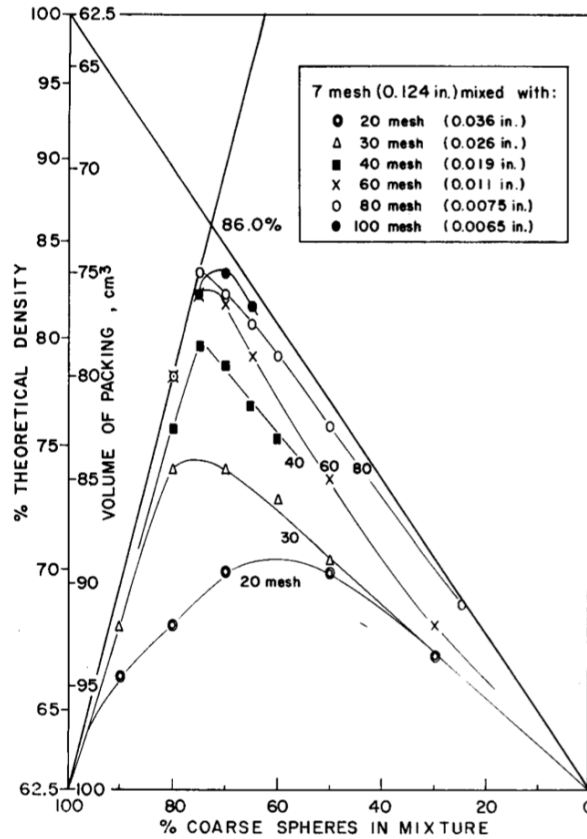


Figure 3. Packing efficiency of binary particles with different sizes. Figure adopted from [25]

Comparing with bimodal distributions, only a few studies have been performed on packing behavior of particles with continuous distributions. Bierwagen et al.[26] implemented an idealized lognormal PSD function and applied to the packing efficiency equation derived by Lee[27]. They concluded that for a single continuous lognormal distribution, the standard deviation of PSD strongly affects the packing efficiency, as shown in Figure 4[26].

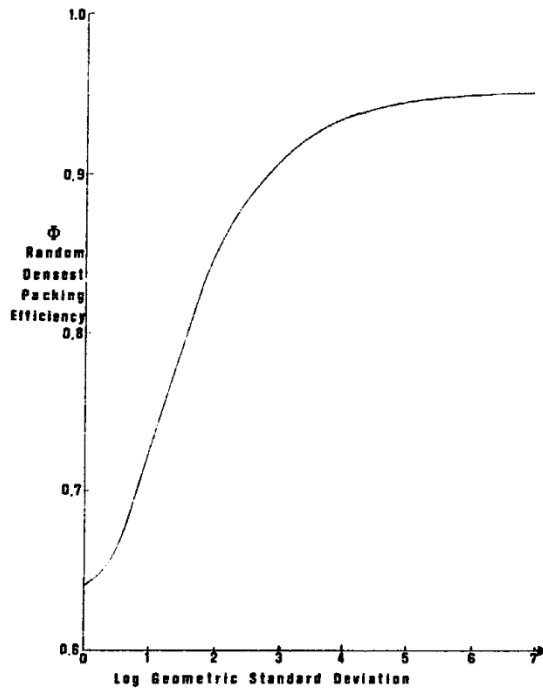


Figure 4. Random packing efficiency of a single log-normal distributed particles.

Note that the packing efficiency increases with increasing the standard deviation of PSD and may eventually reach approximately 0.96 if the powder sizes are distributed widely enough. Therefore, the powder feedstock design methodology should use a continuous distribution that has a large standard deviation.

Such process design methodologies have become widely practiced in P/M technologies, such as powder compaction and metal injection molding. The premise behind such methodology is that larger particle packing defects due to particle packing are comparatively rare and randomly distributed through powder metallurgy parts. However, in BJ3DP the defects do not appear to be randomly distributed. The defects in an as-printed green part made by BJ3DP can be divided into two major types: voids between adjacent printed layers, and printing lines caused by the interaction between liquid binder and powder bed that results in ballistic ejection[28]. Inter-particle interstices, which occur in all powder bodies, are the voids between particles and will occur within the printed layer. Due to lack of pressure, the layer-by-layer manner of building and the inability

of particles to pack well adjacent to a surface, the inter-layer region should have a higher defect concentration. These larger defects are non-isotropic and concentrated in the build plane (x-y plane) and will remain open to the exterior surface until substantially consolidation has been achieved in sintering. Moreover, these are the defects that are most likely to remain in the final microstructure after sintering and effect the mechanical properties of the final product. The generation of interlayer defects is affected by many printing parameters, such as binder saturation, drying time and power, type of additives[29], and most importantly PSD[30]. Mostafaei et al.[21] investigated the printing and densification behavior of binder-jet printed 625 alloy and found that a wide PSD can amend the interlayer defects via rearrangement of small particles near the layer boundaries.

Printing lines are created during the binder injection process after the powder layer has been spread. The binder in the printhead is injected with kinetic energy and will impact the loose powder bed. Without specific treatment, the cohesive energy that bonds the thin top layer of powder bed is quite weak. Therefore the kinetic energy carried by the binder will “flush out” some powder particles causing local rearrangement along the trace of injection, ending up with visible printing line defects. Similar to interlayer defects, the degree of ballistic ejection is a function of many printing parameters, such as binder saturation, printing speed, moisture content which controls the cohesive strength of powder bed, and PSD[28][31]. These printing lines can be seen visually on the surface of as-printed parts and can be qualitatively measured using the profiling function on an optical microscope, as shown in Figure 5. μ CT scan also shows that the printing lines are stacked along the z-direction, making these defects widespread and hence difficult to remove during sintering. A cross-sectional μ CT image of as-printed 625 cylindrical part is shown in Figure 6, indicating printing lines[32].

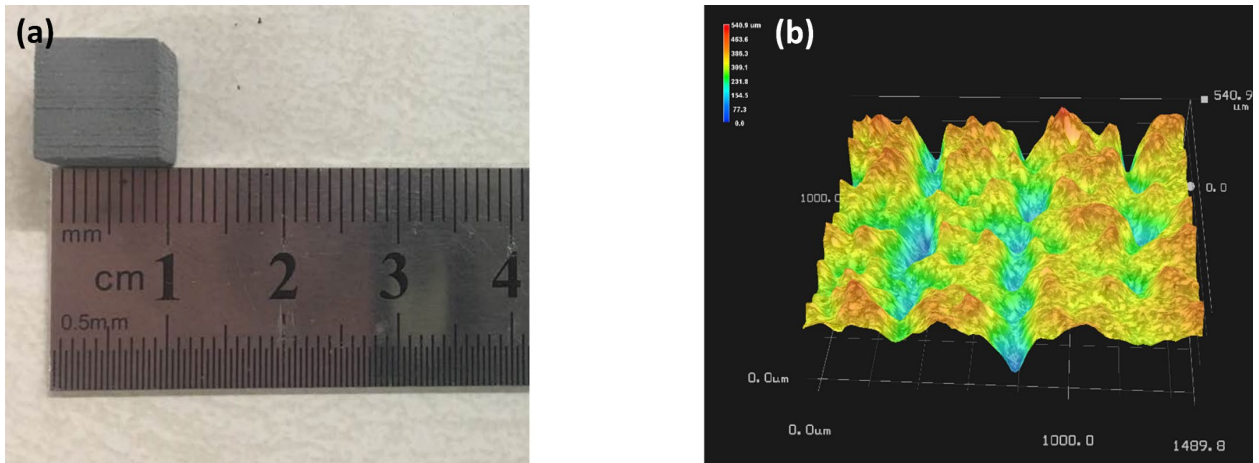


Figure 5. Demonstration of printing lines on sample surfaces made by BJ3DP. (a) Photo of an as-printed silicon carbide cube; (b) Surface profile of the printed SiC using optical microscopy.

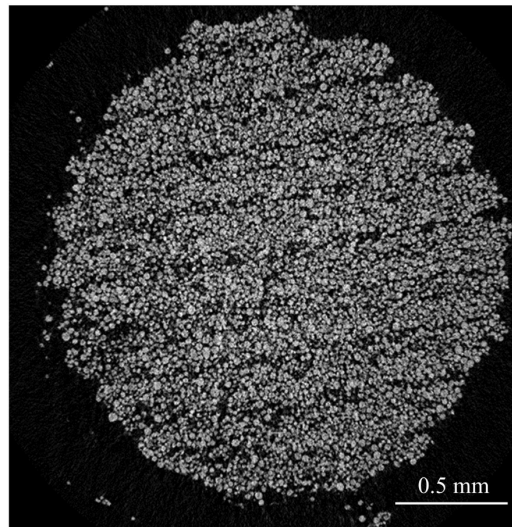


Figure 6. A 2D slice of CT-scanned as-printed 625 alloy sample. The linear defects along the printing direction (printing lines) can be readily seen.

2.1.3 Impact of Defects on Material Properties

Properties of materials made by powder metallurgy are usually related to the thermomechanical process applied to the feedstock material. For mechanical properties especially fatigue behavior, the performance of the final product greatly depends on its remnant defects, such

as inclusions or porosity. It has been shown that in BJ3DP the pores are larger and more difficult to remove for as-printed parts than parts produced via traditional P/M technologies. Hence the issue of remnant porosity in binder-jet printed materials, its origin and its effect on mechanical properties must be addressed.

It has been decades since the first research on the relationship between pore size and strength was conducted. Bal'shin[33] modeled, for the first time, that the strength of a ductile material that has uniform sized, homogenously distributed pores, can be calculated by the equation below:

$$\sigma = \sigma_0(1 - \theta)^m \quad (2-1)$$

where σ_0 is the ultimate strength of a fully dense material, θ being porosity, and m is a constant. Based on this model, Shcherban[34] made an assumption that the loss of strength is contributed to by two types of loss: “matrix” and “skeletal”. Matrix loss refers to the loss in strength of interparticle contacts, and “skeletal” loss is due to the change of the numbers of “bridges” connecting particles in a porous material. Hence the modified expression of porous material strength becomes:

$$\sigma = \sigma_0(1 - \theta^2)^2 \exp(-B\theta) \quad (2-2)$$

Here, B is a composite constant such that $B \approx m$ at low porosity. It has been reported that the modified model agrees well with experimental data, but this equation did not consider the other attributes of pores and their distribution throughout the tested specimen. Brown et al.[35] studied the effect of pore shape and orientation distribution on the strength of porous materials. They concluded that the strength of a material with given pore shape and orientation can be calculated as

$$\sigma = \sigma_0 \cdot \{1 - \sum_i [(x_i a_i / v_i) p_i]\} \quad (2-3)$$

Where a_i is the projected maximum cross-sectional area, x_i is the characteristic length, v_i is the volume of pores and p_i is porosity contributed by the i th type of pores. This equation implies that one is able to characterize non-isotropic pores with a variety of attributes and distributions. The drawbacks of this model are that 1) it only considers crack propagation rather than initiation and should not be expected to be valid at low porosities, and 2) the pore size distribution does not play an important role in this expression. Interestingly, a recent study on binder-jet printed copper systems[36] showed that the strength of these parts was systematically lower than the model prediction, while a HIP-ped part made with bimodal PSD exhibits the highest density as well as desirable mechanical properties.

There are a few experimental studies on the pore size distribution-strength relationship for a variety of material systems. Torii et al.[37] investigated the relationship between strength and pore size distribution in compacted soils. Hou et al.[38] used statistical approaches to model the compressive strength as a function of porosity and pore size distribution. Zakeri et al.[39] studied crushing strength reliability of industrial-scale alumina catalysts controlled by porosity and pore size distributions. They concluded that for powders with higher surface area/volume ratio, although the crushing strength was decreased, the reliability of such strength was increased due to the reduced width of pore size distribution.

Porosity will also degrade ductility. For sintered P/M materials the relative ductility Z can be calculated as a function of porosity:

$$\mathbf{Z} = \frac{(1-\varepsilon)^{3/2}}{(1+c\varepsilon^2)^{1/2}} \quad (2-4)$$

Where c is an empirical constant and ε is porosity. Again this equation does not take into account individual pore attributes; in fact ductility is sensitive to pore shape and spatial

arrangement. It is qualitatively found that cast and wrought alloys have better ductility than P/M alloys with the same amount of porosity[1].

Although remnant pore population greatly affects the fatigue behavior of P/M materials, a quantitative relationship that links these two is still absent. A few qualitative studies have been performed on biomedical-compatible alloys such as Ti₆Al₄V[40–42]. It was concluded that a relative density of >98% is required for P/M Ti alloys to achieve satisfactory mechanical properties.

2.2 Consolidation of Densifying Porous Systems

2.2.1 Sintering

There are a variety of thermomechanical processes used to remove porosity in as-formed materials in P/M. For a densifying system, sintering or hot isostatic pressing (HIP-ping) is commonly used. For a non-densifying system, the porous material is usually infiltrated by a low-melting point material or precursor, and then heated to desired temperature to trigger necessary reaction (melting or pyrolysis). The goal of these processes is to increase the density of manufactured material and reach superior properties.

Sintering is defined as the process of firing and consolidating powder particles.[43] From thermodynamic perspective, materials during sintering eliminates the energy associates with the free surfaces in pores and replace with grain boundary energy. The driving force is the difference of atom mobility on two sides of a curved surface. Figure 7 Demonstrates the origin of shape change and mass transportation via a simple two-sphere model.

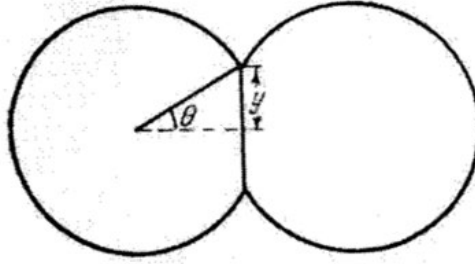


Figure 7. A simple two-sphere model of sintering (initial stage).

Note that the elimination of surface area occurs at the cost of neck formation between particles and hence introducing grain boundary energy. Therefore, for a particle-pore junction, the energies for free surface and grain boundary energy will follow Young's relation once the junction is in equilibrium. Let γ_s be the surface energy of the pore, γ_{gb} being the grain boundary energy, ϕ being the dihedral angle between two segment of pore surfaces separated by grain boundary, then at equilibrium

$$\gamma_{gb} = 2\gamma_s \cos\left(\frac{\phi}{2}\right) \quad (2-5)$$

Whether this equilibrium condition is achieved can be used to distinguish stages of sintering. Before the equilibrium being reached, there is a net mass flow from the bulk or surface of the powder particles towards the neck region, and the neck keeps growing. This is called the initial stage of sintering. Once the equilibrium dihedral angle being reached and the growing necks impinge to create grain edges, the stage of sintering is called intermediate. In this stage, the powder particles have changed shapes significantly from that of a two- or multi-sphere model. Coble[44] argued that in the intermediate stage of sintering, particles can be described as tetrakaidekahedrons, with cylindrical pore channels along the grain edges. Finally when the pore channels shrink to tetrahedral inclusions and become completely isolated from each other (pore closure), the rate of diffusion will decrease and the material reaches final stage of sintering. Figure 8[44] illustrates the shape change of particles and pores used for modeling the three different stages.

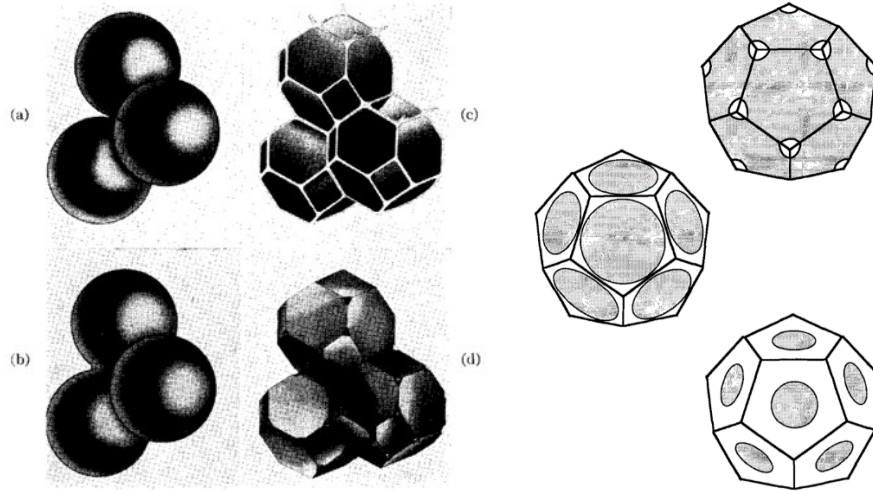


Figure 8. Left: A sketch of particle shape changes in different stages of sintering. (a) Before sintering; (b) At the end of initial stage; (c) Intermediate stage and (d) final stage. Right: DeHoff's space-filling polyhedra[45].

Castro et al.[46] studied the thermodynamic aspect of such sintering behavior and modeled the densification behavior by imagining a virtual “mechanical force” to promote pore elimination. It is derived that the equilibrium sintering model as follows:

$$\left(\frac{1}{\rho} - \frac{1}{\rho_0}\right) = \frac{6V}{P} \left(\sigma_P \frac{dA_P^{GG}}{dA_T} - \sigma_{GB} \frac{dA_{GB}}{dA_T}\right) \left(\frac{1}{D} - \frac{1}{D_0}\right) \quad (2-6)$$

Which includes a vapor pressure term P. This suggests that one may facilitate densification rate by increasing pressure, which forms the basis of pressure-assisted sintering. In P/M industries which require very high final density and uniform dimensional change, hot isostatic pressing (HIP) can be used. For example, it is reported that HIP-ped powder 316L stainless steel has slightly improved strength, toughness and corrosion properties comparing with other metalworking methods[47]. Froes et al.[41] also reported that a Ti-6Al-4V alloy can reach close to 100% density using a “cost-effect press-and-sinter” technique.

On the other hand, HIP-ping of metal parts formed by binder-jet printing is not as practical as in traditional P/M methods without necessary modification. Since the significant shrinkage and shape change resulting from the low green density will counteract the advantage in near-net shape

forming by BJ3DP, one must redesign the shape of part during the design for additive manufacturing (DFAM) stage. This usually requires “iterative information loops based on the computer analysis of dimensional data files”, and it may take months to modify and redesign the process[48]. Moreover, the open pore structure in as-printed green part makes the pores very difficult to collapse under pressure, let alone the high capital cost needed for the equipment setup. In a nutshell, HIP is not a practical solution for many P/M parts designed for specific applications. A cost-saving pressureless process should then be designed to remove all porosity while retaining the desired shape.

2.2.2 Microstructure Evolution in Heterogeneous Porous Structures

The two-sphere model and the tetrakaidekahedron based models used in the 3-stage sintering theory provide simplified geometries that allow for thermodynamic and kinetic analyses. The drawback of these models is the geometric discontinuities between the stages at arbitrary values of density, and the parameters involved in these models are scale dependent. Johnson et al.[49] developed a combined-stage sintering model which integrates three stages of sintering into one single geometry (see Figure 9). They assumed that the shrinkage of a pore entirely originates from the bulk and grain boundary adjacent to the pore, and by using Dehoff’s space-filling polyhedral (see Figure 8) geometry, sintering behavior at all stages can be expressed by a dimensionless factor Γ :

$$-\frac{dL}{Ldt} = \frac{\gamma\Omega_a}{k_B T} \left(\frac{\delta D_b \Gamma_b}{G^4} + \frac{D_V \Gamma_V}{G^3} \right) \quad (2-7)$$

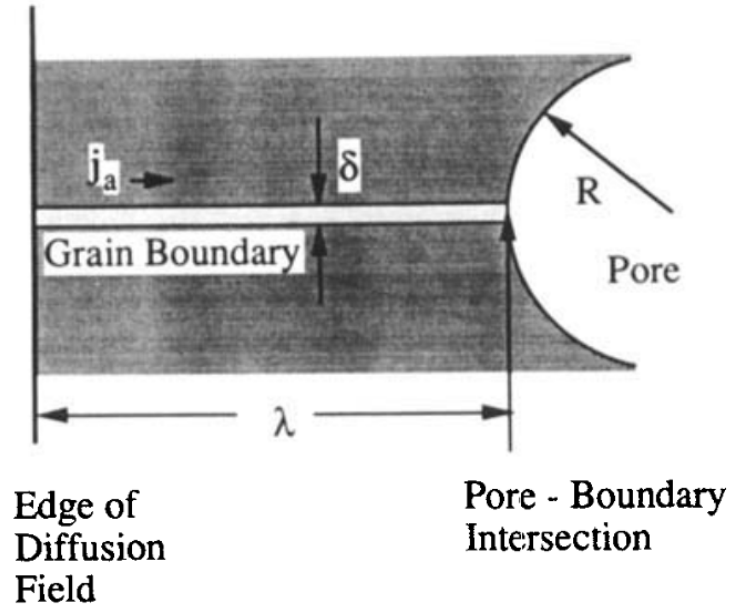


Figure 9. A one-dimensional model of the combined-stage sintering model. [49]

More geometries are available for complex modeling; however, these models, including the combined-stage model, naively assume that the vacancy sink is rigorously located adjacent to a pore throughout the microstructure, and therefore do not take into consideration the effect of local spatial heterogeneity created by particle packing defects or the potential scale change due to grain growth. In fact, due to the inevitable packing defects and the distribution of particle sizes in a green part, local microstructure can be quite different at different locations within the bulk sample. As discussed before, PSD can not only affect packing defects but also can determine the average grain coordination number surrounding a pore. Ting et al.[50] modeled the sintering and densification behavior by considering grain growth and initial PSD and concluded that the shrinkage during the initial and intermediate stage is a function of PSD, i.e.:

$$\mathbf{R} = \iint K_6 \frac{1}{G_0^{m1}} \left(\frac{1}{G_{0,g}} - \frac{1}{G_0} \right) f(G_0) h(t) dG_0 dt / \int f(G_0) dG_0 \quad (2-8)$$

$$\mathbf{R} = K_7 H(t) F_1(G_0) \quad (2-9)$$

Where $H(t)$ is a function of t relating the grain growth coefficient, K_7 is a constant and $F_1(G_0)$ is a function regarding the initial PSD. In a three-modal case, for the sake of illustration, one may obtain the shrinkage as a function of the grain size of the smallest particle and the ratio of particles:

$$\frac{\Delta L}{L_0} = \frac{K_8}{G_1^{4/3}} \left\{ \left[\left(\frac{1+R_{S2}}{R_{S2}^{2/3}} \right) + \left(\frac{1+R_{S3}}{R_{S3}^{2/3}} \right) \right] / (2 + R_{S2} + R_{S3}) \right\} t^{1/3} \quad (2-10)$$

Where G is the grain size of particles and R is the size ratio. Ting et al. pointed out that “the effects of finer and coarser particles are ‘competing’ with each other and depend on how far apart they are from the size of the center particle”. Taking into account the grain growth, along with the movement of grain boundaries (GB) the pores are dragged along by them. Once the mobility of pores become lower than that of the GB movement the pore will no longer stay at the GB but inside the grains. This will cause abnormal grain growth and eventually hinder sintering[51], since lattice diffusion is now required even if grain boundary diffusion is faster. The analysis showed that a narrower distribution of particle sizes will benefit sintering and final densification, and a subsequent study on alumina powders[52] supported this idea.

The local arrangement of fine particles determines the coordination number of the enclosing pore and significantly affects the local densification behavior (“sinterability”). For a highly coordinated pore, grain growth is required to reduce the coordination number for sintering to proceed. On the other hand, particle rearrangement may also occur to create more interparticle contacts and facilitate mass transport[53]. It should be noted that although these works mentioned above took into account the geometric changes in local microstructure, the models developed were merely able to describe the initial and intermediate stage of sintering. The premise in these stages is that the pores are located at all the triple- or multiple-junction of grains, hence the diffusion distance of an individual pore will be no larger than a single grain, if the grain or GB is regarded

as the vacancy sink of pores. This may not be the case, especially in final stage sintering because not all grain corners will contain pores. In fact, in a microstructure with heterogeneous pore size distribution, small pores tend to have higher densification kinetics which will result in preferential elimination during final stage sintering. Once the small pores disappear, the separation between pores is multiplied and the diffusion distance is no longer approximated by the average grain size. According to Herring's scaling law[54], the normalized densification rate is highly dependent on grain size:

$$\frac{d\rho}{\rho dt} = F(\rho) \frac{\gamma\Omega}{GKT} \frac{\delta D}{G^3} \quad (2-11)$$

Where γ is surface energy, Ω – atomic volume, δ - grain boundary thickness, and G – grain size. It can be readily inferred that the multiplication of pore separation will result in extremely sluggish densification as if the sintering process is stalled. So far, few studies focused on microstructural heterogeneity in final stage of sintering and there has been little modeling with the consideration of microstructural heterogeneity and pore elimination. This phenomenon has been proved in the observation of sintered $ZrO_2 - 3 \text{ mol}\%Y_2O_3$ and alumina powders[55,56] via 2D tessellation techniques. It was concluded that the “effective diffusion distance” required for the pore vacancies to travel prior to merging into a sink is nowhere equivalent to average grain size, hence large pores shown in Figure 10 are more persistent in final stage of sintering comparing with model predictions.

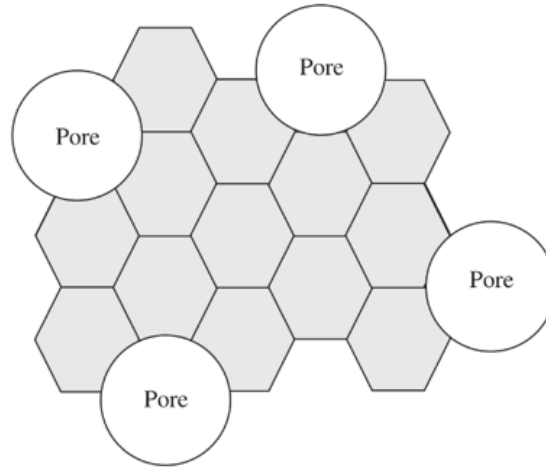


Figure 10. A sketch of remnant large pores in final stage sintering. The effective diffusion distance, in this case, is two times the grain size[55].

As pointed out previously, the defects introduced in BJ3DP systems during printing are even more heterogeneous and larger in length scale comparing to traditional P/M methods. It can be anticipated that without extensive rearrangement of particles and grain growth, the printing defects are likely to remain in sintered microstructure even after prolonged sintering. These large remnant pores could easily be the site of crack initiation and become the main reason of high cycle fatigue failure.

2.2.3 Supersolidus Liquid Phase Sintering (SLPS) and Differential Sintering

The melting point of ceramics is usually far above the solid-state sintering temperatures used for densification. For P/M metals and alloys, however, the relatively low melting temperatures of the system make it possible to partially melt the exterior of powder particles and introduce a liquid phase in sintering above the solidus. If the solid phase is at least partially soluble in liquid, and the liquid wets the particle surface, then such a scenario is called liquid-phase sintering (LPS).

Typically, LPS is achieved by mixing of two powders with different chemical compositions hence different melting points. Once heated to a temperature between the two melting points, one species of powder will melt and form liquid which speeds contact flattening and fills the remaining pores[57]. On the other hand, if one alloy powder is used and heated up to a temperature between the liquidus and solidus temperatures, such a process is called supersolidus liquid phase sintering (SLPS). Unlike LPS where liquid is formed in the interstices between more refractory particles, liquid formed around grain boundaries in SLPS and lowers the viscosity at particle contacts for particle sliding. This will greatly facilitate particle rearrangement to optimize the powder packing efficiency, so that the packing density can increase. Then contact flattening and densification will occur by liquid phase sintering. Comparing with LPS, SLPS that subsequently achieves equilibrium in the solid state produces a monolithic material and hence the potential negative impact of LPS, such as the decrease in mechanical properties due to the introduction of low-melting point second phase, is prevented.

There is a considerable amount of work done by German et al. on LPS, SLPS, and transient liquid phase sintering[58]. German's work on SLPS emphasizes on the capillary forces due to the wetting liquid that is responsible for agglomeration and the rearrangement in liquid phase sintering. More importantly, at low contact angles, Hwang et al.[57] ran computer simulations and showed in Figure 11 that the capillary force, at a constant normalized liquid fraction, is highly dependent on the relative size ratio of adjacent particles. This may suggest that under the condition of SLPS, the co-existence of large and small particles may actually benefit the rearrangement and further densification. A more recent computer simulation[59] suggests that the key factor to complete densification is to ensure the liquid coverage of the grain boundaries.

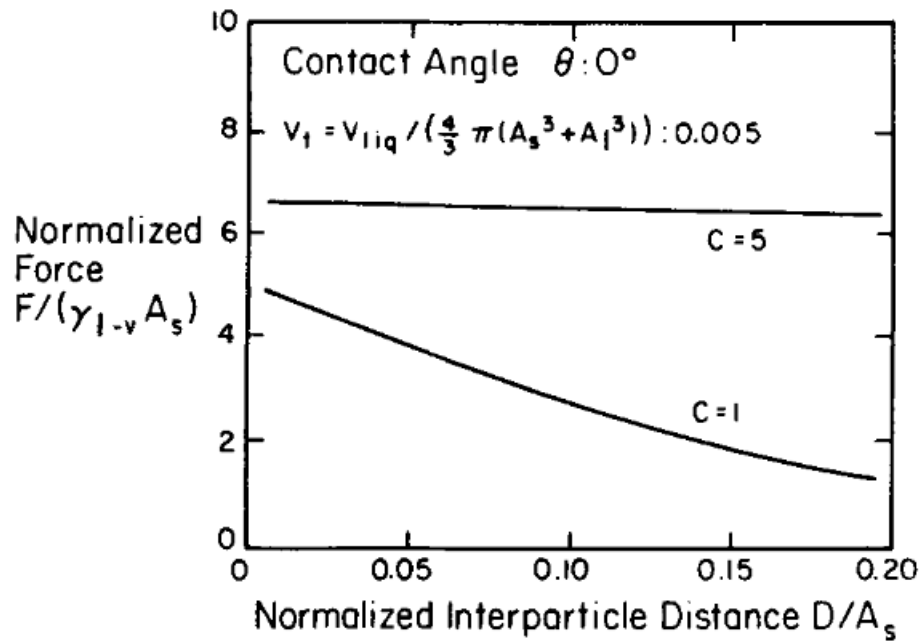


Figure 11. The capillary force acting between two spheres connected by a liquid bridge as a function of interparticle distance. Value C corresponds to the ratio of adjacent particle sizes. [57]

Due to the heterogeneous microstructures, the locality of a powder compact can sinter at different rates, referred to as differential sintering. This can happen in a variety of circumstances, including external stress, constrained sintering, or pressureless sintering of a material with density gradient. Kanters et al.[60] summarized a few scenarios of differential sintering and a schematic illustration is shown in Figure 12. For the case of BJ3DP materials, it lies between the case (c) and (d), where one single material constitutes periodic density gradient along Z-direction.

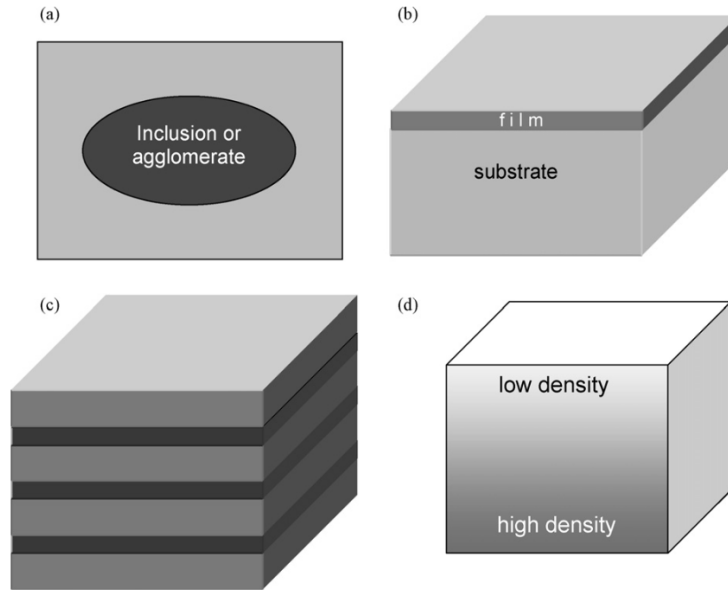


Figure 12. Schematic illustrations of structures undergo differential sintering.[60]

Most of the studies on differential sintering focuses on the co-firing of composite materials, such as metal-ceramic composite or duplex ceramics. In most cases, the origin of the differential sintering comes from the planar constraints, such as co-firing of an low temperature co-fired (LTCC) substrate. Not in all the cases does one see the significant effect of differential sintering. Kanters et al.[60] simulated a co-firing of laminates consisting of two different nanocrystalline zirconia, and found that although there is a difference in pore size distributions at the intermediate stage sintering (71.5% density), both materials reached full density just as free sintering. The final microstructure, including grain sizes, is also the same. Little work has been found investigating differential sintering of metals, since in traditional P/M techniques, a high pressured is usually applied during powder compaction, that exceeds the yield strength of the metal particles and collapses all possible local pore heterogeneity. As a result, P/M green bodies only involves particle interstices and have high green density.

Traditionally, the microstructure characterization of differential sintering is conducted by microscopy. Recently, CT has seen a lot more applications in characterizing pore structures caused

by differential sintering. Okuma et al.[61] use a combination of micro- and nano-CT to observe sintered alumina granule compacts (see Figure 13). They concluded that the pores tend to orient along the direction of compressive stress, which is also demonstrated by traditional 2D characterization in a separate study[62].

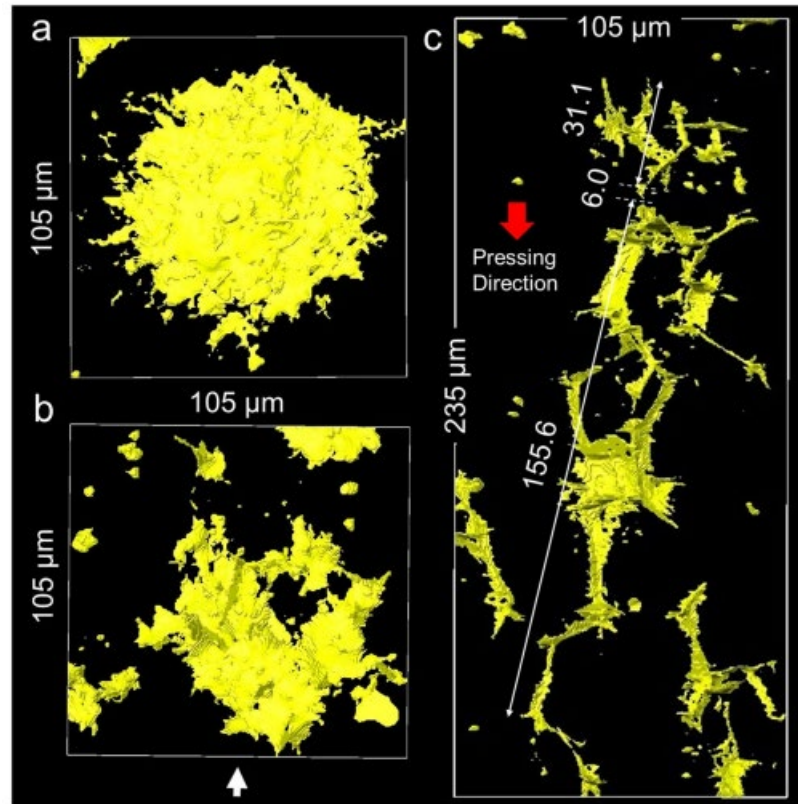


Figure 13. Reconstructed pore network in a sintered α -alumina granules. Image adopted from [61]

2.3 Microstructure Characterizations and Analysis Strategies

2.3.1 Quantitative Stereology

For sintered material, the characterization will focus on remnant pores therefore the feature size equals the pore size of the specimen. In P/M due to relatively large powder size the pore size usually ranges from 1-100 μm and can mostly be characterized via optical microscopy (OM). Quantitative stereology provides a means of obtaining averaged field measurement results. It is the generalized body of methods for quantitative characterization of three-dimensional microstructure features by characterizing two-dimensional section. The assumption beneath this methodology is that the features one intends to capture is isotropic throughout the specimen. For anisotropic features such as elongated grain size, one should follow some designated procedures and to observe sections from a variety of orientations[63].

There are several basic measures in any stereology, namely point count P_P , line length L_L , area fraction A_A , and from which one may infer the ultimately desired measure volume fraction V_V . If the features are randomly oriented and isotropic, these measures should be identical in values:

$$P_P = L_L = A_A = V_V \quad (2-12)$$

Surface area density is another common measurement in pore characterization and is usually obtained by boundary intercept method[64]. A test line is applied to the section and point count P_P is measured when this line segment intercepts a feature boundary. Then the point count is normalized by the length of segment, giving point count density P_L . Finally, the surface area density S_V is two times point count density:

$$S_V = 2P_L \quad (2-13)$$

For sintering of a single-phase material, there are two types of surfaces which are grain boundary and free surface of pores, denoted by S_V^{SS} and S_V^{SV} , respectively. Several studies of surface area densities have been reported across different materials[65–67].

Commonly it is critical to examine the pore size in sintered materials, as it determines the remnant pore size during final stage of sintering as well as controls mechanical behavior of the final product. By combining point count and surface area densities measured, the mean pore intercept length $\bar{\lambda}^V$, which is essentially pore size, can be calculated as:

$$\bar{\lambda}^V = \frac{4(1-V_V)}{S_V^{SV}} \quad (2-14)$$

Similarly, the average grain size $\bar{\lambda}_g^S$ can be calculated assuming no pore detachment occurred, i.e., the pores are on grain boundaries:

$$\bar{\lambda}_g^S = \frac{4V_V}{S_V^{SV} + 2S_V^{SS}} \quad (2-15)$$

Note that in a single-phase material, if a line is put on the micrograph, the microstructure is essentially an alternating pattern of pores and grains. Therefore, the average pore separation, which is the average distance between the boundaries of two adjacent pores, $\bar{\lambda}_p^S$, is similar to the expression of mean pore intercept length:

$$\bar{\lambda}_p^S = \frac{4V_V}{S_V^{SV}} \quad (2-16)$$

Finally, by directly counting the number of pores/grains in the field of view, one may obtain the number of features per unit area N_A . This is a direct reflection of pore and grain population density. A more complex combination of these microstructure parameters, usually compiled as a function of density, can describe the evolution of pore and grain features in what are called microstructure pathways.

2.3.2 Field Measurements vs. Feature Measurements

Quantitative stereology is the method of measuring average properties across the field of interest in a micrograph. However, local heterogeneity usually exists in a sintered porous material and parameters calculated using the methods above will conceal such heterogeneity. Naively using these parameters in sintering analysis will likely lead to misunderstanding of microstructure evolution and kinetics of the examined material. For example, simply investigating the average grain size, surface fractions and pore-to-grain surface ratio is incapable of reflecting the difference in microstructural changes for differently treated slip cast alumina[66]. Moreover, the boundary intercept method is incapable of measuring attributes of individual features especially shape, which is a well-known factor that is critical to pore shrinkage or coarsening[53]. Therefore, individual feature measurements become necessary that can accurately reflect properties of individual pores in the 2D section.

Nowadays, it is much easier to analyze feature parameters with digitized micrograph image and a few open-source image analysis software packages. For shape factors, there are commonly four descriptors that can be readily computed: circularity, solidity, aspect ratio and roundness. Circularity C is defined as the degree to which the particle is similar to a circle and is a comprehensive measurement of particle form and roughness:

$$C = \sqrt{\frac{4\pi A}{P^2}} \quad (2-17)$$

Where P is the perimeter and A is area.

Solidity, in 2D, is defined as the fraction of the area of an object A divided by its convex hull area A_C . The convex hull of an object is an “envelope” surrounding the object that has convex perimeter everywhere throughout the envelope. Solidity S is expressed as:

$$\mathbf{S} = \frac{A}{A_c} \quad (2-18)$$

Aspect ratio is the ratio of the Feret's minimum length to the Feret's maximum length:

$$\mathbf{AR} = \frac{x_{F \min}}{x_{F \max}} \quad (2-19)$$

Feret's minimum length and maximum length refer to the shortest and longest distance between any two parallel tangents on the object shape, respectively.

Finally, roundness is the inverse of aspect ratio:

$$\mathbf{Round.} = \frac{1}{AR} \quad (2-20)$$

Aside from these common shape descriptors, features such as local curvature and connectivity may also be computed using developed algorithms. It should be noted that curvature is rather vulnerable to pixelated object boundaries hence requires a robust algorithm of computation. A number of works have been done to calculate local curvature with improved robustness.[68,69]

There has been extensive usage of feature measurements in cell biology, such as the identification of bacteria and cell growth[70][71]. However, only a few studies have been performed on investigation of sintering behavior using specially designed feature measurements in 2D. Nellros et al.[72] developed an automated measurement process to determine sintering degree via analyzing optical micrograph sections of iron ore pellets. In this work the joint neck area, neck radii and their population, as well as curvature distribution have been computed. An analysis of the microstructure evolution of 625 alloy during sintering has been done and will be explained in preliminary work section, which demonstrates the feasibility of using shape descriptors.

2.3.3 Statistical Approaches

Feature measurements and microstructural pathways combined are able to reveal microstructure evolution when the feature in the observed section is homogeneously distributed. However, for heterogeneous features such as locally clustered pores or particles, these measurements are incapable of representing the effect of local microstructure on densification or grain growth. An example would be the investigation of slip cast alumina. Nettleship et al.[66] calculated stereological parameters and plotted several microstructural pathways, but found that these measurements, at grain scale, were unable to explain the difference in densification behaviors of dispersed and flocculated alumina powders. The difference was later explained by McAfee[73] who applied pore boundary tessellation to the sectioned micrograph and plotted the microstructural pathway in cell maps. The CA-SAF (cell area-solid area fraction) map indicated that the particle rearrangement early in intermediate stage sintering for dispersed system is much faster than that in the flocculated system. An illustration of tessellation is shown in Figure 14[74], and the plot of CA-SAF map is shown in Figure 15.

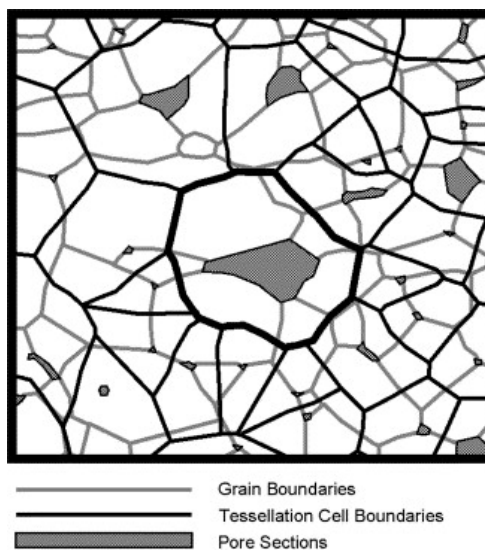


Figure 14. A sketch of pore boundary tessellation.

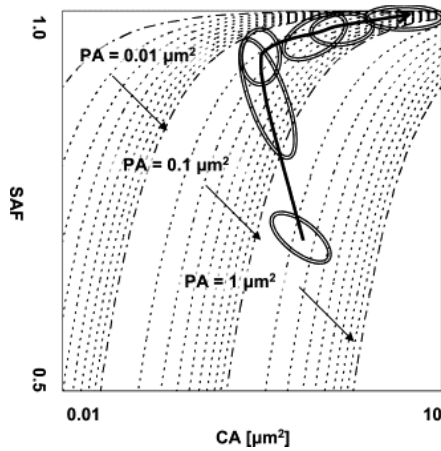


Figure 15. The CA-SAF plot for sintered alumina[74], showing the two systems took different pathways during sintering.

In a binder-jet printed powder system, as stated previously, the population of defects and pores is highly heterogeneous. Moreover, the fatigue behavior also relies on the maximum remnant pore size rather than the mean. Therefore the necessity of using statistical approaches in microstructure description as well as in establishing structure-property relationships has to be addressed.

Since in many cases the field measurements are incapable of reflecting the detail of porous microstructures and there are a large number of features in one field, these observations must be presented as a distribution. For a single feature such as particle or pore size, a histogram or density plot can be used and such distributions from different samples can be stacked to qualitatively show the trend. However, for some microstructural pathway plots it is difficult to plot one distribution against another even in a 3D space. In this case a distribution fitting should be performed which abstracts the distribution into a few descriptive parameters (such as mean and deviation), then the microstructural pathway can be plotted separately. This is rarely done and so there are very few microstructural pathways for feature measurements. Another issue is that typically both PSD and pore size distribution is heavily skewed towards the fine end, and improper binning will bias the

distribution. To tackle such problem a maximum entropy method may be used is a single mode can be assumed[73]. Again, this is rarely considered and so there are no microstructural pathways for feature measurements in sintering.

2.4 Three-dimensional Characterization via Micro-computer Tomography (μ CT)

2.4.1 Advantages of Three-dimensional Characterizations

Bias in two-dimensional sectioning is somewhat inevitable in highly heterogeneous samples. There are two sources of bias found in quantitative microscopy: sampling bias and systematic bias. Removing sampling bias requires a sufficient amount of sampling sections and areas collected. In biological microscopy, the largest variability (70%) comes from that of inter-individual object such as cell or bacterium, and the variability between sections and fields take up approximately 8%; In material science such distribution of variability leans more towards sections, fields and measurements so it require more effort in sampling and micrograph acquisition[75]. However, in many cases in material science this is not practical. However, high-temperature alloys such as nickel-based superalloys can be ground and polished to create new sections in the same sample, but the grinding/polishing process can be quite tedious depending on the grinding and polishing characteristics of the alloy. Hence it is a widely accepted compromise that one can take the results of quantitative measurements from only a few sections and fields of view as representative of the entire specimen if there are no noticeable biases such as microstructural gradients. For a specimen with layered structures such as a binder-jet printed green body, if it is sectioned along the building direction (z-axis) then the chance of capturing these large interlayer

defects will solely depend on the location of sectioning. With limited number of sections observed it is impossible to obtain the actual population of pores and defects in the whole green body. The preliminary results in the examination of a binder-jet printed silicon carbide sample demonstrated such bias.

Systematic bias in quantitative measurements can sometimes be difficult to notice and can misrepresent the microstructure. For example, an individual three-dimensional feature can be sectioned by an arbitrary measurement plane that goes through it, but the chance of capturing the representative size of that feature is low. In fact, it is impossible to tell from a 2D section that if the cross-section of that feature corresponds to a small fraction of the feature or a majority of it. An example of this bias is shown in Figure 16[76]. Sectioning may result in the same cross-sectional area, but the features in 3D have variable sizes.

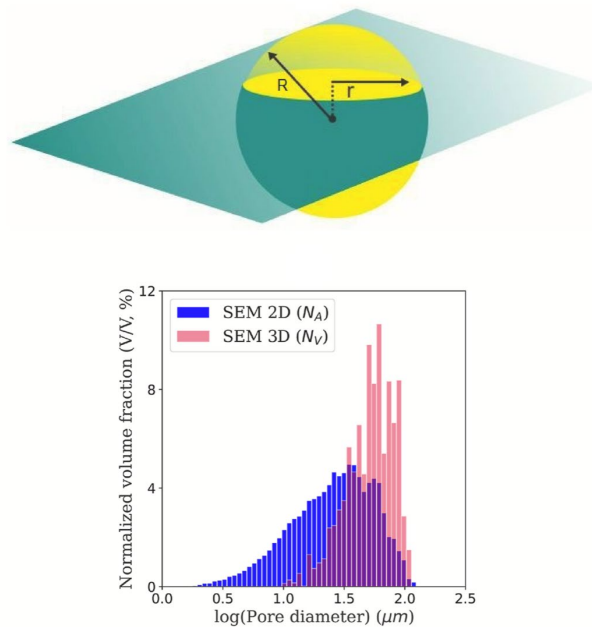


Figure 16. Sectioning a sphere with a plane that does not pass through the geometric center.

In order to extrapolate 2D measurements into 3D space and obtain true convex feature measurements in 3D, one approach is to assume a specific distribution model, such as normal,

lognormal, Weibull or gamma distribution[77] and use some fitting model to infer the actual distribution. An alternative method is to use a forward method[78–85] which compares the measured 2D distribution with “pseudo-sections” created by computer simulation for different types of distributions. Then the computer takes iterations to compare these data until a best match is found. Furthermore an advanced method developed by McAfee[73] that used information entropy method to enable the generation of distribution function without explicitly defined distribution models[86–90]. All these methods are not a direct measurement of features in 3D space and require shape and distribution assumptions. If there is anisotropy due to grain elongation or anisotropic pore shapes with unknown orientation, such sectioning will fail to reflect actual distributions of the features even with advanced fitting methods.

Obviously, a direct 3D measurement will easily resolve the bias associated with 2D sectioning. For acquisition of 3D micrographs, the method can either be destructive, such as serial sectioning or FIB-SEM, or non-destructive, such as computer tomography (CT). It is obvious that non-destructive methods have inherent advantages such that one may preserve the specimen for further measurements. The acquired 3D image is either an assembly of 2D images or can be easily re-sliced into a series of 2D sections in an almost arbitrary manner, providing extreme convenience for cross-validation with 2D micrographs. Another advantage of 3D imaging is the precise measurement of topological parameters that are inaccessible in 2D. For example, it is not possible to determine if a pore section detected on a two-dimensional measurement plane is from a closed pore or from a continuous pore channel that enters and leaves the measurement plane numerous times. Only 3D analysis can determine the number of pores directly.

2.4.2 Introduction to Computer Tomography (CT)

Computer Tomography (CT) is one of the most widely used imaging technologies in three-dimensional characterization especially in biomedical applications. The word “tomography” refers to “the cross-sectional imaging of an object from either transmission or reflection data collected by illuminating the object from many different directions”[91]. The most commonly used light source for illumination is X-ray since the photon has sufficient energy to penetrate an object and create a response on the screen or film. In an X-ray CT there are several key components: the radiation source, various hardware filters, an object mount and a detector that captures the attenuated photons. For biomedical CT the object is usually a patient, Typically the resolution for human body CT is 0.625-1.25 mm[92]; for CT used in materials science, the object is much smaller hence the resolution can be much higher than regular CT at the range of 0.3-1 μm , hence called micro-computer tomography (μCT).

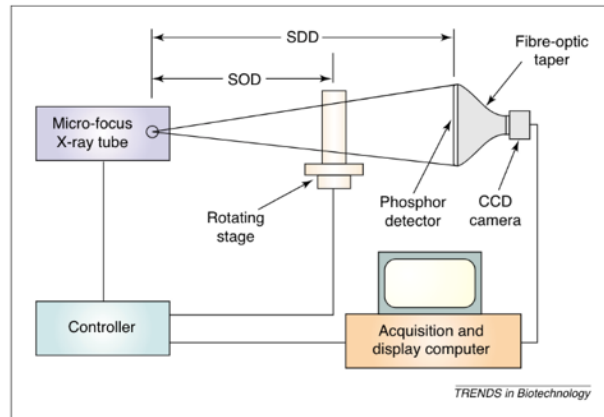


Figure 17. A basic setup of μCT . Image adopted from [93]

A basic layout for μCT is shown in Figure 17[93]. The X-ray source is generally a vacuum tube that contains two electrodes, which is made of tungsten spiral as in a light bulb (cathode), and a positively charged anode (target). The current-heated cathode emits free electrons, which are

accelerated by the potential difference between two electrodes. The potential turned into kinetic energy of the free electrons, and eventually converted to photons when the electrons hit the target. For a 20-150 kV potential the energy of the photon lies within the range of X-ray.

When an X-ray photon penetrates an object there are two mechanisms that contributes to the attenuation: photoelectric effect and Compton effect. Photoelectric effect is the conversion of photon energy to excite an electron in the atom to its free state. Compton effect is a deflection of photon caused by the interaction with an electron. The decay of photon energy caused by these two effects can be combined as a constant photon loss rate μ . If a number of photons are shot through the object, then the number of photons one may collect as a function of their travelled distance can be given by[94]

$$N(x) = N_0 e^{-\mu x} \quad (2-21)$$

Where N_0 is the number of photons entered the object and x is the distance. In a two-dimensional case, the loss rate μ is a function of space coordinates x and y , hence

$$\int_{ray} \mu(x, y) ds = \ln \frac{N_{in}}{N_d} \quad (2-22)$$

Where N_{in} is the number of photons entering the object and N_d the number exiting the object. It is rigorously proven that with enough linear projection data (attenuation ratio), $\mu(x, y)$ can be explicitly determined[95,96]. The next step is the conversion of $\mu(x, y)$ to the atomic number of the locality (x, y) . Multiple studies have been done in establishing such relationship via experimental measurements and theoretical modeling in body CT[97]. Denison et al.[98] modeled the relationship between the loss rate and the effective atomic number Z as

$$\mu = \rho \left(a + \frac{bZ^{3.8}}{E^{3.2}} \right) \quad (2-23)$$

Where a and b can be regarded as constants, ρ being the electron density at point (x, y) , and E being the energy of incoming beam. From the effective atomic number it is easy to calculate

the density at point (x, y) . Finally, the reconstructed image is generated by mapping local density to an 8-bit grayscale (256 levels) for each pixel, forming a three-dimensional grayscale image. A side projection of a silicon carbide object and one reconstructed slice in x-y plane is illustrated in Figure 18. After the reconstruction the slices are assembled into a 3D volume. The visualization of such 3D volume can be either via volume rendering or surface rendering.

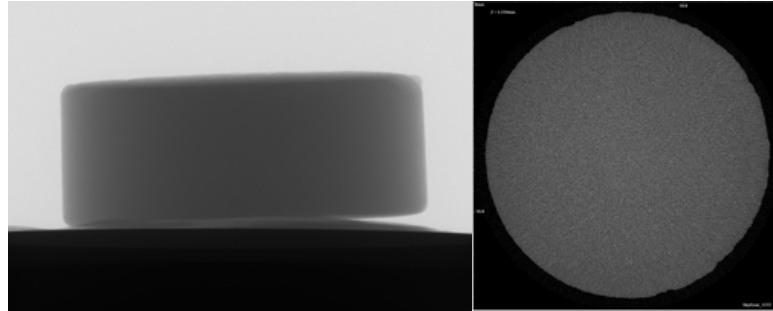


Figure 18. A CT-scanned silicon carbide pellet. (a) side projection; (b) a reconstructed slice.

2.4.3 Applications of Micro-computer Tomography in PM and Sintering

A number of works have been done using μCT to investigate mesoscale microstructures, especially in porous systems. The first study carried out by Jasti et al.[99] was on glass bead packs and Berea sandstone. The reconstructed image showed good contrast between pores and solid phase. Other works including the characterization of porous ceramics[100], sprayed titanium coatings[101], quality control of additive manufactured metals[102–105], fracture and corrosion[106][107], to name a few.

The interest in CT-characterization of porous structures in sintered materials is increasing in recent years. Bernard et al.[108] reported the first direct visualization of pore structure evolution during the sintering of soda-lime glass powder (Figure 19). Vagnon et al.[109] performed statistical analysis on sintering of copper powder and reported microstructural measurements (neck

size, coordination number, and pore size distribution) in 3D. Olmos et al.[110] acquired in-situ CT images during the sintering of heterogeneous copper/alumina powder mixture. Wakai et al.[111] reported spatial anisotropy in a viscous flow sintered glass film. Such anisotropy is reported to be undetectable or heavily biased via 2D sectioning methods.

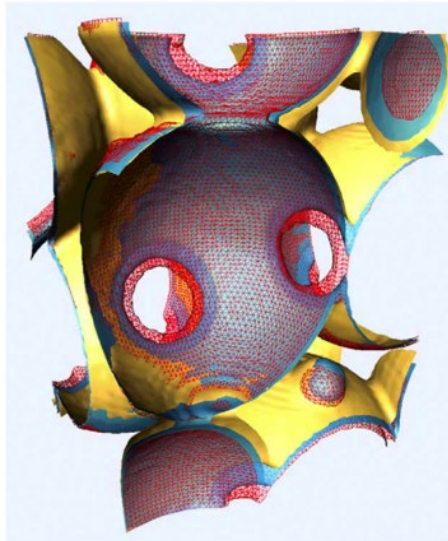


Figure 19. Visualization of soda-lime glass grains under sintering colored mesh shows grain growth and coalescence at different sintering times (red – 20 min, blue – 90 min, yellow – 120 min).

2.5 Rationale for This Work

The rationale of this work originated from the preliminary experiments done by Mostafaei et al. and analyses by the author. In the preliminary work, nitrogen-atomized 625 alloy powder with a PSD of 16-63 μm was binder-jet printed using an ExOne X-1 Lab printer, and subsequently cured and isothermally sintered below and above solidus temperatures (1270 °C and 1285 °C, respectively). Details of the experimental and analysis methods can be found in the published reference[112]. It was found that under subsolidus temperature, solid-state sintered samples could

merely reach a final density of $\sim 85\%$. Densification essentially stalled after 2 h after reaching isothermal temperature. On the other hand, samples sintered above solidus temperature reached a high final density above 99% after 12 h. In fact, sample densities were above 95% after 4 h supersolidus sintering, indicating a much more efficient densification. Figure 21 shows density progression during sintering and optical micrographs showing final microstructures are shown in Figure 20.

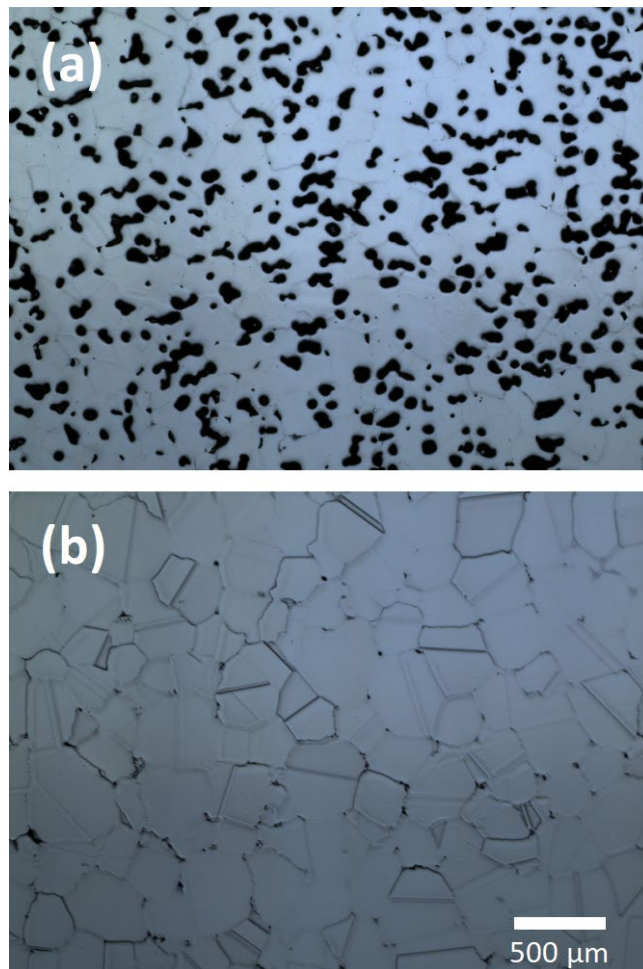


Figure 20. Optical Micrographs for binder-jetted 625 alloy sintered at (a) 1270 °C and (b) 1285 °C, both for 12 h.

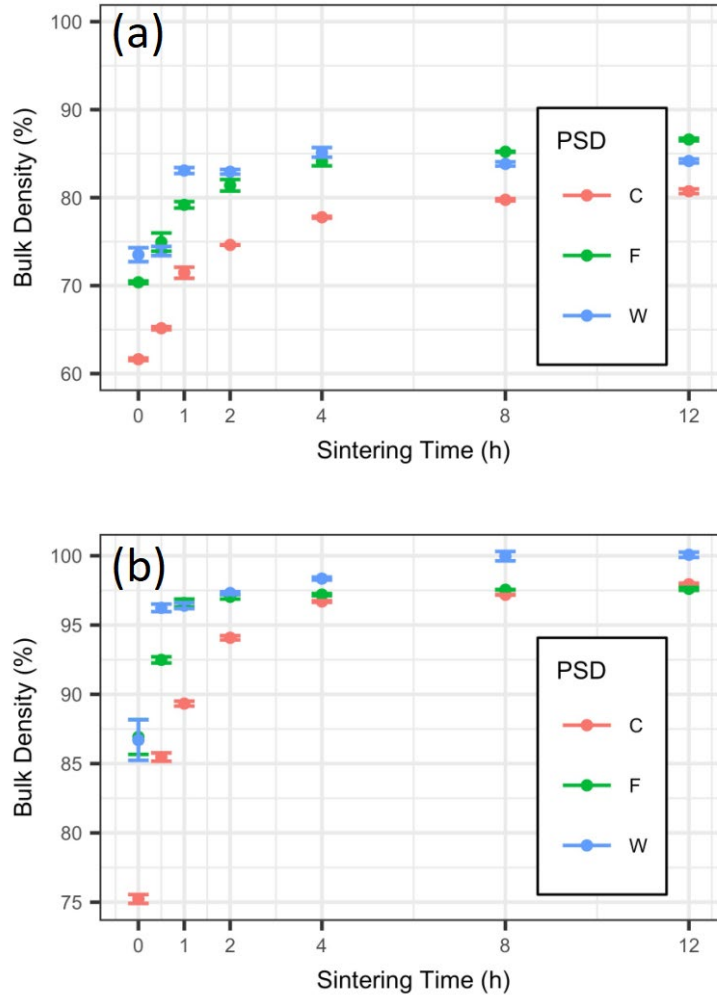


Figure 21. Archimedes densities for 625 samples sintered 0 – 12 h. (a) 1270 °C; (b) 1285 °C. In this study, refer to powder W for 16-63 μm PSD. [112]

A detailed individual feature measurement on pores was conducted on optical micrographs for different times and temperatures of sintered samples. Distribution density plots for pore area are shown in Figure 22. Here, one may clearly see how large pore sections evolve as a function of sintering time. For subsolidus sintered samples, there was a continuous right shift of the peaks as sintering time prolongs. This indicates a preferential removal of small pore sections in the microstructure, although from (b) where the absolute number of pores was plotted against sizes, that overall porosity is decreasing. Finally at 12 h a small number of relatively large pore sections,

with pore area of 1,000 – 10,000 μm^2 , remained in the final microstructure. On the other hand, the peak for supersolidus sintered samples remained small, averaging between 10 – 1,000 μm^2 throughout isothermal sintering up to 12 h. This is an indication of pore section removal of both large and fine pore sections. Especially at the first 0.5h, pores larger than 1,000 μm^2 were removed rapidly, which was distinctly different from subsolidus sintering.

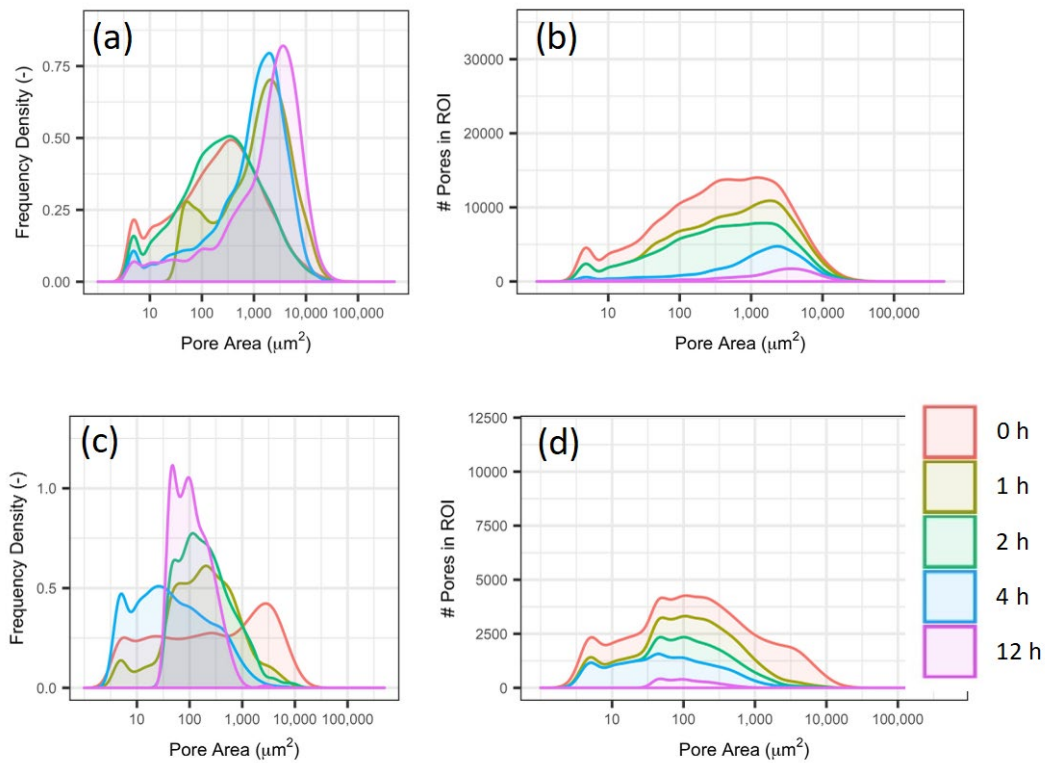


Figure 22. Pore area frequency distribution for (a) (b) subsolidus and (c) (d) supersolidus sintered 625 alloy.

(a) (c) show relative frequency distributions whereas (b) (d) show absolute pore number count in the microstructure. Figure edited from [112]

Based on these observations, the difference in densification behavior between super- and subsolidus sintered 625 alloys can be explained by the occurrence of particle rearrangement during SLPS. A schematic is shown in Figure 23. Since the interlayer spacing (boxed with dashed lines) in a binder-jetted material is more porous than each jetted layer, the powder particles are thought to rearrange in this region more likely. In microstructure path (b), supersolidus temperature allows

the formation of viscous liquid, which enables rapid particle rearrangement. Small particles will displace and relocate into cavities which used to be packing defects. Hence, large packing defects will collapse quickly and the microstructure will be homogenized. The later densification is also greatly accelerated thanks to the homogeneous microstructure even with conventional mass transport mechanisms. While samples sintered SLPS reached high final density, heavy chemical segregations were found via SEM-EDS in the final microstructure, where fast-diffusing elements, such as Nb and Mo, segregated significantly towards secondary phase between grains (see Figure 24). For subsolidus sintered samples, in microstructure path (a), densification kinetics solely rely on the neck growth via solid-state sintering mechanisms, where small pores are preferentially removed, resulting in locally heterogeneous microstructure that is detrimental for further densification. The fact that powder W sintered to a higher final density compared to narrower PSDs may also be explained by German's work, that a wider range of PSD effectively increases value C hence the capillary force is larger in samples made by powder W, especially in the low-density printing defect regions, where particles are farther away from each other.

Since in path (b) the particle rearrangement only occurs in very short time, it is reasonable to infer that supersolidus temperature is only required during the time span of rearrangement. Therefore it is possible to design a process that combines the advantages of super- and subsolidus sintering so that the binder-jetted material is able to fully densify while avoiding the formation of secondary phases and accompanied chemical segregation. Such hypothesis can be backed up by German's work, that a transient liquid phase may be present under certain conditions that allows for the segregated elements to diffuse back into bulk. (Supersolidus-Transient Liquid Phase Sintering Using Superalloy Powders). Another question remains unsolved in the preliminary work is, characterization on 2D sections can only explain the densification mechanisms with the

microstructure involves interlayer spacings, but not printing lines or other type of defects in the green structure. It is impossible to know whether SS or SLPS can repair printing lines in XOY plane. In other words, one may not conclude which type of printing defects contributes to the majority of remnant porosities in a sintered structure. This constitutes another motivation of this work: to distinguish different printing defect types and their evolution during sintering.

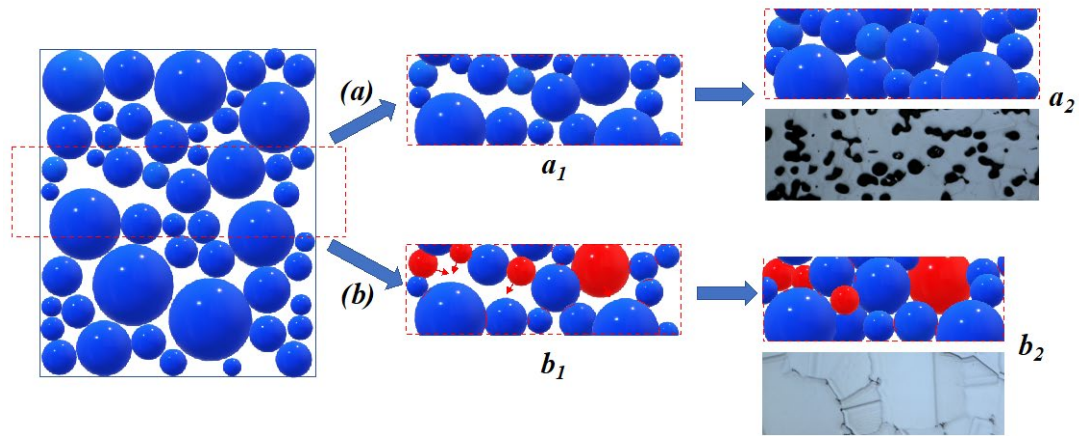


Figure 23. A schematic illustrating densification and particle rearrangement mechanisms for (a) SS and (b) SLPS. Adopted from [112]

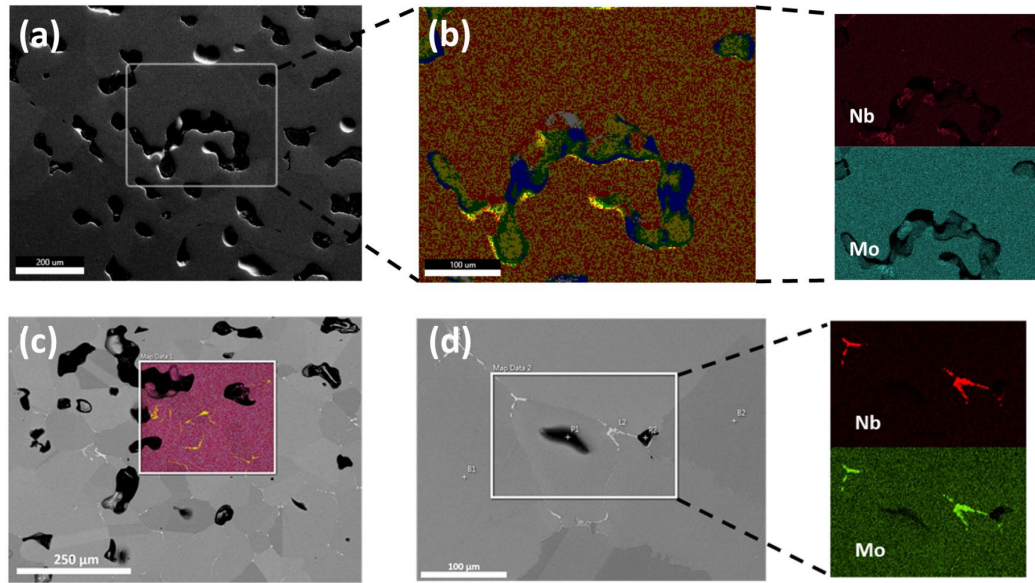


Figure 24. SEM-EDS elemental maps for (a) (b) subsolidus and (c) (d) supersolidus sintered 625 alloy. Figure adopted from [112].

3.0 Hypothesis

1. A two-step viscous rearrangement assisted (VRA) sintering process is proposed in this work. It is believed that the key to rapid densification in a highly heterogeneous microstructure is first facilitated by the collapse of large pores due to the liquid generated in grain boundaries, which results in substantial rearrangement of particles under surface tension and hence reach higher packing efficiency, while preserving small pores as particle interstices. In such way, in the first stage of supersolidus sintering the large pores are preferentially removed but the effective diffusion distance does not rise rapidly. The second step of sintering is to lower the temperature such that the sample undergoes solid-state sintering, to completely remove remnant small pores. The long time in solid-state sintering will help the re-dissolution of highly segregated elements in liquid phase back into the grain and eventually reaches chemical equilibrium.

2. Preliminary results show three types of printing defects which may result in remnant porosity in the sintered microstructure, which includes regular packing defects (random packing defects and particle interstices), printing lines in XOY-plane (ballistic ejection of the binder droplets), and interlayer defects (due to spreading of powders in Z-direction). It is hypothesized that these defect types do not contribute equally to the remnant porosity in the final microstructure. It is likely that regular random packing defects can be removed via subsolidus sintering, while the printing lines and/or interlayer defects are only able to be removed by supersolidus sintering. Therefore, the control of printing lines and/or interlayer regions are more critical in controlling final sample qualities than controlling random packing defects.

4.0 Objectives

1. Demonstrate that a two-step VRA sintering is capable of producing a fully dense binder-jet printed material. The second step in VRA sintering, namely low-temperature solid state sintering, will allow the re-dissolution of highly segregated liquid phase and reach a chemically homogenous microstructure by the end of sintering process. This can be verified by density measurements using water immersion method. The chemical homogenization is verified by EDS mapping of fast-diffusing elements (Nb, Mo).

2. Demonstrate that μ CT can characterize green microstructures, defects and microstructure evolution during sintering for porous material fabricated by BJ3DP of metal powders. This includes CT scan of green bodies and sintered parts at different time and densities. The accuracy of CT scanning can be verified by comparing Archimedes density measurement results, SEM/OM micrographs and CT-analysis results. If the threshold of reconstructed 3D images is calibrated by Archimedes density, then other field and feature measurements can be used to determine the evolution of the microstructure during sintering.

3. To separate the effect of different defect types in samples' green state that influence the microstructure evolution during sintering and final porosity. Isothermal sintering above and below the solidus temperature will be used to determine its ability to repair each type of defect in the printed green materials. To achieve this objective, three (3) types of CAD model were designed and printed. The first type is regular 625 green bodies, where a full solid cubic shape was printed and the binder will be jetted to cover the full cross-sectional area for each printing layer. The second type is called "skin" where the CAD model is a hollow shape but with closed surfaces, constructing a "skin" of printed materials surrounding a core of spread powder. After printing,

since the volume inside the surfaces cannot be de-powdered, there will be spread but un-jetted loose powders remaining in the hollow volume. Therefore, this type of green body consists of a jetted “skin” and a loose powder “core” spread in layers. The third type is called “crucibles” where a hollow shape is printed but with an opening on the top surface. In this case the loose powder in the core will be extracted after printing and curing, and the same powder will be poured into the cavity to fill this volume. Therefore, this type of green body also consists of a jetted “skin” and a loose powder “core”, but the “core” will not have printing lines nor interlayer defects but only normal packing defects. In this way, three types of defects in the green state can be separated and studied individually during sintering.

4. To establish a process-structure relationship between printing methods, sintering condition and the microstructural evolution during subsolidus, supersolidus, and VRA sintering of binder-jet printed metal powders will be compared using microstructure pathways. This includes 2D/3D quantitative imaging, microstructural pathway parameter acquisition, data correlation and statistical analysis. One or a combination of the pathway parameters will be chosen as a representative parameter that best describes the densification status of the sintered material.

5.0 Experimental Methods

5.1 Synthesis of Samples

5.1.1 Binder-jet Printing of Regular 625 Alloy Green Samples

The synthesis of AM Inconel 625 alloy green bodies was made with an ExOne Innovent BJ3DP printer. Air-melted, nitrogen-atomized 625 alloy powders provided by Carpenter (Carpenter Technology Corporation, USA) were used for all the binder-jet printed experiments. The labeled particle size distribution was 16-53 μm . Particle size distribution of the powder feedstock was characterized using Microtrac Zetasizer S3500 particle size analyzer. It characterizes the particle size using the Mie scattering of laser light. The tri-laser system and multiple compensation algorithms allow the analyzer to measure PSD for the range of 0.02-2800 μm for both spherical and non-spherical particles. Only minor amount of powder is needed to obtain an accurate measurement. A distribution plot was constructed according to the output of the analyzer to control as well as characterize as-received and sieved 625 alloy powders. The measured PSD of gas-atomized and gas-atomized 625 powder (GA) is shown in Figure 25[113].

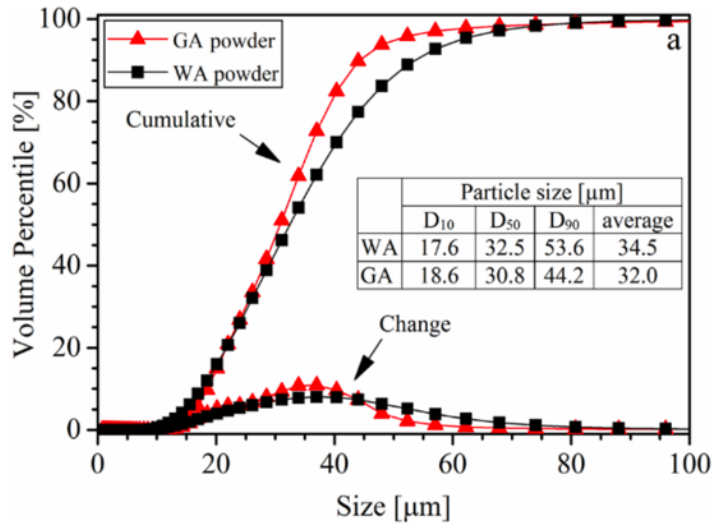


Figure 25. PSD measured for gas- and water-atomized 625 alloy powder. Figure adopted from [114]

The printing parameters were those used previously by Mostafaei’s work for the same as-received powder size distribution[21]. The CAD model of “regular 625 samples” were rectangular cuboids with 1*1 cm base cross-section, with two filleted edges on the top to distinguish printing direction, building direction and rolling direction. This gave the orientations for the microscopy. Since the green bodies were too fragile to be machined or cut in the green state another set of cylindrical samples (diameter 1.5 mm, height 4 mm) were printed using the identical conditions, for the CT characterization.

After printing, the samples were carefully de-powdered and placed in an oven for binder curing. The curing temperature was 200 °C and the time duration was 8 h. The green body characterization methods, including density measurements and CT scanning.

5.1.2 Sintering of Printed Green Bodies

Based on the analyses from the preliminary work on the 625 alloy system, the sintering processes were used as follows: three technical repeats of each sintering condition were placed in

a high-temperature Lindberg Blue (Thermo Fisher, USA) tube furnace under vacuum at the same time. Three groups of samples were prepared, namely VRA group, solid-state sintering (SS) group, and supersolidus sintering (SLPS) group. During the first step of the sintering cycle, the temperature profile followed that of Mostafaei's work[113]: heating from room temperature to 600 °C at 5 °C/min, then to 1000 °C at 3.2 °C/min, and finally 2.8 °C/min to designated temperature (VRA and SLPS group at 1285 °C, SS group at 1270 °C). Once the system reached the designated temperature, a variety of holding times were to perform isothermal sintering experiments. The holding time for three groups are listed in Table 1. For SS and SLPS group, there was only one step for isothermal sintering, after which the samples are naturally cooled down in the furnace under vacuum. For VRA samples, a second-step solid-state sintering was carried out after the first step SLPS sintering, by stopping furnace power output and naturally cool the system to 1270 °C, then hold for a variety of time durations followed by natural cooling to room temperature. Non-destructive measurements, such as density measurement and μ CT, were done prior to destructive characterizations (OM and SEM-EDS analyses).

In normal sintering studies and practices, it is uncommon to compare two groups of samples isothermally sintered with a temperature difference of merely 15 °C. The temperature selection of this work was based on two reasons: 1) sintering under such temperatures has been done by Mostafaei et al.[114]and proven to have radical difference in densification behavior, therefore one should expect similar behavior as long as the furnace temperature is well calibrated and controlled; and 2) In P/M processing, metal powders are usually sintered at a temperature very close to the melting point or solidus line ($> 0.9 T_m$), and under supersolidus sintering one needs to control the temperature such that the shape retention can be kept, especially for AM products. In this work, the tube furnace was carefully calibrated by testing the temperature at the center of the

heating zone inside the tube. A temperature profile was also plotted as a function of distances away from the heating zone, showing a temperature drop of no more than 1 °C within a 6-inch span. Therefore, the samples were considered to sinter reliably just above the solidus temperature.

Table 1 Time durations for SS, SLPS and VRA group samples during isothermal sintering

Group	Step 1 (h)					Step 2 (h)			
	SS	0	1	2	4	8	N/A		
SLPS	0	0.25	0.5	0.75	1	N/A			
VRA	1					1	4	8	12

5.1.3 Printing and sintering of “Skin” and “Crucible” samples

To achieve Objective 3, specific shapes of “Skin” and “Crucible” samples were designed to ensure the accuracy and feasibility of the different characterization methods. For “Skin” sample, a cylindrical shape with a thin tip and a wide base was used during printing. The thin tip was used for CT characterization and the wide base was to ensure stability during sintering, to minimize error when measuring density using the balance, and to enlarge the area of observation under microscopy when the samples were sectioned. For the “crucible” samples, a cylindrical cup shape with an unsealed top was designed to ensure powder extraction after curing.

The printing parameters and curing processes were kept the same as “regular” samples mentioned in section 5.1.1. “Skin” and “Crucible” samples were separated into group SLPS and SS only, since the chemical homogenization process was no longer of interest in this part of work.

The temperature and holding time durations were the same as the regular 625 alloy samples, as indicated in Table 1.

5.2 Microstructure Characterizations

5.2.1 Two-dimensional Characterization

Two-dimensional characterization of this work involves observation of sectioned samples under optical microscopy (SmartZoom 5, Carl Zeiss AG, Germany) and scanning electron microscopy (Sigma 500 VP, Carl Zeiss AG, Germany; FEI Apreo, Thermo Fisher, USA). Sintered samples were sectioned using diamond saw, then ground and polished for observation. The grinding/polishing process were carried out using a Struers Tagramin-25 grinder/polisher (Struers Inc., USA) and the detailed process can be found in[115]. The pore structures were mainly characterized by optical microscopy. To cover as large field of view as possible, a total of 5 sample images were acquired for each polished section. At the lowest magnitude (101X), the resolution of ROI (region of interest) was 1600*1200 pixel with 2.2013 $\mu\text{m}/\text{pixel}$, for a total size of 3522*2642 μm^2 . The generated files were saved in the RGB/CMYK format. For the sake of feature extraction and analysis, the images were converted into grayscale. This was done using the ImageJ software (Fiji version)¹. SEM were set in the backscattered electron mode to reveal secondary phases and heavy segregations from the bulk microstructure.

¹ Fiji is released as open source under the GNU General Public License.

5.2.2 Three-dimensional Characterization

Three-dimensional characterizations were mainly carried out by μ CT scans. The equipment used for the scan was Bruker Skyscan 1272 XRM with a 16-megapixel CCD camera and an X-ray source up to 120 kV, with a resolution up to 0.35 μm in a single image slice. After the scan, the images were reconstructed using the NRecon software and analyzed using CTAn software. The 3D visualization of powder and defects was done using CTVox and CTVol software offered by Bruker. The detailed workflow and algorithms are explained in the Background section. The output of the CTAn analysis was in the format of a text file and could be read and further analyzed using a variety of methods.

5.3 Other Characterizations

5.3.1 Density Measurements

Density and porosity are measured using the water-immersion method based on the Archimedes principle. The sample is first placed on a high-precision balance to measure dry weight m_1 . Then the sample is placed in a basket fully suspended under water and the weight is measured again m_2 (“upthrust”). Finally, the wet sample after immersion in the water is placed on the balance again to measure wet weight m_3 . It can be readily inferred that the apparent density, the density including solid and open pore volume, can be expressed by

$$\rho_{app} = \frac{m_1 \rho}{m_1 - m_2} \quad (5-1)$$

And the bulk density, which takes all the volumes into account, expressed by

$$\rho_{bulk} = \frac{m_1 \rho}{m_3 - m_2} \quad (5-2)$$

The difference between theoretical relative density, i.e., 100%, and apparent density is the closed porosity (cp):

$$cp = 1 - \frac{\rho_{app}}{\rho_{theoretical}} \quad (5-3)$$

and the difference between the relative apparent density and relative bulk density is the open porosity (op):

$$op = \frac{\rho_{app}}{\rho_{theoretical}} - \frac{\rho_{bulk}}{\rho_{theoretical}} \quad (5-4)$$

5.3.2 Chemical Segregation via SEM-EDS

The goal of chemical composition analysis is to track the extent of segregation of alloying elements and precipitation of carbon/carbides near the pore surface and grain boundaries. In the case of 625 alloy, the major segregated elements are Nb and Mo[116]. In this study, only qualitative analysis is necessary to monitor the changes after supersolidus sintering and homogenization treatments. Therefore, a relatively simple SEM/EDS mapping across the 2D micrograph sections was used.

5.4 Statistical Analyses

5.4.1 Feature Measurements

Individual feature measurements can be measured in 2D and 3D. 2D feature measurements can be obtained by analyzing OM images or individual 2D slices from μCT scans. Using ImageJ software, one may compute individual pore sizes and pore shape descriptors. For 3D feature measurements, one may calculate features such as individual pore volume and orientation distribution, pore aspect ratio, surface area, etc., using CTAn software. From 3D scans the topological parameters such as connectivity and Euler number can also be calculated.

For both types of images, binarization is necessary before performing any analysis. In a binarized image, the objects (pores) are segmented from the background (grains). The segmentation process essentially applies a thresholding algorithm to the image, but such algorithm usually requires priori knowledge (i.e., “human judgements”). In this work a ground-truth based thresholding algorithm was used to calibrate the thresholding level using measured bulk density. The advantage of such algorithm is that it has higher precision for 3D images since the image is composed of thousands of 2D slices. Averaging these threshold levels for these slices provided a suitable segmentation of the whole volume. After thresholding, additional denoising filters were applied to remove unwanted speckles, such as dust or twin boundaries on the polished section, or salt and pepper noises in the reconstructed 3D volume. The workflows for 2D and 3D feature measurements are shown in Figure 26.

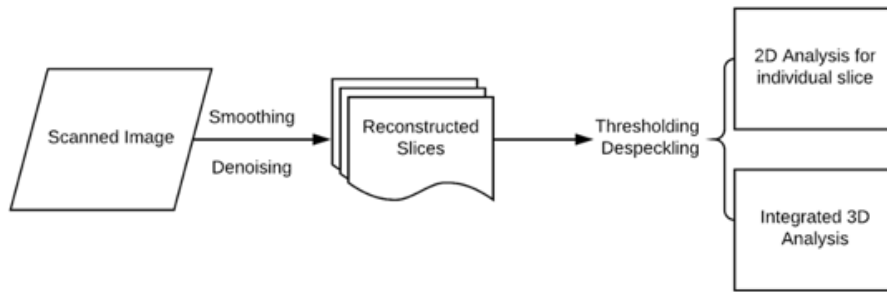


Figure 26. Workflow for 3D image processing and analyses.

5.4.2 2D and 3D Microstructural Pathways

Theoretically, any measurement associated with microstructures can be plotted against another microstructural quantity to form a microstructural pathway plot. However, amongst these plots the dimensionless measures may be of greater interest, since these measures are independent of the absolute sizes of features. A list of possible dimensionless microstructural pathways is shown in APPENDIX. Many such pathways may be realized but the plot of pore size/grain size against density are the only ones widely used in the study of microstructural evolution in sintering. They make intuitive physical sense based on the conceptual understanding of sintering.

5.4.3 Data Analysis and Visualization

Data analysis and visualization were mainly carried out using R language. A few regression models were used, which were included in different packages made available for R. Data visualization was also performed using visualization packages in R (e.g., ggplot2). Visualization of a single feature measurement is commonly accomplished via histograms. In R an improved frequency density plot was created. However, precautions needed to be taken when visualizing

features that are matching the size of a single pixel. Highly pixelated features not only caused false results for the individual feature, but also created unrealistic peaks or valleys in the density plots.

6.0 Results and Discussions

6.1 Regular Binder-jetted Structures

6.1.1 Density and Porosity

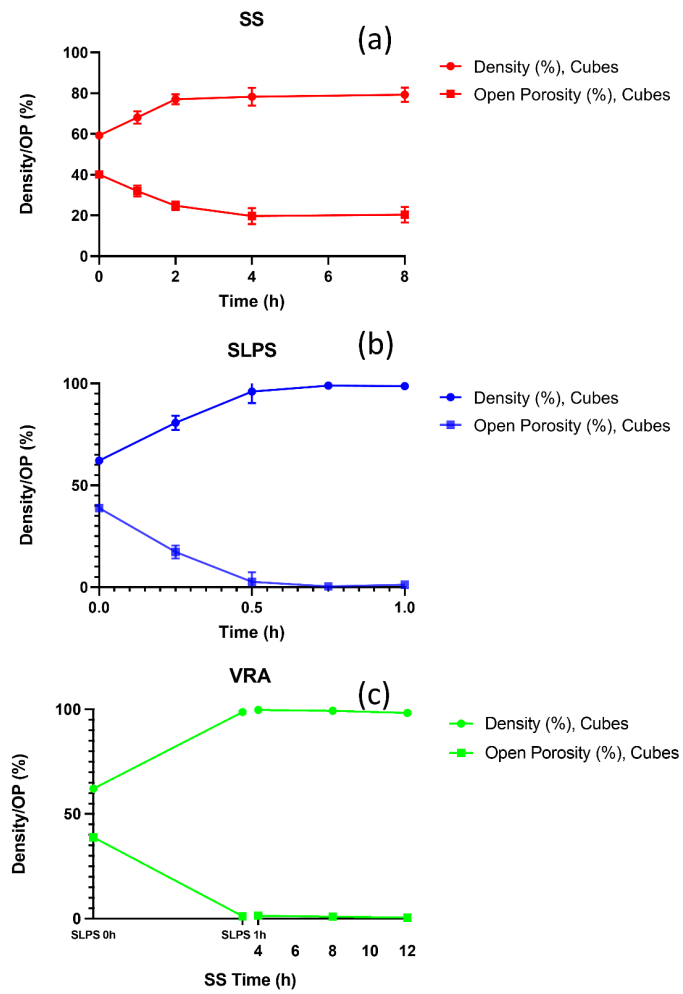


Figure 27. Density and Open porosity measured by Archimedes method. (a) SS, (b) SLPS, and (c) VRA sintering.

Density and porosity, as measured using Archimedes method, are plotted in Figure 27. Density showed a gradual progression as sintering time increases, and accordingly porosity decreases. Green bodies were weighed on balance assuming near net-shape geometry and resulted in an average green density of 55.9%. Due to the nature of green powder compacts all pores are considered open at this point, hence giving an open porosity of ~44.1%.

Similar to Mostafaei's results[117], SS samples showed significant plateauing of densification after 4 h of sintering, with a final density around 79.5%. Accordingly, the open porosity also stabilized at ~ 20% indicating that there was minimal pore closure and the microstructural evolution during sintering stalled at the intermediate stage. SLPS samples showed much faster and efficient densification kinetics comparing with SS samples. There was no plateauing that limits the final density, who reached nearly 100% after only 1 h sintering. Open porosity also was quickly eliminated to below 5% after 0.5 h, showing that the system entered final stage sintering between 0.25 and 0.5 h of SLPS. Similar trend can be observed for VRA samples, that after 1 h SLPS in step 1 the system already fully densified. Therefore the role of step 2 sintering for VRA samples remained only for chemical homogenization. Note that at 0 h of both SS and SLPS samples the densities were both ~ 60%. This indicates that at high temperatures (1270 °C and above), the kinetics for initial densification was so fast that one may hardly tell the difference merely from density data. Therefore what happened in later times during different sintering temperatures determined the final microstructure. Also, using density or porosity as the only indication was incapable of describing the extent of densification under different sintering conditions.

6.1.2 2D Characterizations and Stereology

Figure 28 shows optical microscopy (OM) images for the regular samples sintered under SS and SLPS conditions. The OM images were taken at a magnification of 200X and the scales are uniform among all images.

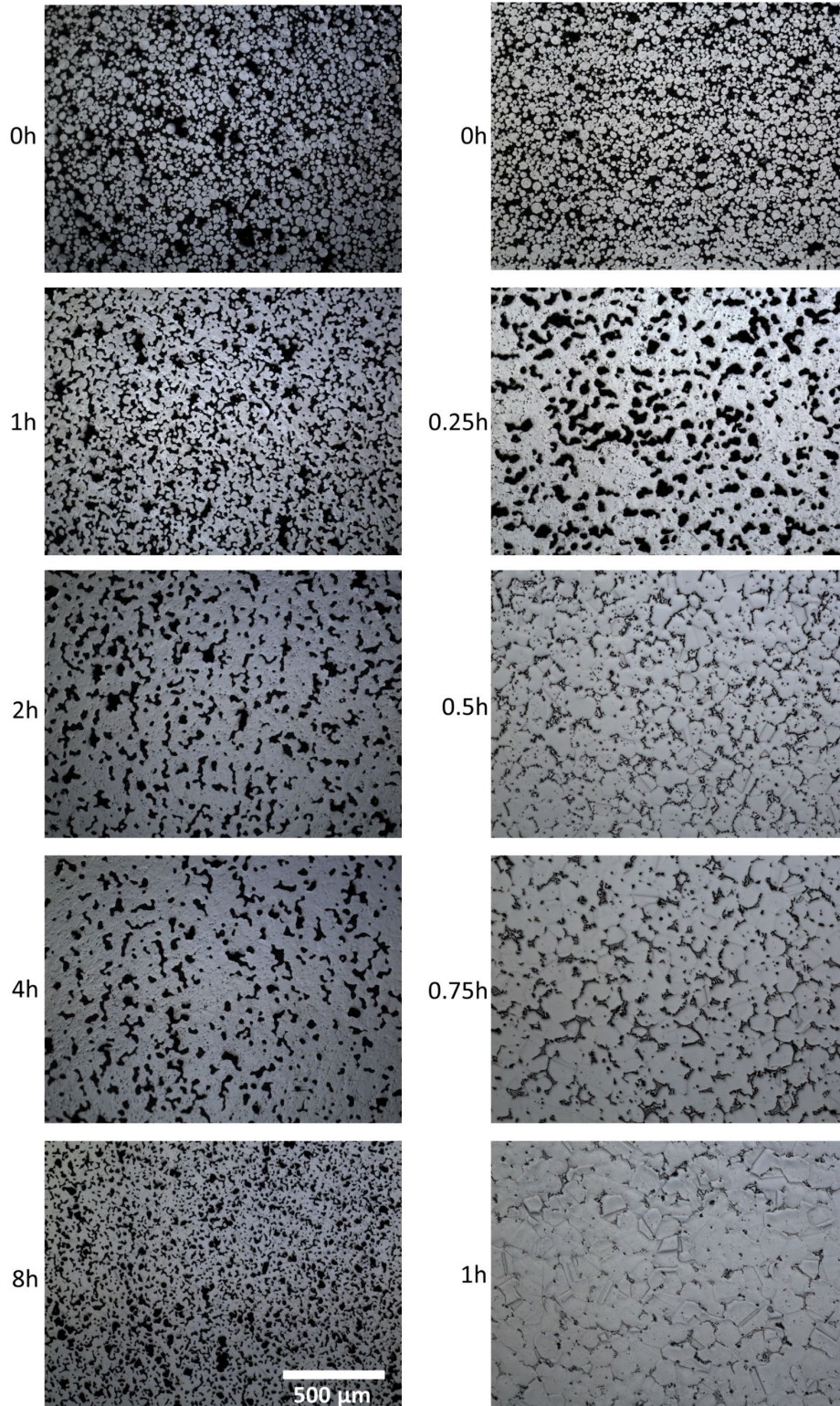


Figure 28. OM images (100X) for SS (left) and SLPS (right) sintered samples. The images are taken on the XOZ-plane therefore interlayer defects (vertical) and printing lines (horizontal) may be visible.

Solid area fraction (SAF) as another measure of density, has been calculated using ImageJ software based on Figure 29 images and is shown in Figure 30. In general, there is good agreement between SAF and Archimedes densities. Note that the dark areas in SLPS group were not likely to be residual porosity and appeared to be secondary phases introduced during liquid formation in SLPS. A detailed comparison between Archimedes density, OM and CT densities is explained in later section. For SS samples, printing lines remained visible in the form of elongated pore sections until 4 h, and at 8 h there may still be pore sections clustered vertically forming segmented printing lines. On the other hand, the elongated pore sections in SLPS samples were eliminated quickly after 0.25 h of sintering. This can be attributed to the liquid formation in SLPS that allowed rapid particle rearrangements[112].

For VRA samples, since the densities were close to 100% after the first step sintering, the OM images are omitted here. Figure 29 shows the SEM images of VRA group samples. Figure 30 shows the liquid area fraction of samples sintered under different time duration of SLPS and VRA. From Figure 30, the liquid began to form at 0 h of SLPS which correlates with the solidus temperature measured previously. As sintering time increased the amount of liquid phase rose and peaked at 1 h of SLPS. Then the second-step SS process of VRA helped decrease the liquid fraction. After 12 h of SS the liquid amount decreased to approximately 50% of the peak liquid content at SLPS 1 h. Also, the grain size of VRA samples seemed to increase considerably as the SS time increases. At 1+1 h of VRA the mean grain size is $\sim 150 \mu\text{m}$ and it had grown to $\sim 400 \mu\text{m}$ after 1+12 h VRA. This may due to the fact that the SS temperature was close to the solidus, hence the driving force for grain growth is high. Despite the drawbacks in strength and ductility, the diminished grain boundary may have benefits in creep resistance for the VRA samples.

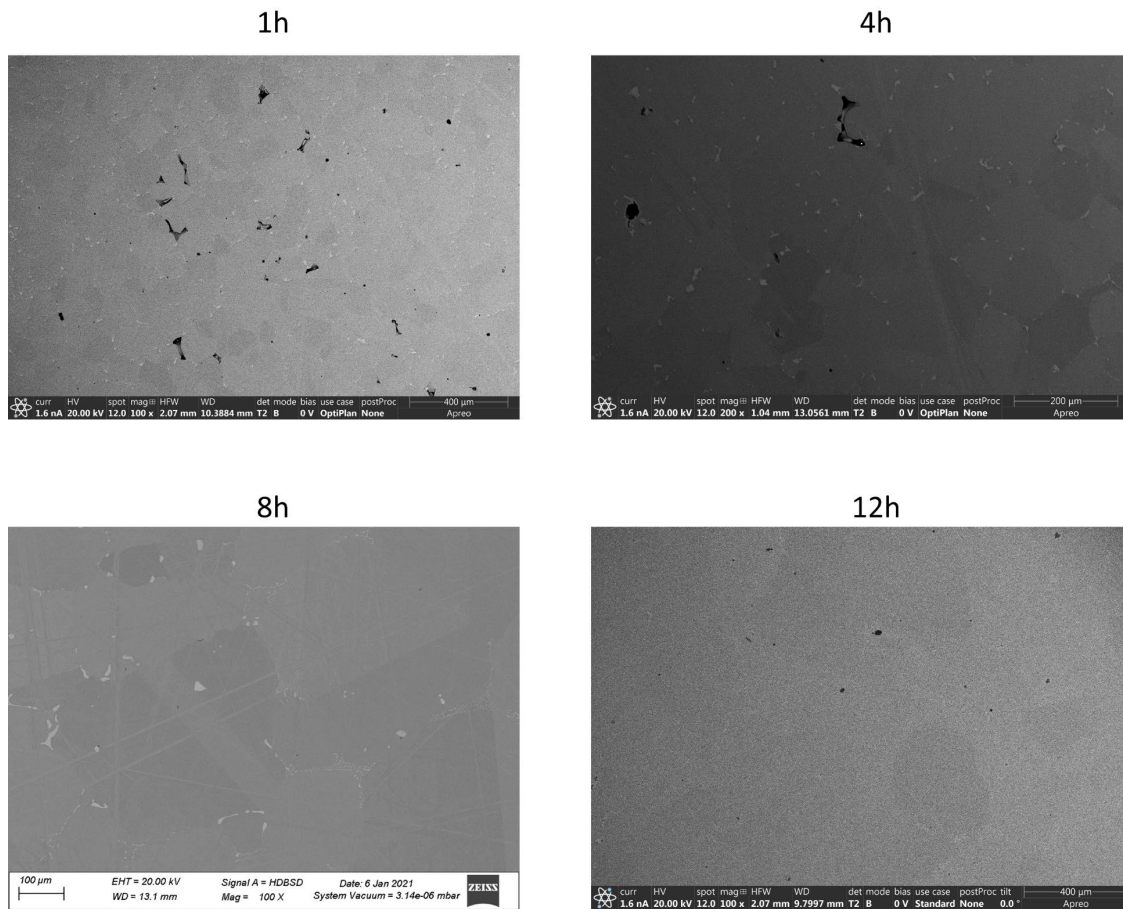


Figure 29. SEM images of VRA samples under different SS-time.

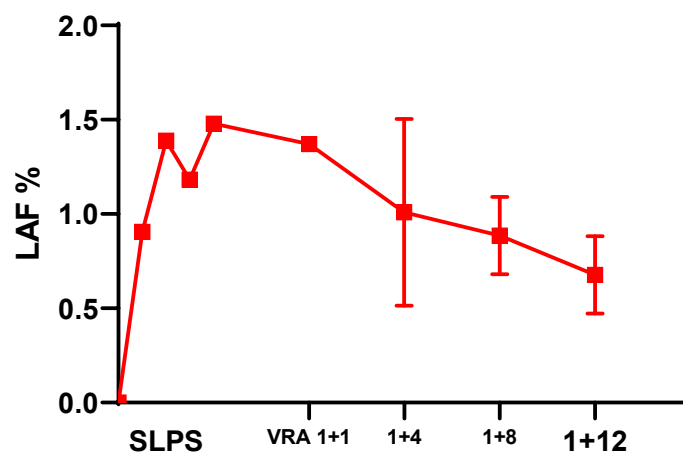


Figure 30. Liquid Area Fraction (LAF) of SLPS and VRA – sintered samples. The LAF data was calculated from SEM images using ImageJ[118].

The morphology of the secondary phases observed for SLPS and VRA samples, shown as bright contrast in backscattered electron SEM images (BSE), is similar to the δ phase observed in traditional heat treated 625 alloys. As a nickel-based superalloy, 625 alloy is expected to have a wide single phase region under equilibrium across different wt.% of alloying elements. Also it is quite difficult to determine a multicomponent phase diagram for an alloy like 625. However there are evidences suggest that for a Ni-Cr-Mo-Fe-Nb-C-Si system, “qualitatively, the elements behaved similarly in the alloys examined as in binary systems with nickel”[119], especially for Nb addition. Therefore, one may use an isopleth of a binary phase diagram to estimate phase formation and melting behavior under sub- and supersolidus sintering in this work.

Figure 31 shows an isopleth of the Ni-Nb system with other elements fixed at the wt. % of a wrought 625 alloy[116]. As anticipated, the FCC (γ) phase is very wide around the isothermal sintering temperatures used in this study. Since Nb has a high diffusion coefficient in this system, it can be expected that Nb-rich grain boundaries will form under heating, thus lowering the solidus temperature, and hence the liquid phase will preferentially form around grain boundaries. From the phase diagram, it is not obvious that δ phase will form under isothermal sintering temperatures. XRD patterns studied by Mostafaei et al.[32] show peaks of δ phase for the BJ3DP 625 samples under supersolidus sintering, but they are highly overlapped with γ/γ' peaks. In general, δ phase is rarely seen for unaged 625 alloy. The δ phase observed in this work was possibly formed during cooling from supersolidus temperature, since little contrasts, both under SEM(BSE) or EDS area scans, were observed for SS samples. In this case δ phase may have helped pinning grain boundaries and slowed down the grain growth. This also explains the grain size differences between VRA 1+1 h and 1 + 12 h as the secondary phases being eliminate during SS sintering.

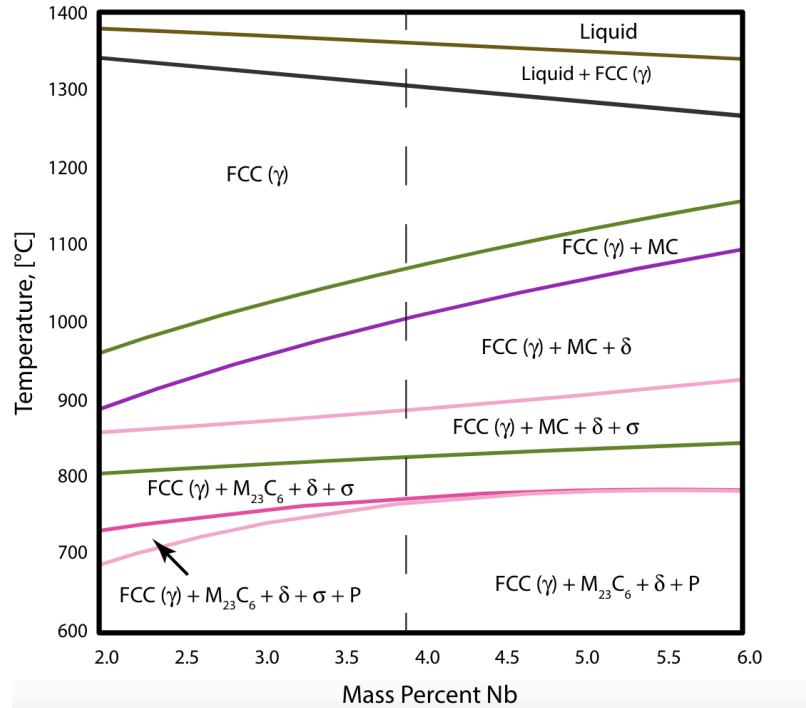


Figure 31 A Ni-Nb isopleth showing phase formations of the 625 alloy. Dashed line shows a Nb composition of 3.7 wt.%. Image adopted from [116]

6.1.3 CT Results

Due to the size constraints, the samples used in CT scanning required significantly smaller volume comparing to sintered samples. Therefore, cylindrical samples with a diameter of around 1.2 mm were cut from the full sample using a Mitsubishi MV 2400-S wire EDM machine (Mitsubishi Heavy Industries, Ltd., Japan). The samples were then scanned using the Bruker Skyscan 1272 with a resolution of 1.2 μm per pixel edge length. Then the raw images were reconstructed using NRecon software and analyzed with CTAn.

Figure 32 shows the reconstructed images for SS and SLPS sintered samples. It is worth pointing out that the image quality of μCT depends highly on density of the scanned sample. It was observed that when the sample density reached 95% or more, the X-ray penetration became

so difficult that the quality of acquired images provides no valuable data. Therefore the CT results for SLPS 0.75 h and 1 h were excluded in this work. Again, reconstructed CT images showed good agreement with Archimedes measurement as well as microscopy data. The comparison between CT results and other characterization methods is also included in Discussion session 6.1.5. One may intuitively see from Figure 32 that printing lines are visible for certain sintering conditions. It appears that printing lines were visible for SS samples until 4 h of sintering, which agrees well with OM results. For SLPS samples, printing lines were visible until after 0.25 h sintering. No obvious printing lines can be seen after 8 h SS or 0.5 h SLPS sintering. On the other hand, it was less straightforward to see interlayer defects from merely the anatomical views. Hence, to quantitatively investigate the evolution of interlayer defects, solid area fraction analyses was carried out on reconstructed 2D sections in a layer-by-layer manner for each sample. Each reconstructed 2D section will generate one SAF value via CT thresholding algorithms. Next, the SAF values were plotted against its respective layer number. Since the layer number corresponds to the relative height of the sample, this plot is equivalent to the SAF variation along Z-direction. The Z-stack SAF plots are shown in Figure 33. For each sample, there are 1200 2D sections involved in the region of interest (ROI) for analysis which corresponds to 1.44 mm in height.

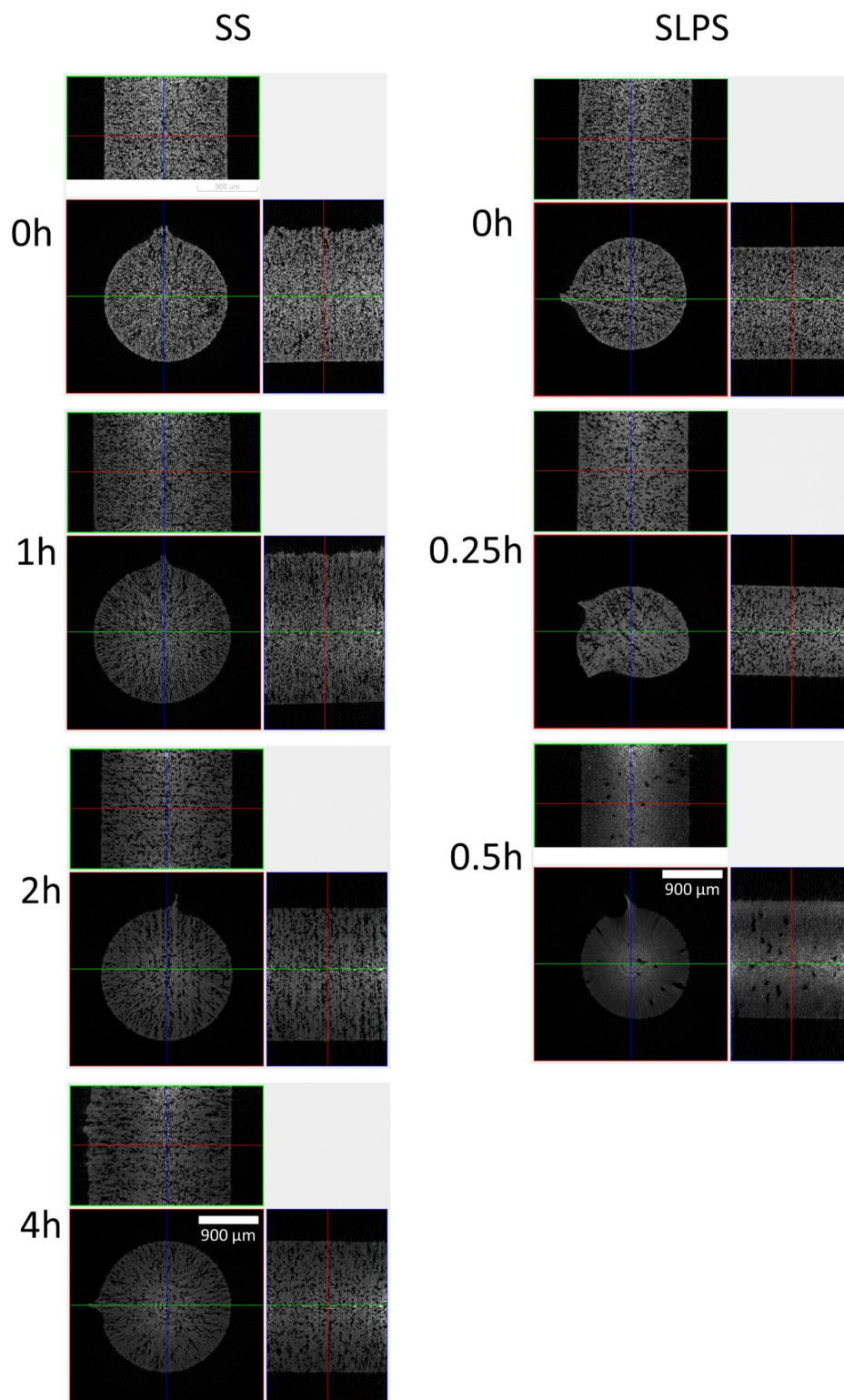


Figure 32. Reconstructed μ CT images for SS (left) and SLPS (right) samples, anatomical view. SLPS 0.75 h and 1 h samples were excluded due to their high density and difficulty in X-ray penetration.

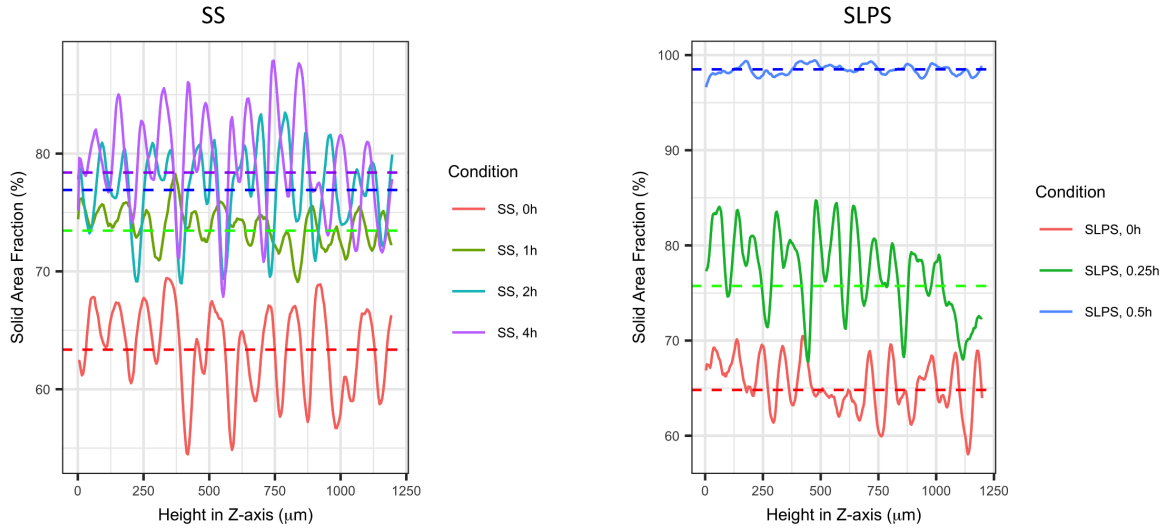


Figure 33. SAF variation along Z-direction for SS and SLPS samples.

In Figure 33, solid lines indicate SAF values, and dashed lines indicate the mean SAF of all slices. For SS samples, the mean SAF increased from $\sim 64\%$ to $\sim 79\%$ as sintering time extends from 0 h to 4 h. At 0 h, initial densification occurs so that the mean SAF improved to above 60%, with pronounced “wave” characteristics in SAF variation, whose “amplitude” ranging from below 55% to nearly 70%. Moreover, the “half-wavelength” of such SAF values, as can be seen in the figure, is approximately 100 μm , which is the set-up value of the layer thickness when printing. Therefore it is quite reasonable to infer that this “wave” behavior originated from the layer spreading during the printing process. When the powder is spread using hopper vibration, it is anticipated that the powder inside the middle of a layer tend to pack more efficiently leading to high SAF. Interaction of binder droplets, roller, and partial-curing process in a printing cycle with the powder particles near the boundaries of adjacent layers are thought to result in less efficient packing, and larger packing defects at the layer interfaces that lower SAF.

Within the first hour of SS sintering the samples densified by a significant amount to nearly 75%. The amplitude at 1 h SS seems to also decrease, ranging from 69-78%. At this stage, it is

thought that the initial densification was rapid and helped to reduce the large defects in the interlayer region. It can be imagined that the region with lower SAF has a higher driving force of densification, therefore the overall system tends to lower the range of densities between the high- and low-density regions. However, beyond 1 hour of SS sintering such equilibration was not observed. At 2 h SS the mean SAF continues to increase to about 77-78% but the amplitude increases again to ~ 15% (69%-84% range). This indicates that, although the system continues to densify, the remaining driving force at low-SAF region is no longer high enough to reduce the amplitude. Furthermore, at 4 h SS the mean density almost plateaued at 78-79 mean SAF but the amplitude as 4 h is as high as ~ 20%. This shows that the densification rate between high-SAF region and low-SAF region has flipped and the pore shrinkage and elimination at high-SAF region is now more efficient. This results in some highly densified bands along the z-direction, as shown in the figure, with density as high as 88% and some very porous region with an SAF of 68%. The 88% SAF means that the denser regions in the sample microstructure were approaching final stage sintering, where pores became isolated and began to be eliminated. Once the pore closes off and become eliminated, the average diffusion distance between pores would increase rapidly, resulting in a sluggish densification rate. Therefore, it can be thought that overall densification stalled after 4 h of sintering and resulted in a porous final microstructure with little driving force for further densification and relatively large diffusion distances.

For SLPS samples, at 0 h, the mean SAF is 65%, close to that of the SS 0h sample. However, the wave amplitude is 59%-70% which is smaller than the amplitude for SS 0h SAF. This may be due to the liquid formation during the later stages of heating, and again according to [112], the particle rearrangement with the help of liquid can collapse large defects in the low-SAF region, making the microstructure more uniform. The mean SAF improved to ~76% at 0.25 h of

SLPS and the amplitude also increased to around 17%, but unlike SS samples, SLPS samples can continue to density after 0.25 h. At SLPS 0.5 h the sample is already significantly densified to above 96% with very small variation of SAF along the height. This is an indication of a much more uniform densification that goes to full density. In a nutshell, from Figure 33, the SAF plots shows that 1) the origin of such wave behavior may come from layered spreading and printing; and 2) SLPS sintering was able to fully eliminate such wave behavior and reach full density, whereas SS sintering fails to repair these large interlayer defects and causes the densification to stall.

Structure thickness and separation is one of the unique features provided by the CTAn software. In 3D analysis, the structure thickness and separation measurement use a sphere fitting algorithm. For an enclosed object, first a skeletonization process is applied to the object to sketch a medial axis along the long edge of the object. Then a sphere is moved along this axis to maximize its diameter while making sure that the sphere is fully enclosed in the object. The maximum diameter corresponds to the structure thickness of this object. By the same token, structure separation is also determined by sphere fitting, only in the enclosed cavities (black voxels). This method has been proven to minimize the bias caused by the selection of orientation[120]. A sketch showing the sphere fitting process is shown in Figure 34.

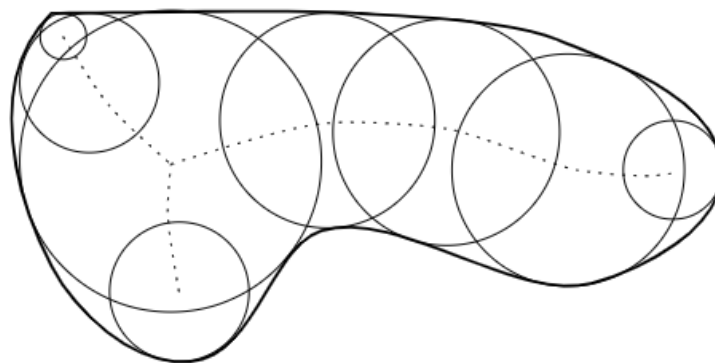


Figure 34. Sphere fitting of an enclosed object. Dashed lines indicate skeletonized axes. Image adopted from

[120].

In sintering studies, the concept of pore size, grain size and pore separation are commonly used to investigate the sintering kinetics. Here one may extend these stereological parameters into 3D by using the concept of structure thickness (STTH) and structure separation (STSP). An illustration of how the structure thickness/separation can relate to pore separation and size is shown in Figure 35. Here, a circle (a sphere in 3D) is fitted into the solid phase surrounded by pores. The diameter of the circle corresponds to structure thickness, which can also be approximated as pore separation. In heterogeneous microstructures, this separation can generally be regarded as the twice of the effective diffusion distance, although the diffusion path is along the grain boundaries in reality. On the other hand, if the pore shape is close to spherical, then the circle fitting of the pore phase, or the structure separation, essentially equals the pore size. In case that the pores are non-spherical and are elongated throughout the 3D volume, the structure thickness will roughly equal the width of the pore channel. The distinct advantage of using STTH and STSP is that this measurement method is not a field measurement but a feature measurement. In traditional 2D stereology, all the pores in the region of interest (ROI) will contribute to the mean free path of pore separation, and the result is one single value. Here one may obtain a distribution of pore separations in 3D and theoretically can fit the distribution to its densification behavior, constructing a 3D microstructural pathway for sintering.

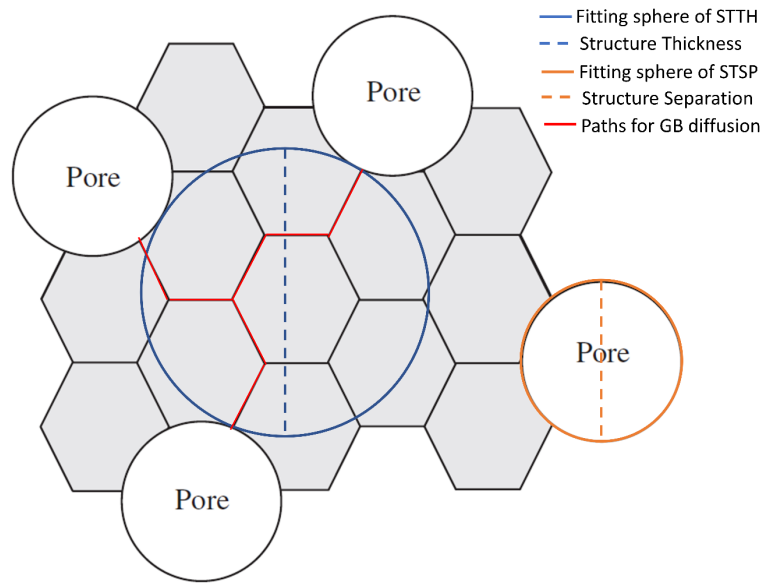


Figure 35 An illustration of applying structure thickness/separation analysis on a porous structure. Figure edited based on [55]

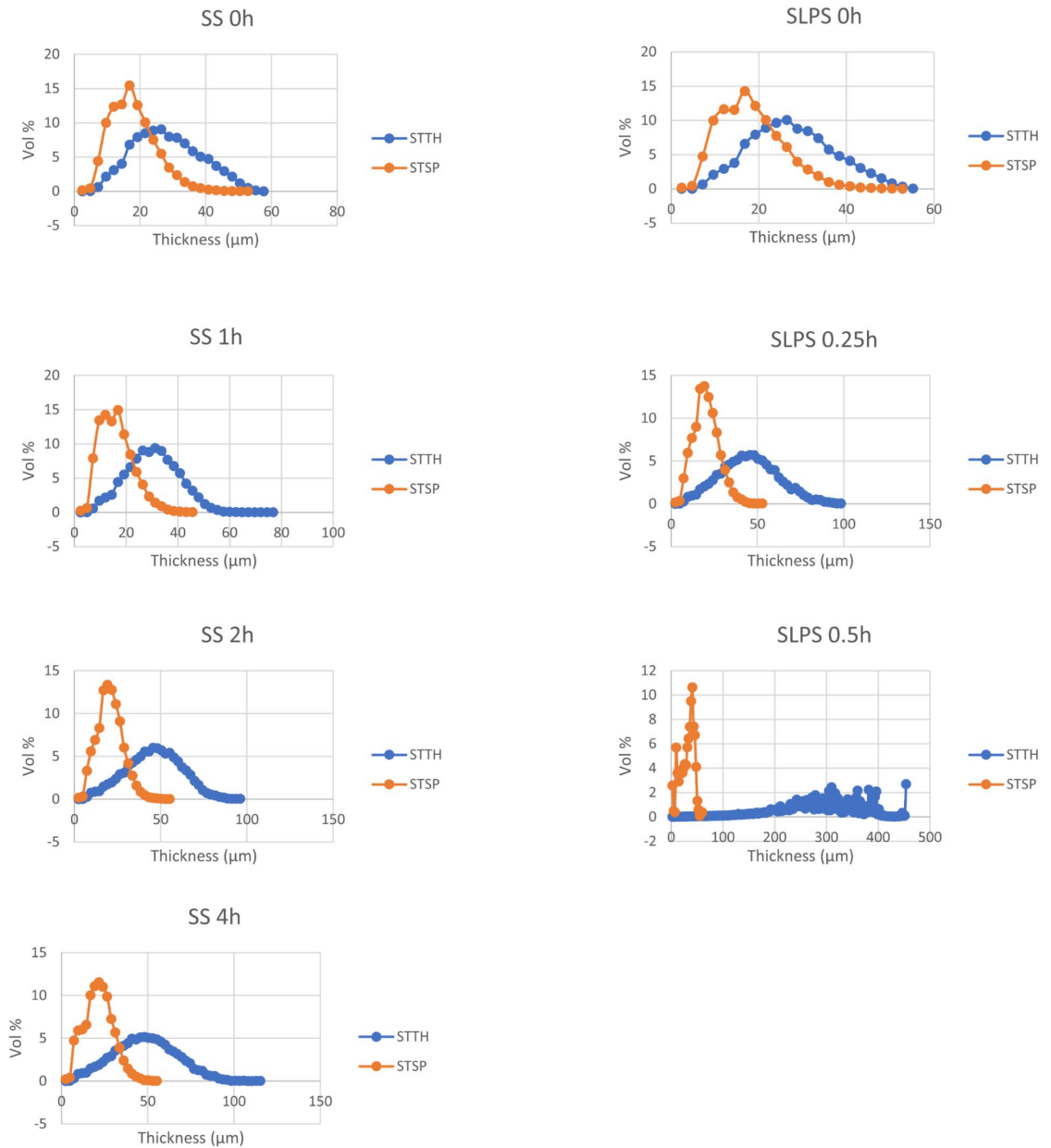


Figure 36. Structure thickness and separation distributions.

Figure 36 shows the structure thickness and separations for sintered regular samples. Note that at 0 h, the thickness and separation distributions are very alike between SS and SLPS samples. The mode of STTH (pore separation in 3D) is around 30 μm , which is very close to the mean particle size if averaged by volume instead of number. The mode of STSP (pore channel diameter in 3D) was approximately 18 μm , indicating most of the pores had a “thickness” no more than the

size of a 625 alloy particle. For SS samples, the STTH gradually increased from 0 h to 4 h while STSP stayed almost at the same level. On the other hand, STTH changed rapidly from 0.25 h to 0.5 h. By 0.5 h the mode of STTH was already above 300 μm , indicating that there were thick “bands” of solid that are pore-free. There was even a significant volume of solid structures with a thickness of about 450 μm .

6.1.4 Statistical and Orientation Analysis

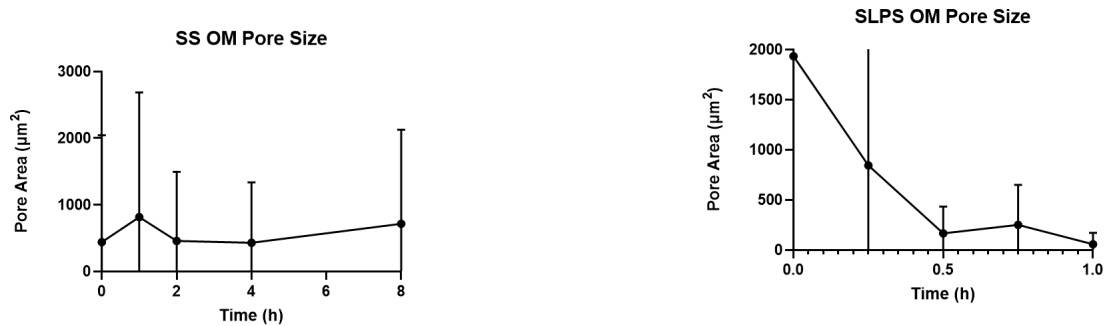


Figure 37. Mean and standard deviation of pore areas observed by OM.

Figure 37 shows the pore area average and distribution of SS and SLPS samples observed under optical microscopy. The pores were segmented by thresholding of grayscale OM images and calculated their area using ImageJ software[121]. It is obvious that the mean pore area of SS samples remained in a range of 500 – 1000 μm^2 , and the standard deviation was very large, up to more than 5000 μm^2 for SS 1 h samples. This implies that although the overall microstructure was densifying, the large pores were not really shrinking, and thus the standard deviation remained high even after 4 hours of sintering. On the other hand, for SLPS samples, the mean and standard deviation were both large at 0 h, but quickly diminished as the samples sinter. At 0.5 h the average

pore size was already lower than $200 \mu\text{m}^2$. This demonstrates again that SLPS was capable of eliminating both large and small pores and fully densifying the material.

Similarly, after segmentation of the scanned CT images, the pore size analysis can also be carried out using individual 3D analysis (i3D) of the objects. To achieve this goal, the reconstructed images must be segmented inversely such that the pore phase are shown in white voxels. The pore volume was then counted by the CTAn software and assembled into distributions and finally visualized using a distribution density plot, as shown in Figure 38. The distribution density plot was generated using ggplot 2 package in R[122]. The overall algorithm is that the program first creates histograms with adaptive binning based on the data collected from CTAn output, then applies a gaussian filter to generate a smooth distribution density. This can be thought as the probability density, i.e., how many pores one will likely find at a given pore volume.

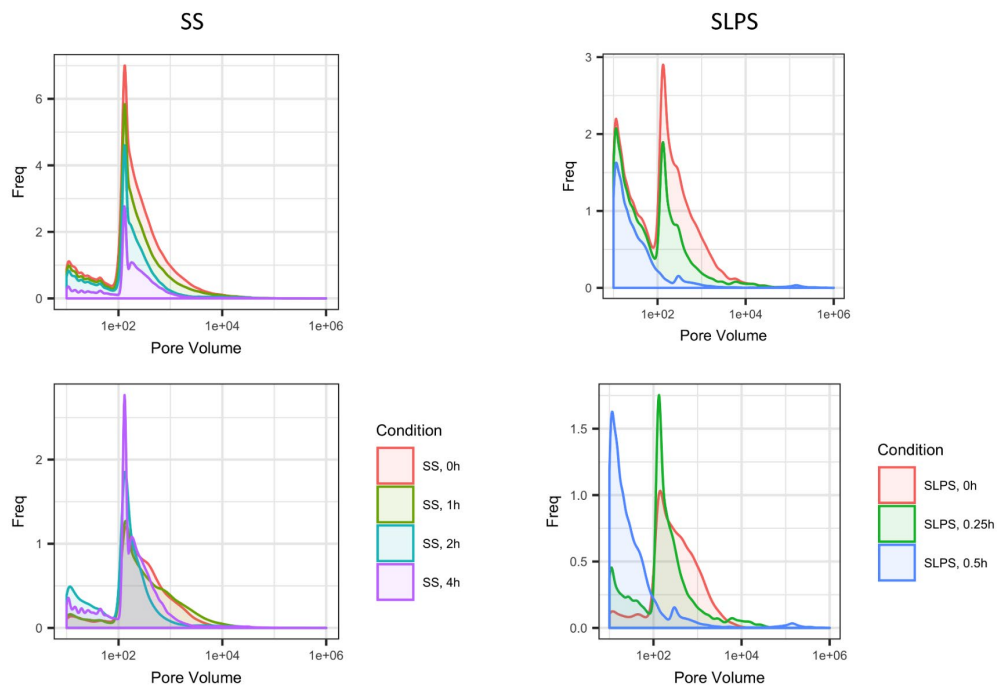


Figure 38. Distribution frequency plot for pore volumes measured in 3D, unit in μm^3 . Top figures show the distributions counted by absolute number; bottom figures show relative frequencies.

From Figure 38, the pore size evolution behaved very similar to the 2D pore area distribution in the preliminary work (see Figure 22). The mode for SS samples stayed constant as sintering time increased, although the absolute number of pores decreased. Again, this demonstrates that after 2 h, the closure of small pore sections dominated the microstructure evolution but contributed little to densification. On the contrary, the mode for SLPS sintered samples had a significant shift towards the finer end. After 0.5 h there was very few pores with a size larger than $100 \mu\text{m}^3$. The abnormal high peak at the very fine end (left) is probably due to the speckle noises in the thresholded image. Since this distribution is plotted on a log scale, most of these “pores” are of a volume of one voxel, which is highly likely an artifact. In general, the comparison with the 2D pore size distributions demonstrated again that the 3D analysis results are reliable and quantitatively comparable to the results obtained from traditional 2D imaging.

It is possible to convert the pore volume or area to one-dimensional pore size and compare the results between 2D and 3D analyses. For instance, one may use equivalent circle diameter in area (ECDa) for 2D pore sections, and equivalent sphere diameter in volume (ESDv) for pores in 3D. However, it was not particularly helpful doing such conversions in this work, since the necessary geometric assumptions behind is that the pores are close to circular in 2D and spherical in 3D. This is in general not true for partially sintered BJ3DP materials. The defects were naturally highly heterogeneous due to the printing process, and the sintered pore channels remain elongated and were very connective throughout most sintering conditions. In a 2D section, one may only able to capture one cross section of such pore network, hence it makes much less sense to make the ESDv and ECDa conversion, let alone the comparison. In fact, pore area and volume are regarded a better representation of pore attributes in this work. Nevertheless, these measurements are still internally consistent and comparable.

As introduced previously, there are three types of defects that exist in the microstructure of binder-jetted materials, two of them are introduced by printing and may therefore be orientation dependent. To investigate separately the microstructural evolution of each defect type, an in-house designed code was developed to automate the line intercept method in quantitative stereology and to compute the line intercept density along x- and y-direction in each reconstructed CT slice. The essential workflow of such line intercept measurement is conducted as follows: first, a reconstructed CT slice is segmented and cropped into a round-shape ROI. The processed image is then rotated such that the printing lines, if noticeable, align with the vertical direction of the image. A series of horizontal and vertical lines are then applied to the image and will intercept pore boundaries. The code then counts the number of intercepts along horizontal and vertical directions respectively and then normalize the numbers by the total length of the test lines. The outcome of such algorithm is the number of pore intercepts per unit length along a certain orientation. An example of processed image in such work is shown below in Figure 39.

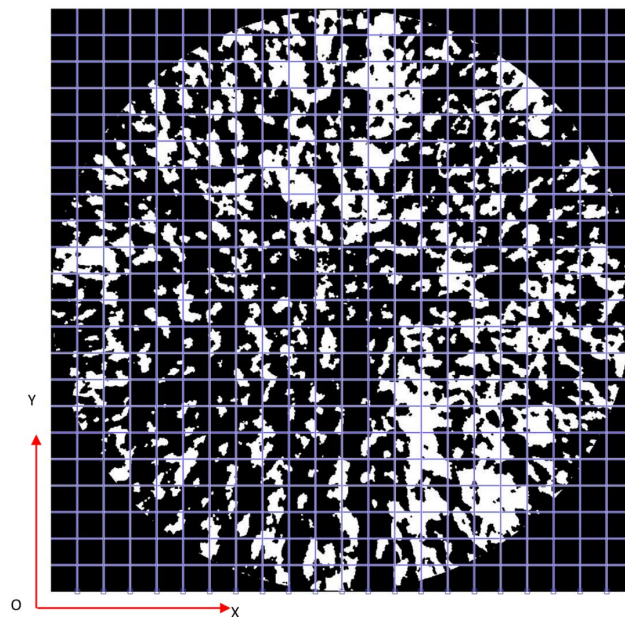


Figure 39. An example of applying intercept measurements on a reconstructed CT slice. The image has been segmented such that white objects reflect pores.

One CT-scanned green body and each sintered sample has been examined by selecting representative volumes and analyzing every slice in such a volume. For each sample, the representative volume has the number of consecutive 2D section images for a volume equal to a “half-wavelength”, that is, the sections between a local minimum in density corresponding to a layer interface and an adjacent maximum corresponding to the relatively dense interior of the layer in the SAF plot for that sample. This collection of sections is called a “mini-stack”. The number of intersects along x- and y-direction as well as the mean are again plotted against the number of images in the mini z-stack. An example of the “half-wavelength” analysis using SS 0 h sample is shown in Figure 40. First, a “mini-stack” of continuous image slices (boxed with dashed lines in (a)) were chosen that has an SAF variation from a local minimum to a local maximum. The “minimum” slice represents the interlayer region, and the “maximum” slice represents the dense region inside a printed layer. Their SAF values are plotted in (b). Then the line intercept analysis was performed on this “mini-stack”, one 2D slice at a time. Finally, the line intercept density (number of intercepts per unit length of test line) along vertical direction, horizontal direction or their average, is plotted against Z-height, as shown in (c). Results for seven representative samples are shown in Figure 41, including one green body, SS sintered samples 0, 1, 2, and 4 h. Since it has been demonstrated that SLPS can repair all printing defects and fully densify the system, the intercept analysis for SLPS samples were omitted.

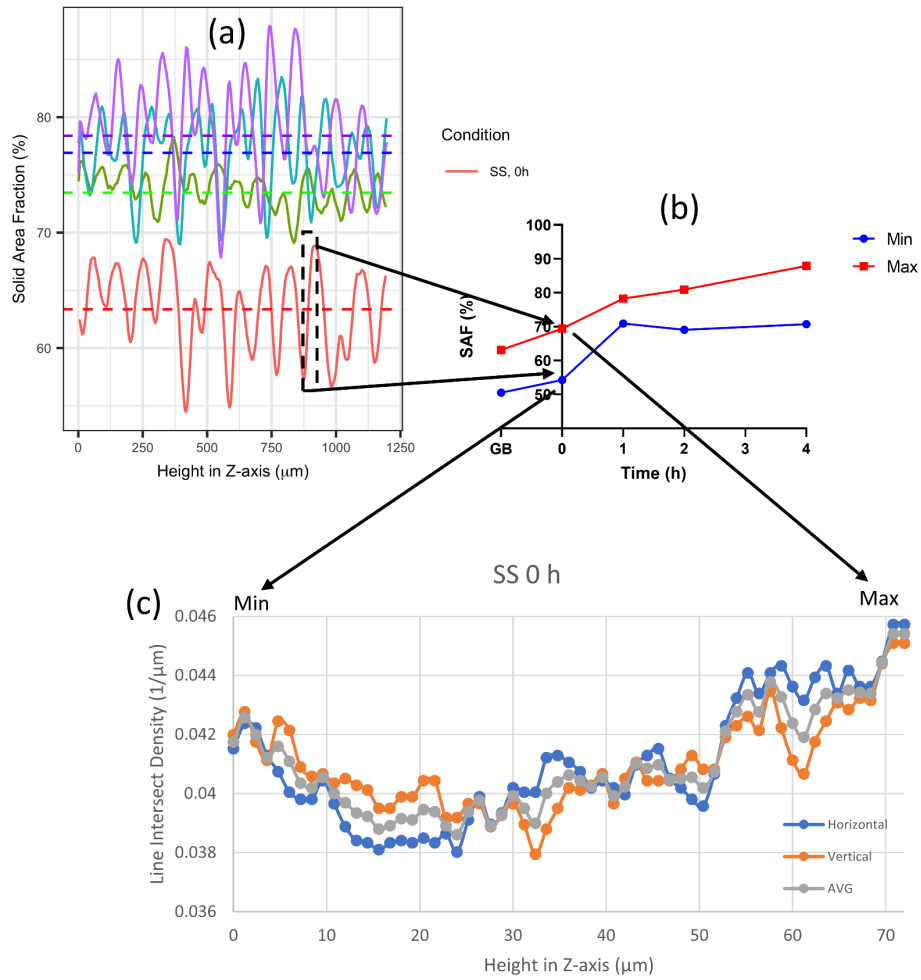
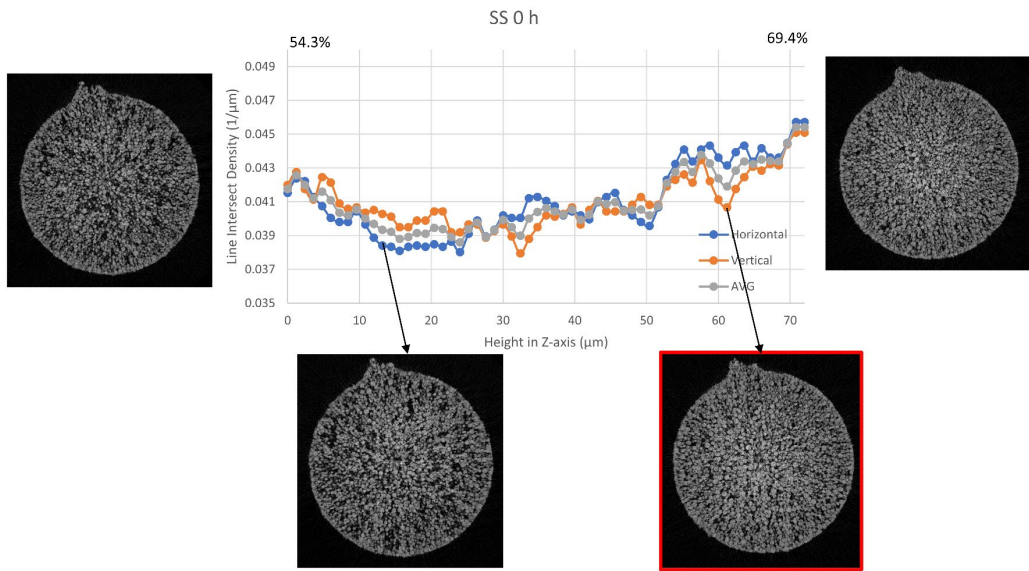
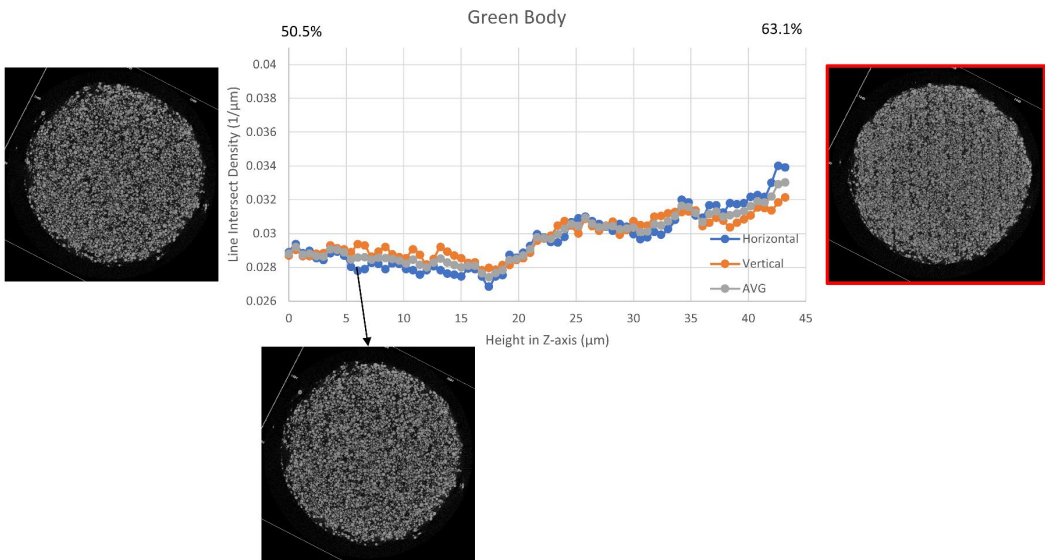


Figure 40 The line intercept analysis using a stack of images in the SS 0 h sample. A “half-wavelength” of the images were chosen in the analysis.



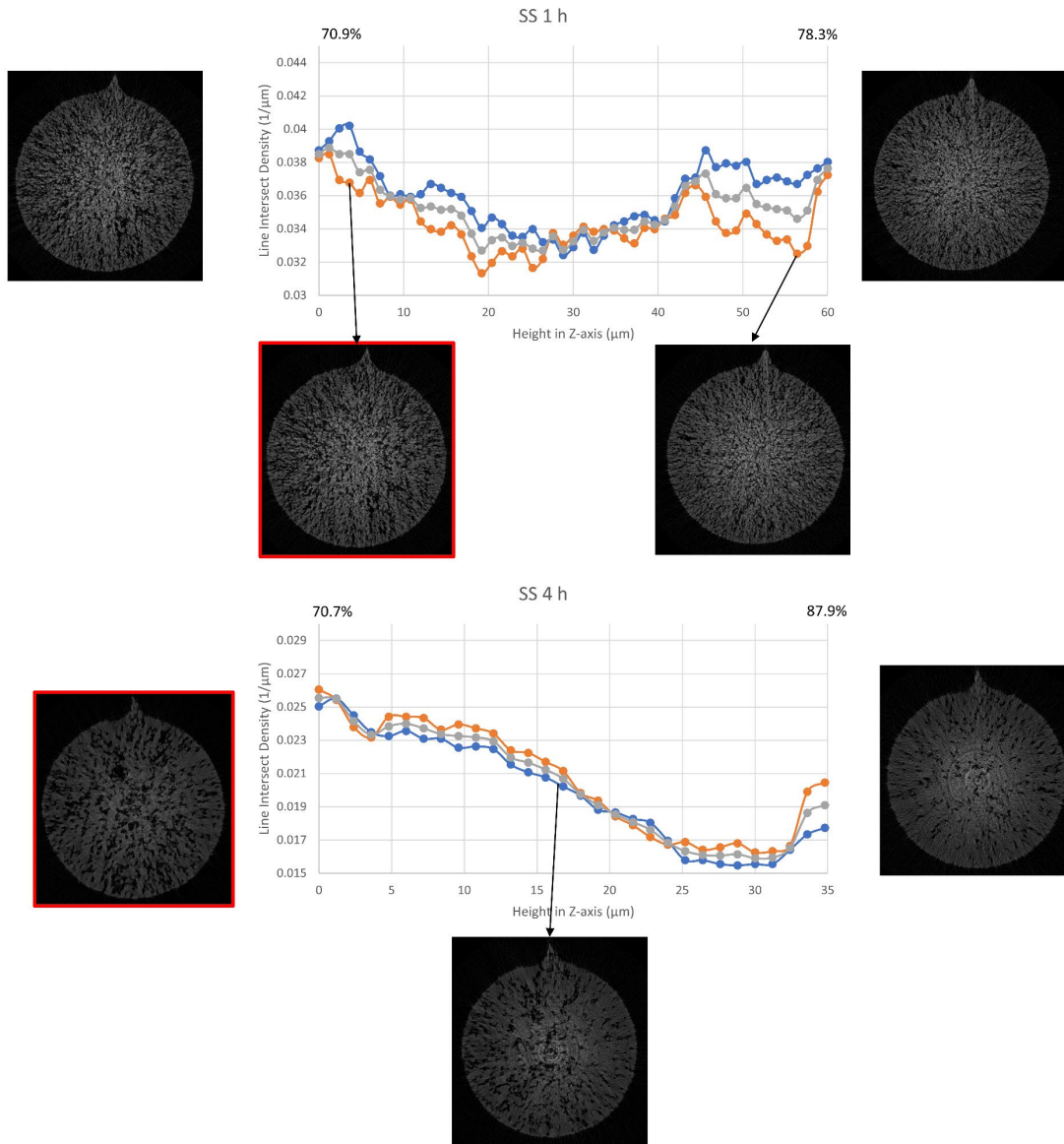


Figure 41. Line intercept test results. Blue markers represent horizontal intercepts, orange markers vertical intercepts, and grey the average. X axis shows the relative z-height in the “mini-stack” (minima-maxima from left to right, with respective 2D SAF values).

As shown in Figure 32, vertical printing lines can be readily seen in the reconstructed image. For the green body, in the line intercept (LI) plot, the vertical line number is generally higher than horizontal in low-density regions (0-22 μm), and lower than the number of horizontal

intercepts in high-density regions (22-43 μm). This suggests that there are more pores along y-direction in low-density region, forming the visible printing lines. In the high-density region, the relationship between horizontal and vertical LI number is flipped. It is interesting that the average LI in the high-density region is higher than in low-density region. At the high-density region, namely inside a printing layer, the pores are mainly random packing defects and particle interstices. These pores are smaller in size and do not have orientation preference, therefore there is less chance that these are part of one large pore network in a 2D slice. On the other hand, the interlayer defects are likely assemblies of multiple pores formed by printing. Hence, although the density is higher inside the printing layer, the pore area density N_A (number of pores per unit area) may be higher than interlayer regions. This can be verified from the reconstructed image at the local maximum/minimum of the green body. It can be seen that the number of particles was fewer and less well packed in the local minimum. Interestingly, in the minimum slice, vertical printing lines are not as visually obvious as in the maximum slice inside the print layer. Again, this is because the minimum slice is generally more porous, and the pores around the printing lines are highly connective, making the lines not so clear by visual inspection.

At SS 0 h, the absolute number of LIs is $\sim 50\%$ higher compared to the green state. This is an indication of pore closure in 2D, forming more closed pore sections and increasing N_A . Moreover, the difference between horizontal and vertical LI numbers become more pronounced. Although it lacks a clear trend in the relative difference between the LI values corresponding to the two orientations or corresponding to the minimum-maximum transition in SAF, in general the relative relationship between horizontal and vertical lines are similar to the green state, where the horizontal LI number is higher in high density region. Here, printing lines were mostly visible at

the slices closer to the local maximum ($\sim 56 \mu\text{m}$), just like the green body, but at the very maximum, the printing lines were starting to degrade by pore section elimination as the SAF went to $\sim 70\%$. It is likely that SS sintering was effectively repairing the printing lines even at early-intermediate stage sintering. At SS 1 h the absolute value of LI began to decrease, indicating very fine pore sections being eliminated in 2D. Note that this does not suggest pore elimination in 3D. At this point, printing lines were no longer visible in high density regions, but still visible in low density regions. The relative relationship between horizontal and vertical lines flipped, in that the horizontal LI exceeded vertical LI. This suggests that the pore sections began to merge in 2D forming large irregular defects in low density regions. A few large pore sections can be readily seen from the image. This formation of larger elongated defects can be attribute to differential sintering across the printing layer interfaces. As a result, the morphology of printing line defects changed from an array of fine pore sections along the line towards a few long pore channels. Finally, at SS 4 h the LI average drops back to $0.02/\mu\text{m}$. At this point, the difference between horizontal and vertical LI numbers were small in most slices, indicating at SS 4 h there were no more pore orientation preference in the XOY-plane in the majority of the “mini-stack”. In most of the slices, there are large remnant pore sections that seem to be randomly oriented, but large linear pattern was observable in the local minimum slice. However, in addition to linear defects, it seems that the solid phases are clustered into “bands” which look linear in the 2D section.

By comparing reconstructed slices from green state to SS 4 h, it can be found that the slice which showed the most visible printing lines shifted from the local maxima to the local minima, when sintering continues as shown in the boxed images in Figure 41. This strongly suggest that the differential sintering occurring between printed layers in Z-direction had a significant influence on the generation and elimination of printing lines. In the interior of the print layers, SS sintering

was able to repair the printing lines as early as 1 h into isothermal sintering. In a nutshell, this is a demonstration that SS sintering is capable of repairing printing line defects, but the interlayer defects and their associated differential sintering have kept the remnants of both interlayer pores and printing lines in the low density regions.

6.1.5 Comparison between 2D and 3D Results

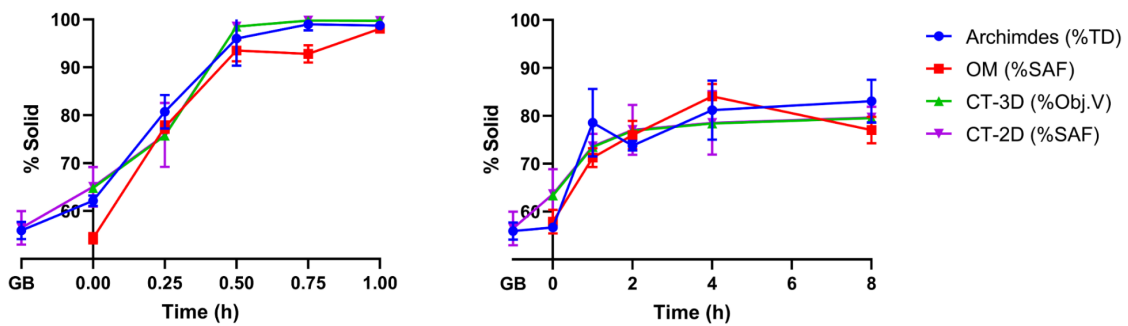


Figure 42. Comparison among Archimedes density, optical micrograph SAF and CT results. Left: SLPS samples; Right: SS Samples.

Figure 42 shows a comparison among different characterization techniques in terms of measured density. Generally, there is good agreement among all characterization methods. In fact, for SLPS samples, the error between CT results and Archimedes density are even smaller than the error between the latter and OM results. In microstructure characterization in sintering, Archimedes density is often regarded as “ground truth”. In this case, CT imaging has demonstrated its accuracy. For SLPS 0 h sample there was a significant gap between the OM SAF value and the Archimedes density. This can be attributed to the porous sectioned surface for microscopy. Since the material strength was low at 0 h, it is likely that extra materials was removed from the sectioned surface during grinding and polishing process. Moreover, the difference between the CT-2D

results and CT-3D results were minimal. This shows that the interpolation algorithm in the 3D analysis gave consistent results.

6.1.6 Three-dimensional Microstructure Pathway

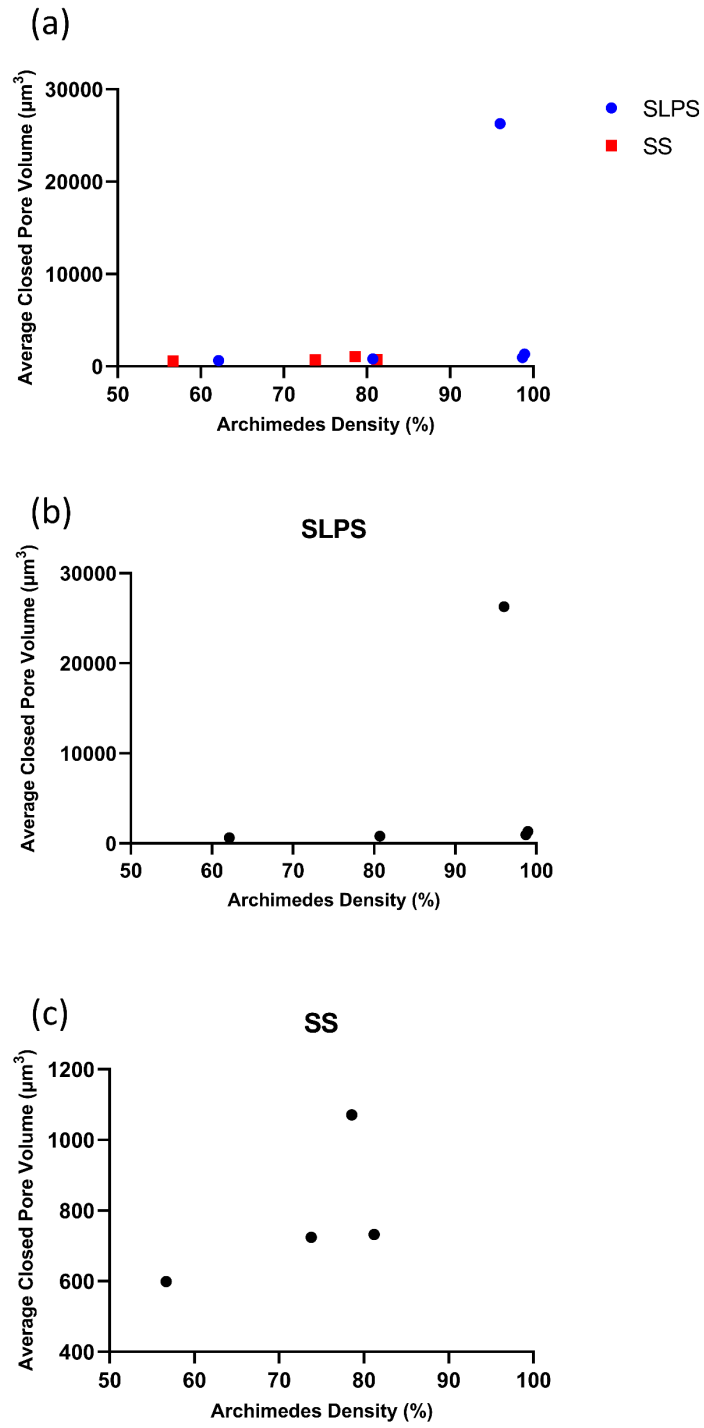


Figure 43. Average pore volume as a function of density. (a) all samples; (b) SLPS; (c) SS.

Figure 43 shows a 3D microstructural pathway, consisting of average pore volume as a function of density. For SS samples, there was a general trend of increasing average pore size as a function of sintering time. This is probably due to the elimination of fine pores in both intermediate and final stage sintering, while the larger pores are preserved. This correlates well with the 2D pore size data measure from OM (Figure 37) and 3D pore volume distribution plots (Figure 38). SLPS samples also showed an increase in pore size. Unlike the small pores in SS samples which were preferentially removed, the sudden increase in pore volume at a density of 98% is probably due to closure of all pores including the large pores. Once all pores are closed, a more homogeneous microstructure allowed further densification and eventually the elimination of all pore sections.

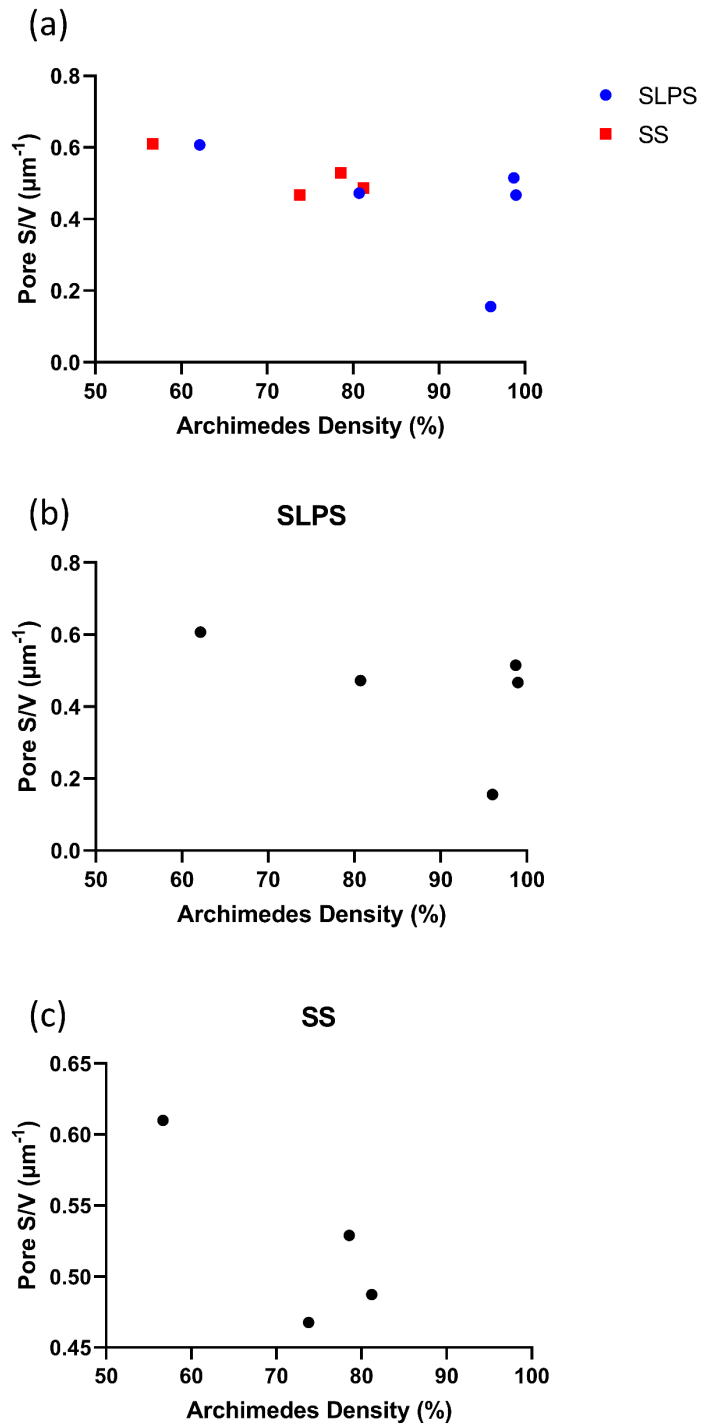


Figure 44. Pore surface to volume ratio as a function of density. (a) all samples; (b) SLPS; (c) SS.

Figure 44 shows another 3D microstructural pathway, this time for pore surface to volume ratio. Since the parameter S/V has a unit of length^{-1} , it was not surprising to see such value was

negatively correlated with the average pore volume. The S/V value decreased and then increased as the SLPS samples in the latter stage of sintering. Compared with studies performed on sintered alumina [66] which only showed a downslope line trajectory for the S/V value, this suggests such result that performed on 2D sections was biased. The pore may have seemed closed in a 2D section at low densities but was open in reality and was not taken into account in 3D measurements.

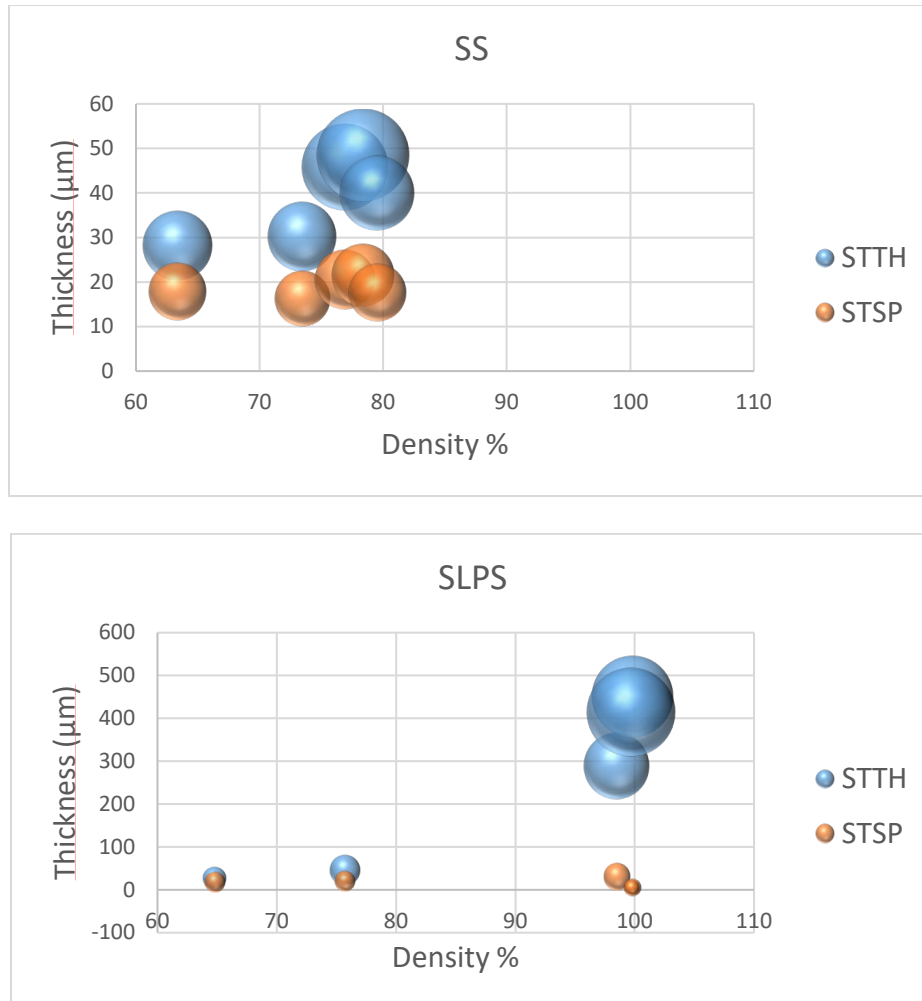


Figure 45. Structure thickness and separation evolution as a function of density. The coordinates of the balloons correspond to the mean of STTH/STSP, and the radii represents standard deviation.

Another unique 3D microstructural pathway that can only be generated with the help of μ CT is structure thickness/separation against density, shown in Figure 45. One important criterion that determines the material's sinterability is the separation between STTH and STSP, since if the

pores are being eliminated uniformly the STSP will eventually be diminished. If the sintering only eliminates fine pore sections, the STSP will remain constant, despite the increment of STTH. In SLPS samples, the separation between STSP and STTH occurred after the sample reached final stage sintering, whereas for SS samples the value of STSP hardly dropped.

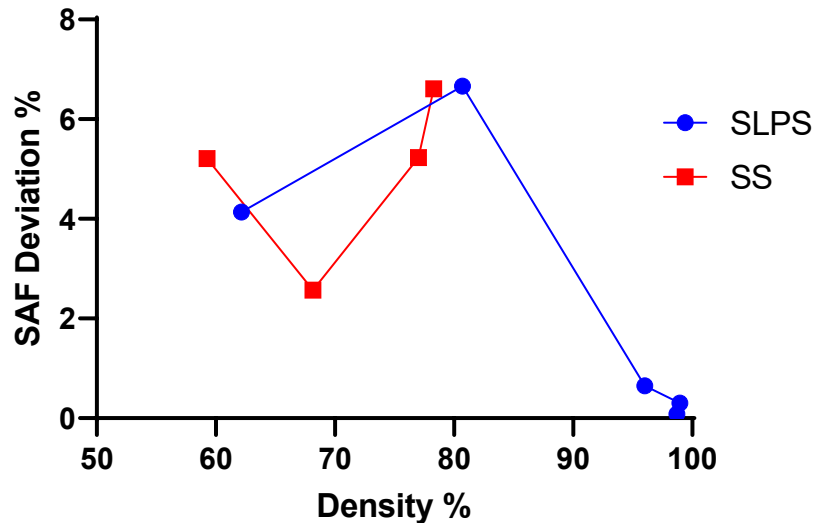


Figure 46. Standard deviation of SAF variation as a function of density.

To describe the extent of differential sintering, a new microstructural pathway has been plotted in Figure 46, in which the y-axis corresponds to the standard deviation of the Z-stack SAF variations for different samples (see Figure 33). It is assumed that the larger the deviation, the more severe differential sintering it represents. From Figure 46, the extent of differential sintering evolved quite differently between SS and SLPS samples. In SS samples, the SAF deviation first decreased when the density rose from 60% to nearly 70%. Then the SAF deviation began to increase until the end of sintering. Therefore, the heterogeneous microstructure was never repaired in SS. SLPS sintered sample also saw differential sintering at the density range of 60% to 80%, but with the help of viscous liquid, the microstructure was able to quickly homogenize, therefore the SAF deviation eventually disappeared as the sample went to full density. This behavior

somewhat correlates with Kanter's result[60], which suggests the maximum magnitude of sintering stress occurs at the beginning of final stage sintering of the material, although the “turnaround” point seemed to occur at a lower density.

6.2 “Skin” Samples

6.2.1 Experimental Design and Methods

The results for reconstructed CT images and Z-stack analysis on regular printed samples demonstrated the effect of the three defect types in the green state on sintering of binder-jetted 625 alloy, among which two types - interlayer spacing and printing lines – are directly caused by the nature of binder-jet printing process. Moreover, orientation analysis did detect orientation effects in the microstructure, probably associated with jetting of the binder. The two types of defects caused by printing may evolve differently under different sintering conditions. Therefore, it is intuitive to seek for a means of separating these two defects (those associated with spreading and those associated with jetting) and investigate their microstructure evolution separately.

To achieve this goal, a “skin” sample was designed using CAD software and imported to the X-1 Innovent printer for binder-jetting. Each of the “skin” samples consists of two parts: a “shell” which is normally binder-jetted, and a sealed “core” whose powder is deposited and spread flat using the hopper and roller of the X-1 Innovent machine, but the binder is not jetted into the layers, resulting in a stack of layers made of un-jetted powder in the interior of the jetted powder.

The CAD design of such skin samples consists of two-level cylindrical shapes, with larger diameter at the bases. The idea of such design is to ensure: 1) a cylindrical tip with diameter small

enough to be scanned under CT; 2) a base with larger cross-sectional area that can be observed using OM and SEM; and 3) an overall sample volume large enough to represent statistical significance when measuring density and porosity using Archimedes method. A final CAD design of skin samples is shown in Figure 47.

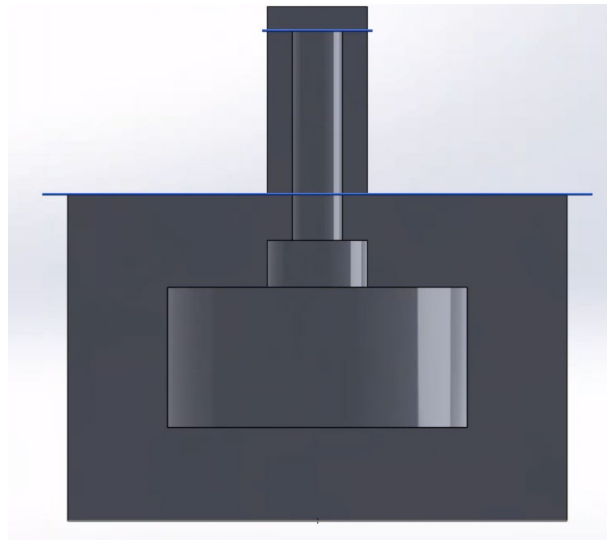


Figure 47. A cross-sectional view of CAD model for skin samples. Note that the hollow “core” shown in the CAD model will be filled with spread powders during actual printing.

Since the “shell” part of the skin samples are normally binder-jetted, it contains all three types of defects: interlayer spacings, printing lines and particle interstices/random packing defects. For the “core”, only interlayer spacings and particle interstices/random packing defects will exist since there is no jetted binder. Similar to regular samples, skin samples are sintered under sub- and supersolidus temperatures (1270 °C and 1285 °C, respectively) after binder curing. The sintering time are set to 0 h and 8 h for SS sintering, and 0, 0.25, 0.5 and 1h for SLPS sintering. Additionally, a VRA 1+1 h sample was sintered to verify that under VRA sintering, skin samples were able to fully density while avoiding heavy elemental segregations like that observed in the “regular” samples.

Due to the fragile nature of the un-jetted core, it was unrealistic to perform measurements or characterizations on the green skin samples. For sintered samples, Archimedes measurements are carried out for density and porosity data. μ CT scans were performed to obtain microstructural information from the interior. OM images were selectively taken on some samples, mainly to verify the fidelity of images acquired via CT scanning. Also, SEM images were taken on a sectioned surface of VRA sintered skin sample to reveal potential secondary phases in the microstructure.

6.2.2 Density

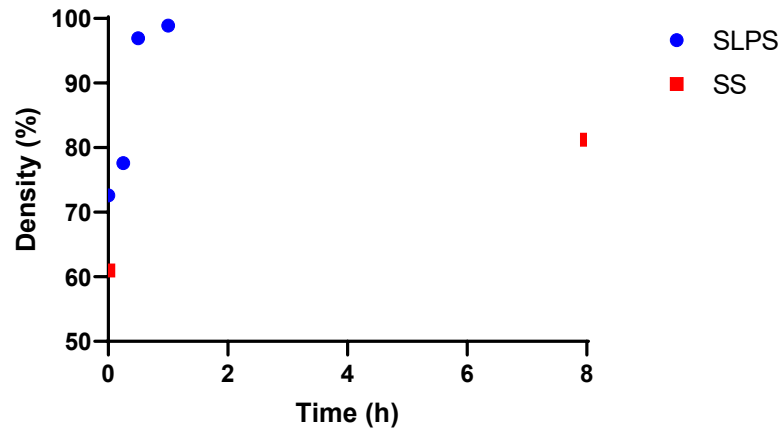


Figure 48. Archimedes density for skin samples sintered under SS and SLPS temperatures. For SLPS sintering, the time durations are 0, 0.25, 0.5 and 1 h.

Figure 48 shows the Archimedes density for sintered skin samples. The overall density evolution for the skin samples is similar to the regular samples, especially for SS sintering, as the starting density at 0 h and 8 h for skin samples are approximately 60% and 80% respectively, very close to regular samples sintered under the same conditions. However, although the SLPS samples reached near full density after 1 h, they started with a much higher density at 0 h, around 72%,

which is much higher than the 0-h density for regular samples (~60%, see Figure 27). This can be attributed to the higher green density of the core. Since the core has not been binder-jetted, no printing lines are created in the XOY-plane, hence one may anticipate less defects in the core. The higher green density of the core also results in a more homogeneous microstructure at the beginning of isothermal sintering, especially at higher sintering temperatures. As one might expect, Archimedes measurements could not separate the core and shell structures and their density evolution. Therefore μ CT scan was used to separate these structures and investigate their densities and microstructures independently using separate volume of interests in the shell and the core.

6.2.3 CT Results

CT scans for sintered skin samples were done using the same equipment and parameter settings as the “regular” samples to ensure consistent image qualities. Due to the fragile nature, the skin samples could not be characterized using CT at their green state. The detailed information concerning the conditions for the CT scans in this work can be found in section 6.1.3.

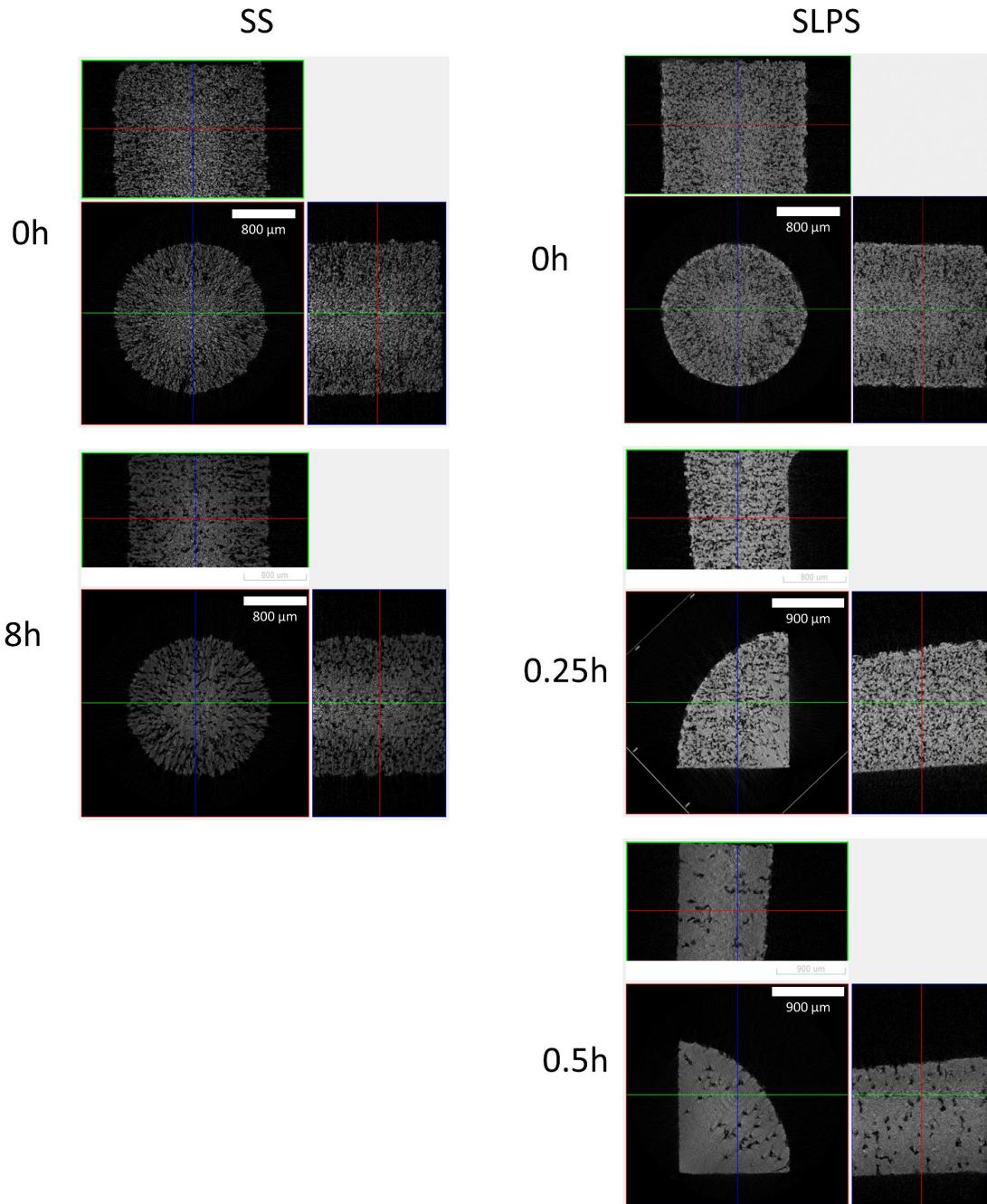


Figure 49. Reconstructed μ CT images for SS (left) and SLPS (right) skin samples, anatomical views. SLPS 1 h sample were excluded due to their high density and difficulty in X-ray penetration. SLPS 0.25 h and 0.5 h samples are cut into smaller sizes with WEDM to ensure X-ray attenuation.

Figure 49 shows the CT scanning results. It can be readily seen that for nearly all samples, the cores have higher density compared with adjacent shell structures. This correlates well with the Archimedes density measurements as well as the expectations from the printing process. However, for SS condition, although the skin samples have a denser and more homogeneous core to at the beginning of densification, they still failed to reach a final density higher than 80%. From SS 8 h imaging, a few large remnant pore sections are observed in the core. This suggests that SS sintering was not able to remove all porosities in the core, even if the core is free of printing line defects. Since the only systematic large defect type is interlayer spacings for the core, it may be inferred that the origin of remnant porosity in SS samples, regardless of normal or skin, is due to layer spreading rather than the jetting of binder. Importantly, SLPS sintering was able to repair all defects, for both the core and shell.

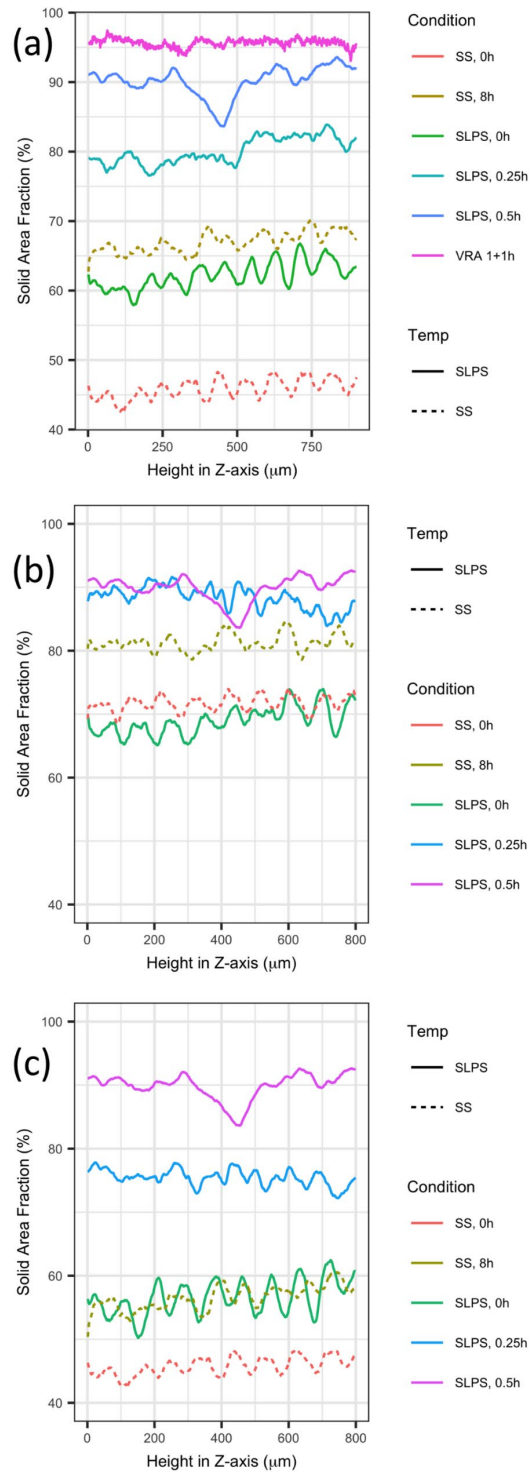


Figure 50. SAF variation along Z-direction for skin samples, sintered under SS and SLPS temperatures. (a) overall ROI, (b) SAF for core, (c) SAF for shell. For VRA sample, the core and shell are no longer distinguishable due to high final density, therefore data were not included in (b) and (c).

Figure 50 shows the 2D solid area fraction as a function of Z-coordinates. Here one may clearly see the density difference between core and shell under the same sintering condition. For SS sintering the un-jetted core started isothermal sintering at a much higher density, around 70%, compared to ~45% density for the shell. However, the core did not densify much further once it reached the SS temperature. The final density of the core stayed at ~ 80% after 8 h. On the other hand, for SLPS samples, both core and shell has densified extensively before reaching the isothermal temperature. The core reached ~ 70% and the shell reached above 55% density, the latter being similar to the 0 h density for regular samples (see Figure 27). After 0.25 h the shell is above 75%, whereas the core is approaching final stage sintering with a density of ~ 90%. At this time, there is still 15% difference between core and shell, but by 0.5 h the shell was catching up quickly, reaching a density above 90%. The next 0.5 h of sintering resulted in the final densification of microstructures with pore shrinkage and elimination, therefore at VRA 1+1 h the microstructure is essentially pore-free.

To investigate and compare microstructure evolution in core and shell regions, integrated 3D analysis has been conducted individually. Figures 51-55 show some parameters computed by CTAn software in 3D which describes different solid and pore attributes as a function of sintering time and temperature.

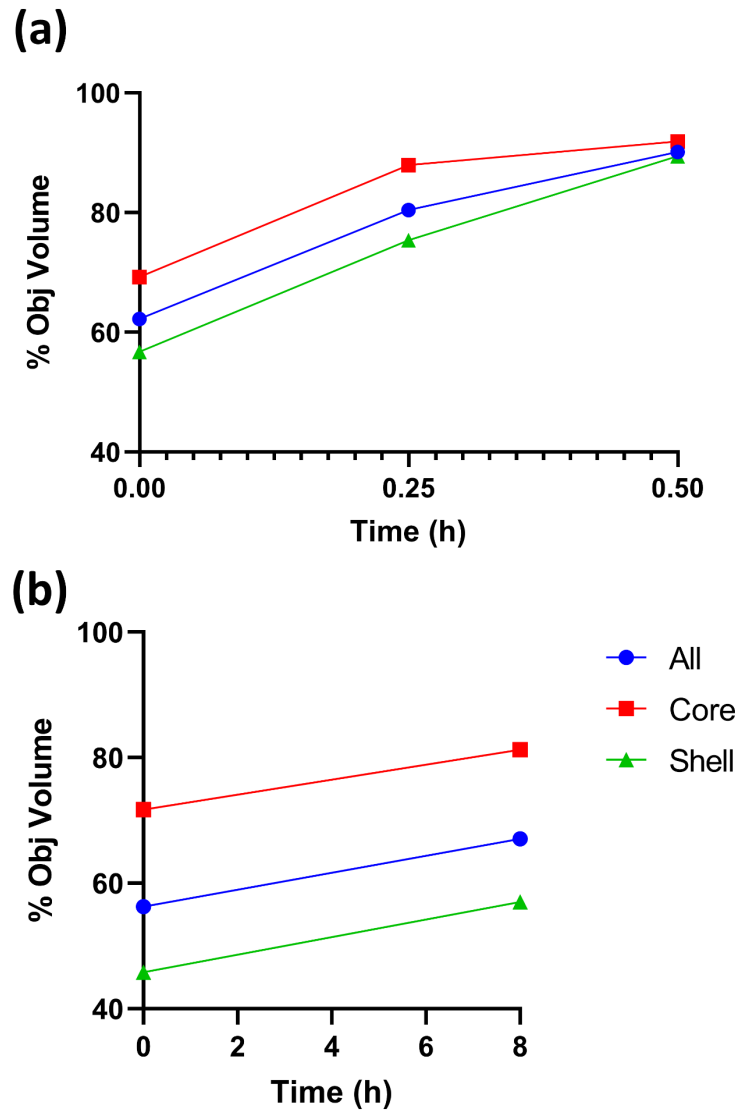


Figure 51. 3D Solid volume fraction of skin samples calculated from segmented CT images. (a) SLPS sintered, (b) SS sintered.

3D solid volume fraction plot shows good agreement with the Z-stack SAF plot in 2D. This is evidence that different analyses made by CTAn maintain internal consistency. As for the 2D results, the density gap between the core and shell remained almost constant from 0 h to 8 h for the 3D results. In contrast, the shell was able to catch up densification with the core after only 0.5 h for the SLPS samples.

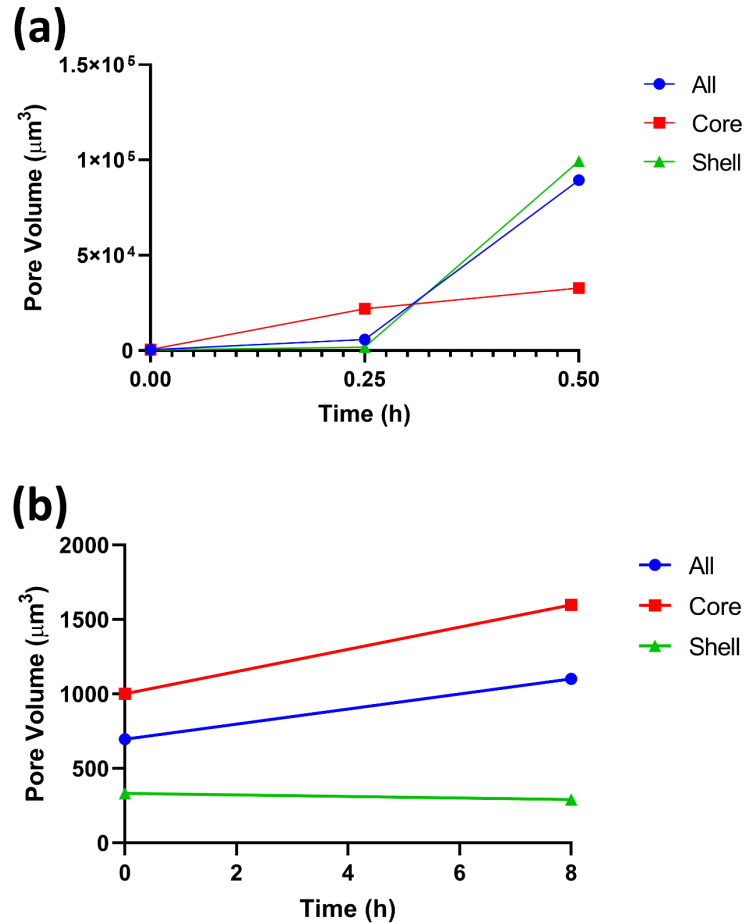


Figure 52. Average closed pore volume. (a) SLPS sintered, (b) SS sintered.

Figure 52 shows the mean closed pore volume in the microstructure, averaged by number. One needs to be cautious interpreting the trend of this average pore volume evolution, since in image processing, only pores that are fully enclosed are considered in the computation. For a low-density binder-jet printed material, especially in its green state and in the early stage of sintering, most pores are open and connected to the exterior surface. For example, in Figure 52 (b) the mean pore volume decreased slightly from 0 h to 8 h under SS sintering for the shell. In reality, it is not likely that the microstructure is densifying, since even after 8 h SS the shell density remained very low, hence most pores still remained open rather than closed. In contrast, the overall pore volume and core pore volume increased by about 50% on average. This matches the previous work[112]

that showed that SS sintering, the mean pore size, regardless of whether it was measured in 2D or 3D, increased suggesting a “coarsening” of the microstructure. Thanks to high green density and early pore closure, the mean pore volume in SLPS core evolves quite differently compared to the shell sintered under the same condition. The average pore volume for both core and shell started at a low value at 0 h SLPS, indicating a fully open initial pore structure in 3D, despite that the core has already densified to ~70%. Then by 0.25 h the core had a much higher mean pore volume, around $2 \times 10^4 \mu\text{m}^3$, while having a higher density (~85%). Again, this is probably due to pore closure as the core reached the end of intermediate stage sintering. Meanwhile the pores in the shell were still largely open. By 0.5 h SLPS, the mean pore volume for the core continue to rise as it entered final stage sintering and a large number of pores close. Interestingly, the shell at this time was able to catch up in densification and resulted in a large increase in mean pore volume. Nevertheless, both the core and the shell were able to fully densify, despite a mean pore volume as high as $\sim 10^5 \mu\text{m}^3$.

Another parameter that can be used to infer the status of pore evolution is the surface to volume ratio of the closed pores (S/V ratio), as shown in Figure 53. For SLPS samples, the S/V ratio generally decreased as densification progresses. For the shell in the SS samples, the S/V ratio increased as the sample sintered from 0 h to 8 h. Again this could be due to the closure of a few very interconnected pores. Aigeltinger et al. [67] have observed a transient increase in S/V ratio during the intermediate stage sintering of copper particles ranging from ~45% to 60% density, which is also the density range for the shell sintered under SS temperature from 0 h to 8 h.

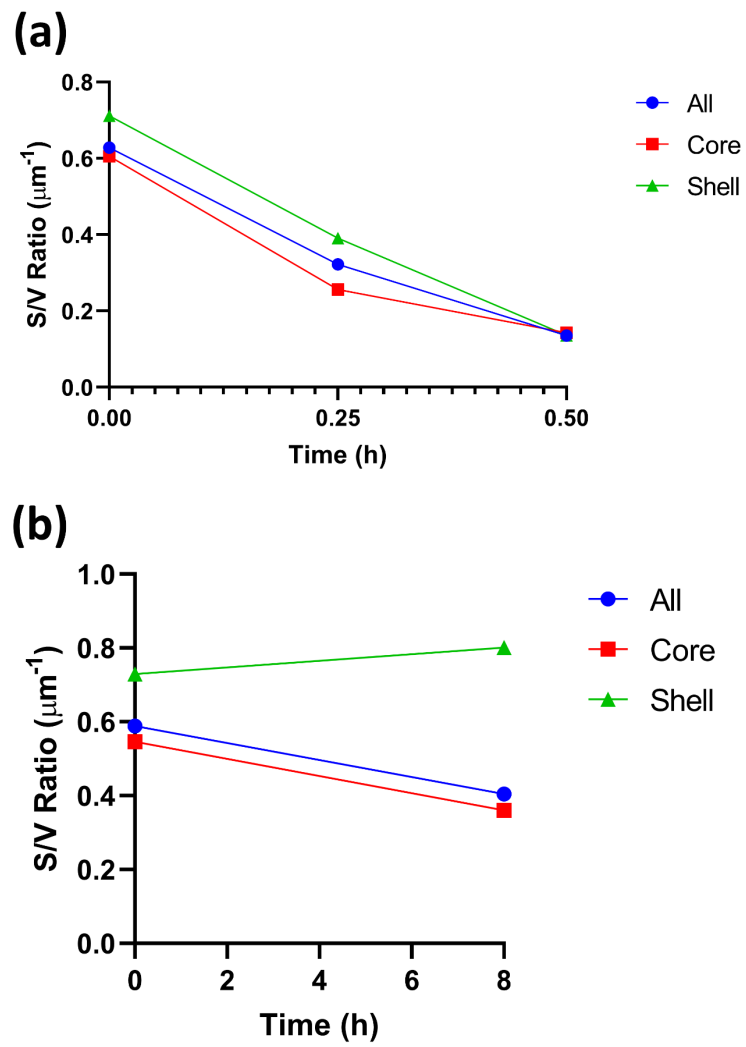


Figure 53. Closed pore surface to volume ratio. (a) SLPS sintered, (b) SS sintered.

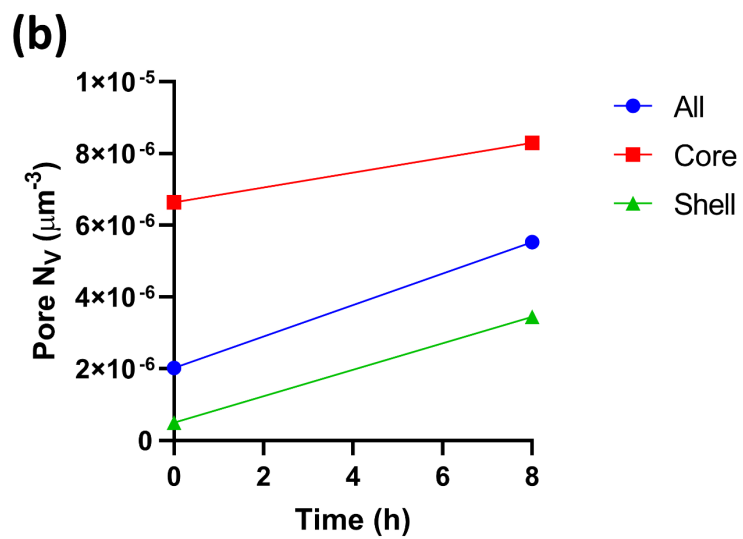
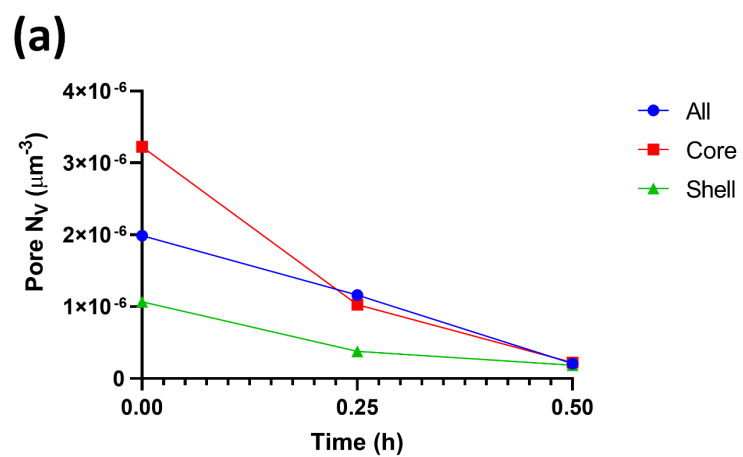


Figure 54. Closed pore number density (per unit volume). (a) SLPS sintered, (b) SS sintered.

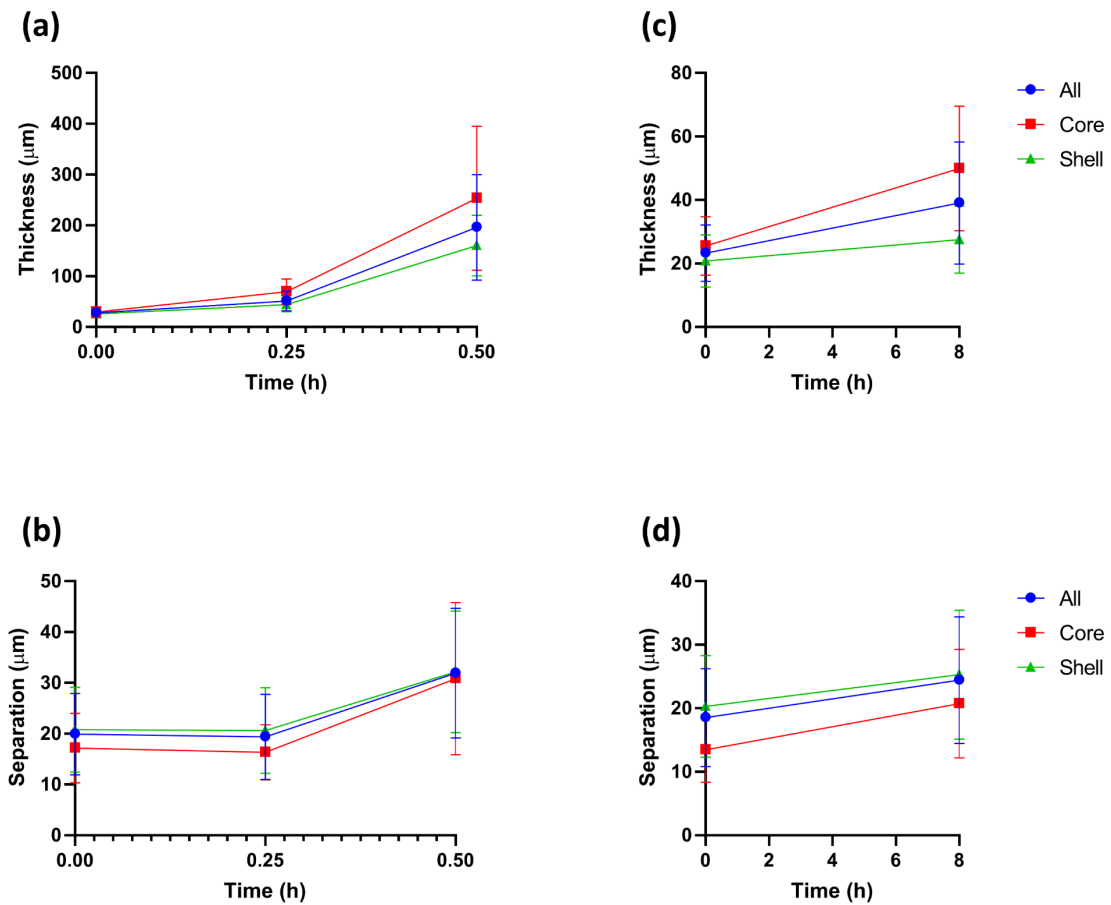


Figure 55. 3D structure thickness and separations. (a) (b) SLPS sintered, (c) (d) SS sintered. Error bars show the standard deviation of structure thickness and separation.

Similar to the regular samples, the pore number density per unit volume, N_V , shows most clearly the status of pore closure. As shown in Figure 54 (a), the general trend for pore N_V is decreasing for both the core and shell under SLPS sintering. At 0 h, the core had an N_V value of over $3 \times 10^{-6} \mu\text{m}^{-3}$, significantly higher than the shell. As discussed previously, due to the low density in the shell, most pores are connected in 3D, hence causing the reduction of N_V . In Figure 54 (b), at SS 0 h, the N_V value is similar to the SLPS 0 h in the shell, but N_V in the core is more than twice the value of the core of the SLPS 0 h and around 10 times larger than the value in the shell for SS 0 h. The high number of N_V here suggests sintering and pore closure for SS samples

in the core happened to a much less extent in the shell. This implies that differential sintering may have happened in the SS samples. The detail regarding differential sintering is discussed in section 6.2.4. Under SLPS sintering, N_V continued to decrease as sintering time increased, and by 0.5 h only a small number of closed pores were left in the microstructure. Under SS sintering, since neither the core nor the shell ever entered final stage sintering, the N_V value keep rising from 0 h to 8 h.

In the microstructure for SS 8 h sample, the overall mean N_V exceeds $5 \cdot 10^{-6} \mu\text{m}^{-3}$. This means that in this density range, the effect of pore closure outpaced the effect of pore elimination. As a result, in this microstructure, a large number of closed pores are expected. This is demonstrated in the structure thickness and separation plot shown in Figure 55. Referring to figures (c) and (d), the starting thickness and separation at SS 0 h were on the order of 10-20 μm , which correlates with the mean particle size used during printing. After 8 h, the densification in the core caused the structure thickness to increase to over 40 μm . Meanwhile little change in structure thickness was observed in the shell, suggesting limited densification. However, as the thickness increased, the structure separation did not decrease after 8 h. Again, this is possibly due to pore elimination. As a comparison, the structure thickness for SLPS samples reached more than 200 μm for the core and over 100 μm for the shell. Since the layer thickness is 100 μm in printing, this means there is a rather large, fully densified “bands” in the microstructure after 0.5 h of SLPS sintering. Meanwhile the structure thickness data is comparable to the data for SS samples.

6.2.4 Discussion

When skin samples were sintered in the early stages, differential sintering is anticipated to occur due to the difference in the packing of the particles in the core and shell. This is reflected in the Z-stack SAF plots in Figure 50. Note that for SS 0 h sample, the SAF “wave” for the skin and core are mostly synchronized, i.e., the local maxima and minima occur at the same z-coordinate, indicating that the powder spreading process had equal impact for skin and core regions. This had changed by 8 h when the peaks and valleys in density no longer match at the same z-coordinate. This means that within 8 hours of SS sintering, local regions in the core where the microstructure has significantly densified, may have created tension in the adjacent skin regions which have lower density and may have prevented the skin from densification as much as it could if it was not bonded to the core. Hence the low-SAF values at these z-coordinates. In the final microstructure, the density gap between the core and shell was not closed. For SLPS samples, at 0 h the amplitude of the SAF “wave” in the shell is much larger than SS 0 h samples, which means the shell has gone through differential sintering along the z-direction, similar to the regular samples. Meanwhile the core has densified substantially. At 0.25 h the entire sample SAF has already lost part of the sinusoidal wave behavior, suggesting efficient particle rearrangement in the presence of the wetting liquid. For the core, in this same density range (~90%) the pores would have mostly closed and entered final stage of sintering. At 0.5 h the sample has completely lost the SAF variation created by interlayer defects. Moreover, the shell was able to densify and catch up with the core. This is an indication that the initial density difference, along with effects of differential sintering between the core and shell, has been fully eliminated by the formation of viscous liquid. Both core and shell have entered final stage sintering and it is only a matter of allowing the conventional liquid phase mass transport mechanism to bring the overall microstructure to full density.

6.3 “Crucible” Samples

6.3.1 Experimental Design and Methods

In skin samples, the core was not binder-jetted therefore it avoided the printing line defects caused by jetting of the binder droplets. However, the powder in the core is still spread layer by layer, so the core still contains interlayer defects along the z-direction. To further separate the effect of layer spreading and jetting, a “crucible” sample was designed. This sample is made of a hollow cylinder, with a “shell” of 1 mm thickness and a cylindrical core with a diameter of 2 mm. A CAD model is shown in Figure 56.

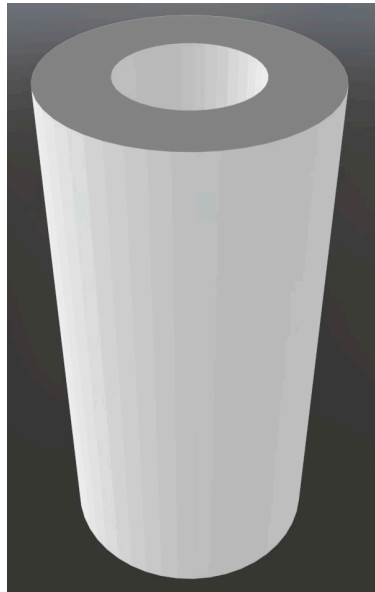


Figure 56. CAD model of a crucible sample. The inner diameter, outer diameter, and height is 2 mm, 4 mm, and 10 mm respectively.

The crucible samples were printing using X-1 Innovent printer with identical powder and parameter settings as the previous samples. After curing the binder, the un-jetted powder in the core was poured out completely. Next, the same 625 alloy powder was poured into the cavity and then gently tapped to approach efficient random powder packing. Then the samples were sintered

under the same conditions as the skin samples, i.e., SS for 0 h and 8 h, and SLPS for 0 h, 0.25 h, 0.5 h and 1 h. After sintering, the samples are sectioned using Wire EDM and CT-scanned, also using identical parameters as the regular and skin samples.

6.3.2 Results

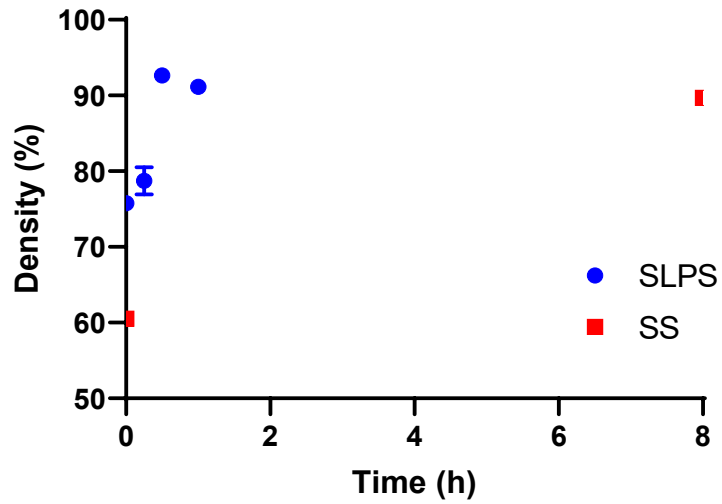


Figure 57. Sintered density for crucible samples.

Figure 57 shows the density evolution of crucible samples. The density evolved quite similar to the skin samples for the SS sintering and the majority of SLPS sintering. To better compare the density evolutions, the data for crucible samples are also plotted along with the skin and regular samples, as shown in Figure 58.

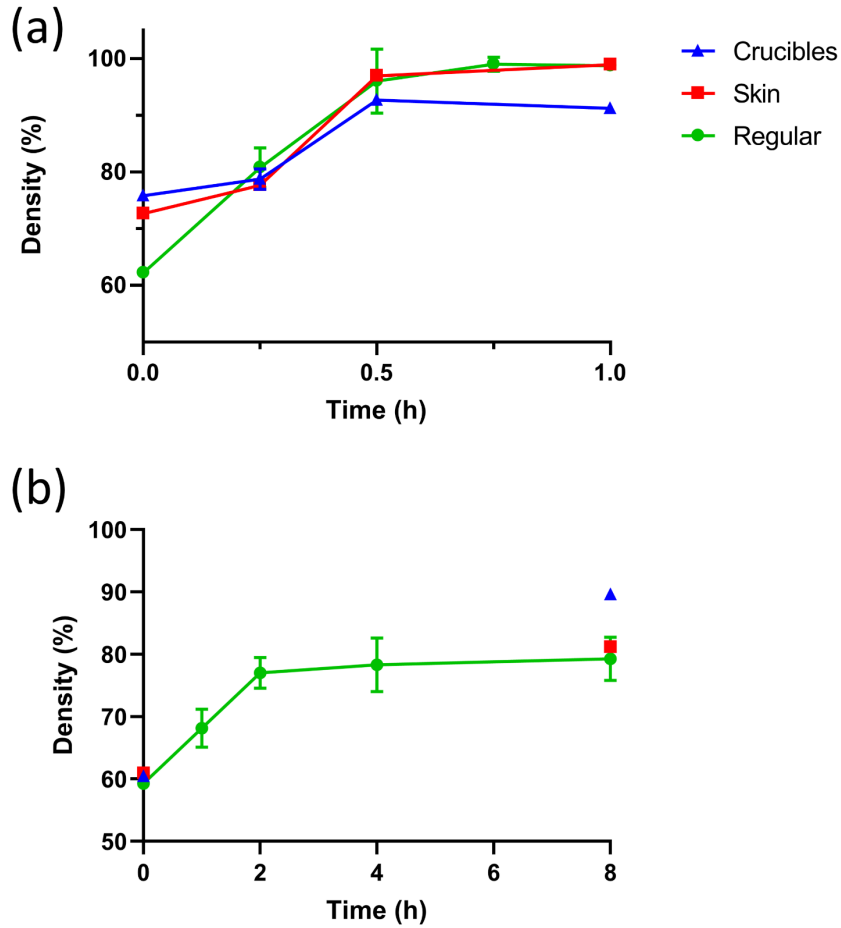


Figure 58. Comparison of densities for crucible, skin and regular samples. (a) SLPS sintering from 0 h to 1 h; (b) SS sintering from 0 h to 8 h.

The SS sintered crucible samples, just like regular and skin samples, failed to reach full density after 8 hours. However, despite similar density at SS 0 h, the crucible samples sintered for 8 h had a higher density, approximately 89%, about 10% higher than skin or regular samples. For SLPS sintered samples, the crucible behaved closer to the skin samples rather than regular samples. At 0 h the density of crucible sample was already above 75%. Its evolution at 0.25 h and 0.5 h is also very close to the skin and regular samples. However, unlike the latter two, the crucible sample did not reach near 100% density after 1 h SLPS. The densification plateaued after 0.5 h sintering, suggesting the pore structures in the crucible samples was too heterogeneous for the viscous liquid

phase to fully repair. Therefore, the densification kinetics after 0.5 h was essentially like SS samples and the densification stalled.

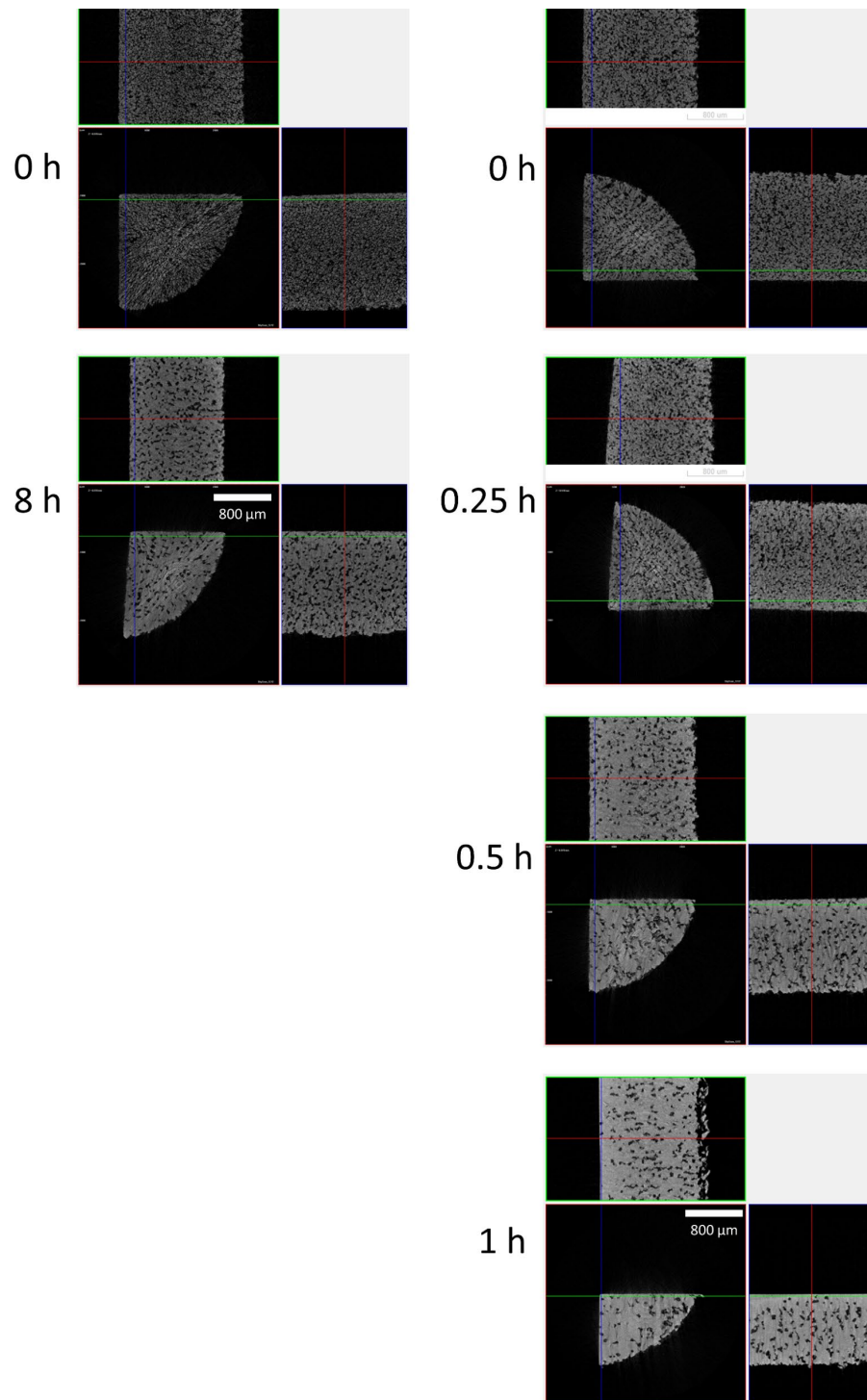


Figure 59. Reconstructed μ CT images for SS (left) and SLPS (right) crucible samples.

Figure 59 shows the reconstructed anatomical views for sintered crucible samples scanned by CT. There is remnant porosity, estimated at 10% of volume, that exists in the final microstructure after 1 h SLPS sintering. More importantly, from the images of SS 8 h and SLPS 1 h, it can be seen that several pore channels extend in the XOY plane are visible in the shell regions. This indicates that under these sintering conditions, the large printing defect in the shell caused by spreading were not repaired. This is very different from skin or regular samples sintered under SLPS temperature, since it was demonstrated that the liquid phase formation could repair interlayer defects and promotes densification. More details can be obtained from the 2D solid area fraction plots from the Z stacks.

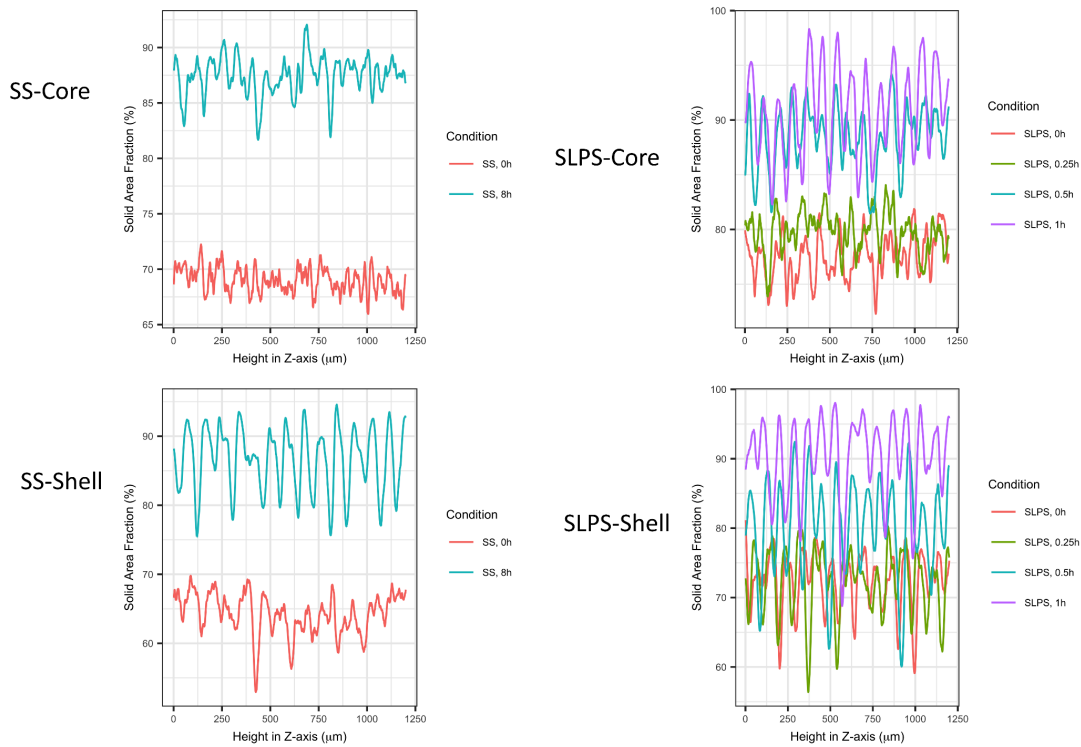


Figure 60. SAF variation along Z-direction for crucible samples, sintered under SS and SLPS temperatures.

Figure 60 shows the solid area fraction of crucible samples measured from the Z-stack CT image dataset. For SS samples, the SAF evolution generally matches that of the skin samples, although the shell has been densified to a much higher density (~65% average) at SS 0 h in the

crucible samples. Like the skin samples the core of the crucible samples started with a higher density, since the core was free of any type of printing defects. Both the core and shell stopped at a final density of $\sim 85\%$ average after 8 h of SS sintering. It is interesting to see that the shell was actually able to catch up with the densification in the core, possibly because it had a higher density when it reached the sintering temperature, nevertheless they still fail reach final stage densification. For SLPS samples, the evolution of shell and core was also very similar to each other, and also similar to the skin samples. The shell started at a relatively lower density at 0 h, compared to the core, and was able to overcome most of this disadvantage after 1 h SLPS. However, just like SS samples, the microstructure did not reach full density. The final density for both core and shell for the SLPS 1 h sample was $\sim 90\%$.

One very interesting conclusion from Figure 56 is that the core is supposed to be free of any type of printing defects, since the powder was deposited by hand-pouring and tapping, not through the printing process. However, one clearly sees the sinusoidal wave behavior in the SAF plot for the cores, especially for longer sintering times. For instance, the “amplitude” of the SAF wave is much more significant for SS 8 h core compared to SS 0 h core, reaching a maximum amplitude of $\sim 10\%$. Similarly, the maximum amplitude for the SLPS 1 h core is as high as $\sim 15\%$. For shell region, this amplitude is even larger ($\sim 29\%$ for SLPS 1 h shell). This suggests the microstructural heterogeneity caused by differential sintering gets worse during sintering and cannot be repaired. With a density below 70%, the low-density regions in the shell of the crucible samples were never able to be repaired, and so the pores were never closed. This resulted in remnant porosity that has a length scale of multiple particle sizes in the final microstructure.

6.3.3 Discussion

The appearance of the wave behavior in the core of the crucible samples is unexpected. This might be attributed to differential sintering. Given the high green density and more homogeneous microstructure of the core, it was anticipated that it would densify faster than the shell in the initial stages of sintering. Extensive densification in the core may have occurred even as the sample reached the supersolidus sintering temperature at SLPS 0 h, since there are no printing layers. If the packing is homogeneous in the core, then the densification rate along the Z direction would be homogeneous (same densification rate at all locations along the Z-direction). However, the densification rate along the Z-direction in the shell differs between the dense powder layers and the defective interlayer regions. Therefore, one would expect the locations in the interlayer regions of the shell would densify more slowly. As a result, tension would be created between the densifying core and the shell and that will vary along the Z direction and such variation will follow the same periodic pattern as the microstructure of the shell. Therefore, differential sintering may occur in the core in the early stages of sintering in response to this sinusoidal tension, resulting in a periodic variation in density in the core along the Z direction. In this case, the formation of liquid phase in SLPS may, in fact, have worsen the scenario by allowing particles to move more freely under the sinusoidal stress state created by differential sintering. If the particle rearrangement in the core caused them to move horizontally in the XOY plane into the more porous interlayer region in the shell, this would create defects in the core at a Z-coordinate corresponding to the interlayer regions in the shell, thus causing even larger amplitude wave behavior as one sees in the SAF plot. Evidence that supports this hypothesis is that, for the core and the shell, the phase of the SAF waves in SLPS samples is synchronized to a certain extent after 1 h sintering, indicating that the density in the core is lower in the regions that correspond to the interlayer regions in the

shell. This is also supported by the reconstructed anatomical view of SLPS 1 h sample (see the sideview of SLPS 1 h sample in Figure 59), where the linear pore channels are visible and extend throughout the width of the sample and into the core. This effect is much more pronounced in the crucible samples, because 1) the density in the core is the highest in the crucible samples, so the tension created at the interface is larger; and 2) the thickness ratio of shell to core in the crucible samples (1:1) are much larger than the same ratio in the skin samples. Although the size of the crucible sample is relatively small (4 mm outer diameter for the shell, 2 mm inner diameter for the core), a line of particles across the core used in this study (average $\sim 25 \mu\text{m}$ in size) will consist of ~ 80 particles. Since the effect of planar container surfaces on particle packing usually affects no more than a few particle widths, it can be concluded that the majority of the core powder packing was not affected by the surface with the shell at its green state. A schematic sketch showing a possible differential sintering and particle rearrangement mechanism is illustrated in Figure 61. To fully reveal the interactions between the core and the shell and its impact on final microstructures, more systematic and careful examinations are required, which is beyond the scope of this work.

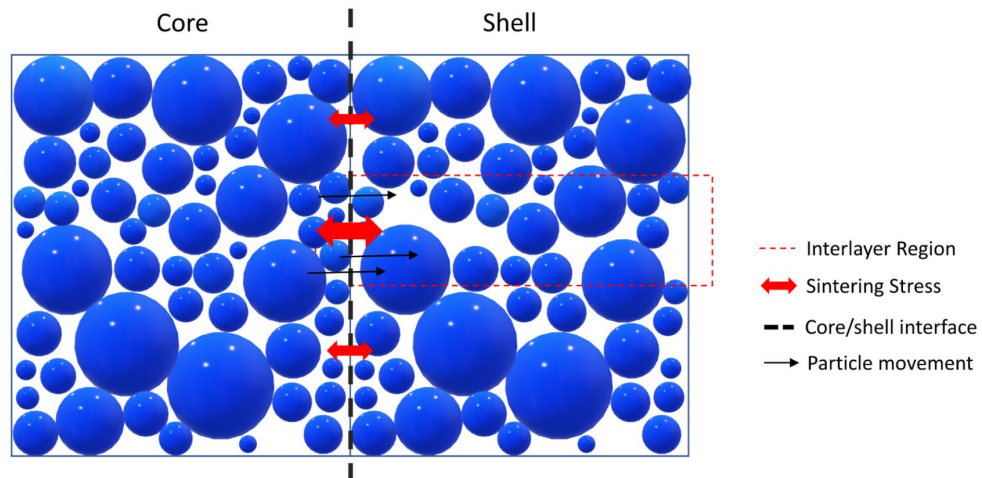


Figure 61. A proposed schematic (XOZ-view) of the differential sintering and rearrangement during SLPS sintering of the crucible samples. The size of the red arrows shows the relative magnitude of sintering stresses.

7.0 Conclusions

In this work, microstructure evolution investigations have been applied to binder-jet printed and sintered, gas-atomized Inconel 625 alloy in both two- and three-dimensions. Three types of samples were designed and printed to investigate the evolution of the pore phase created by binder-jet printing, namely regular printed structures, the “skin” structures and the “crucible” structures. These structures were printed to investigate the relative contributions of powder spreading and binder-jetting to remnant porosity. All samples were then isothermal sintered under subsolidus and supersolidus temperatures. Additionally, a two-step VRA sintering process has been developed and applied on selected samples to remove remnant porosity in pressureless sintering while minimizing elemental segregation in the final microstructure. Quantitative field and feature measurements were conducted on 2D and 3D microstructural images. The following conclusions are drawn:

1. The viscous liquid assisted (VRA) sintering is able to fully densify binder-jetted 625 alloy powders, but the segregation of the chemical elements could not be entirely eliminated, even after 12 hours of subsolidus heat treatment. Large sample-to-sample variations have been found for VRA samples in terms of liquid phase fraction. Nevertheless, the liquid content generally decreases when the SS sintering time was prolonged in the second step.

2. The utility of 3D characterization using μ CT for microstructure analysis has been demonstrated. Comparison between 2D traditional characterization techniques and CT results showed good agreement in terms of the evolution of some characteristics of the pore

phase. The difference in microstructural evolution between SS and SLPS sintering can be described

3. Based on CT imaging, the solid area fraction plot coupled with the orientation analyses on pore phases revealed that subsolidus sintering could remove defects originating from the jetting process in part of the dense regions inside the material but failed to repair the interlayer defects caused by powder spreading. The presence of liquid phase in SLPS could repair both types of defects and homogenize the pore structure. Therefore, the remnant porosity in a sintered printed powder system is more likely to originate from the powder spreading rather than the jetting process.

4. Differential sintering is observed in all printed samples resulting in sinusoidal patterns in the pore structure along the Z direction. During SLPS sintering the microstructure first becomes less homogeneous due to differential sintering before becoming more homogeneous which allows the pores to be removed in as little as one hour. This is due to the systematic and highly oriented packing defects introduced during the printing process.

5. The “skin” samples were able to fully densify under the same sintering conditions despite enhanced differential sintering between the skin and the core. The latter is thought to not contain defects created by the jetting. The crucible samples failed to reach full density after 1 h SLPS sintering. This is thought to be due to the extent of differential sintering at the core-shell interfaces. In this case the core was thought to contain neither jetting nor spreading defects. The size of the crucible samples, particularly the relative thickness of the shell, is thought to play a vital role determining the sinterability of the

sample since it controls the extent that differential sintering between the core and the shell can influence sintering in the core.

8.0 Future Work

1. Establish quantitative process-structure relationships between printing parameters, the green microstructure and microstructure evolution in sintering using 3d microstructure analysis. This should include tuning of particle size distributions, binder saturations and the powder spreading parameters such as layer thickness, etc. Since the green microstructure bridges the printing process and the final microstructure after sintering it may be possible to directly predict sintering behavior from 3D imaging of the green microstructure.

2. Screen and develop a series of 3D microstructure pathway descriptors to describe the microstructure evolution during sintering. One or a few key pathway parameters could be very useful in quantifying pore closure and its effect on sintering.

3. Further development of VRA sintering should consider more sintering conditions in order to reliably eliminate the second phases in the final microstructures caused by supersolidus sintering. Scaling up the printed samples may also be necessary to ensure utility in large-batch industrial manufacturing.

4. A more rigorous investigation of the mechanism of differential sintering in the crucible samples should be conducted. This could focus on the effect of the printed shell structure on the sintering of the core. This may be achieved by altering the shape and shell thickness of the samples, scaling up/down the sample size, and in-situ imaging using μ CT while sintering. lightly sintered skin and crucible structures may have a broad utility for manufacturing controlled porous structures for filtration applications or duplex materials that have different materials in the core and the shell.

Appendix A Stereological Parameters, Topological Measurements and Microstructural Pathways

2D:

Name	Symbol	Calculation	Unit
Stereology			
Solid volume fraction	V_V	$V_V = P_P = L_L = A_A$	N/A
Point counting	P_P		
Intercept length	L_L		
Area fraction (distribution)	A_A		
Surface area per unit volume	S_V	$S_V = 2P_L = \frac{4}{\pi} L_A$	1/length
Solid-solid surface area/unit volume	S_V^{SS}		1/length
Solid-vapor surface area/unit volume	S_V^{SV}		1/length
Mean pore intercept length	$\bar{\lambda}^V$	$\bar{\lambda}^V = \frac{4(1 - V_V)}{S_V^{SV}}$	length
Mean grain intercept length	$\bar{\lambda}_g^S$	$\bar{\lambda}_g^S = \frac{4V_V}{S_V^{SV} + 2S_V^{SS}}$	length

Number of pores/unit area	NA		1/area
Microstructure Pathway			
Solid-vapor surface area ratio	Ψ	$\Psi = \frac{S_V^{SS}}{S_V^{SV}}$	N/A
Mean grain intercept length to mean pore intercept ratio	Λ	$\Lambda = \frac{\bar{\lambda}_g^S}{\bar{\lambda}_V^S}$ $= \frac{V_V \cdot S_V^{SV}}{(1 - V_V)(S_V^{SV} + 2S_V^{SS})}$	N/A
Mean pore spacing	$\bar{\lambda}_P^S$	$\bar{\lambda}_P^S = \frac{4V_V}{S_V^{SV}}$	length
Mean pore spacing to mean grain intercept length ratio	Σ	$\Sigma = \frac{\bar{\lambda}_P^S}{\bar{\lambda}_g^S} = \frac{S_V^{SV} + 2S_V^{SS}}{S_V^{SV}}$	N/A
Shape Descriptors			
Circularity	Circ.	$\text{Circ.} = \sqrt{\frac{4\pi A}{P^2}}$	N/A
Solidity	Solid.	$S = \frac{A}{A_c}$	N/A
Aspect Ratio	AR	$AR = \frac{x_{F \min}}{x_{F \max}}$	N/A
Roundness	Round.	Round. = 1/AR	N/A

3D:

Name	Symbol	Calculation	Unit
Stereology			
Solid volume fraction	V_V	$V_V = P_P = L_L = A_A$	N/A
Surface area per unit volume	S_V	$S_V = 2P_L = \frac{4}{\pi} L_A$	1/length
Solid-solid surface area/unit volume	S_V^{SS}		1/length
Solid-vapor surface area/unit volume	S_V^{SV}		1/length
Mean pore intercept length	$\bar{\lambda}^V$	$\bar{\lambda}^V = \frac{4(1 - V_V)}{S_V^{SV}}$	length
Mean grain intercept length	$\bar{\lambda}_g^S$	$\bar{\lambda}_g^S = \frac{4V_V}{S_V^{SV} + 2S_V^{SS}}$	length
Number of pores/unit volume	N_V		1/volume
Microstructure Pathway			
Solid-vapor surface area ratio	Ψ	$\Psi = \frac{S_V^{SS}}{S_V^{SV}}$	N/A
3D Mean grain intercept length to mean pore intercept ratio	Λ	$\Lambda = \frac{\bar{\lambda}_g^S}{\bar{\lambda}^V}$ $= \frac{V_V \cdot S_V^{SV}}{(1 - V_V)(S_V^{SV} + 2S_V^{SS})}$	N/A

3D Mean pore spacing	$\bar{\lambda}_P^S$	$\bar{\lambda}_P^S = \frac{4V_V}{S_V^{SV}}$	length
3D Mean pore spacing to mean grain intercept length ratio	Σ	$\Sigma = \frac{\bar{\lambda}_P^S}{\bar{\lambda}_g^S} = \frac{S_V^{SV} + 2S_V^{SS}}{S_V^{SV}}$	N/A
Shape Descriptors			
Circularity/Sphericity	<i>Spher.</i>	$\sqrt[3]{36\pi(V^2/SA^3)}$	N/A
Solidity	Solid.	$\frac{V}{V_c}$	N/A
Aspect Ratio	AR	$AR = \frac{x_{F \min}}{x_{F \max}}$	N/A
Roundness	Round.	Round. = 1/AR	N/A
Curvature distribution	κ	TBD	1/length
Topologies			
Euler number	Eu.	$\chi = \beta_0 - \beta_1 + \beta_2$	N/A
Fragmentation index	F	$F = \left(\frac{S_1 - S_2}{V_1 - V_2} \right)$	N/A
Fractal Dimension	FD	$FD = \lim_{\varepsilon \rightarrow 0} \frac{\log N(\varepsilon)}{\log \frac{1}{\varepsilon}}$	N/A

Appendices contain supplementary or illustrative material or explanatory data too lengthy to be included in the text or not immediately essential to the reader's understanding of the text.

When using the Appendix Style, type the title of the Appendix section after the inserted heading.

Bibliography

- [1] R.M. German, Powder Metallurgy Science, 2nd ed., Metal Powder Industries Federation, 1994.
- [2] G.H. Gessinger, Powder metallurgy of superalloys, Butterworths, 1984.
- [3] H. Fecht, D. Furrer, Processing of nickel-base superalloys for turbine engine disc applications, *Advanced Engineering Materials*. 2 (2000) 777–787. [https://doi.org/10.1002/1527-2648\(200012\)2:12<777::AID-ADEM777>3.0.CO;2-R](https://doi.org/10.1002/1527-2648(200012)2:12<777::AID-ADEM777>3.0.CO;2-R).
- [4] J.M. Torralba, M. Campos, Toward high performance in Powder Metallurgy, *Revista de Metalurgia*. 50 (2014). <https://doi.org/10.3989/revmetalm.017>.
- [5] ASTM, Standard Terminology for Additive Manufacturing – General Principles – Terminology, ASTM International. i (2015) 1–9. <https://doi.org/10.1520/F2792-12A.2>.
- [6] E.M. Sachs, J.S. Haggerty, M.J. Cima, P.A. Williams, Three-dimensional Printing Techniques, 5204055, 1993.
- [7] A. Zocca, J. Günster, A. Zocca, P. Lima, J. Günster, LSD-based 3D printing of alumina ceramics Laser-Induced Slip casting (LIS) of ceramic and geopolymere materials View project AMITIE View project LSD-based 3D printing of alumina ceramics, *Journal of Ceramic Science and Technology*. 8 (2017) 141–148. <https://doi.org/10.4416/JCST2016-00103>.
- [8] B.D. Kernan, E.M. Sachs, M.A. Oliveira, M.J. Cima, Three Dimensional Printing of Tungsten Carbide-Cobalt using a Cobalt Oxide Precursor †, in: 2003 International Solid Freeform Fabrication Symposium, 2003: pp. 616–631.
- [9] J.A. Gonzalez, J. Mireles, Y. Lin, R.B. Wicker, Characterization of ceramic components fabricated using binder jetting additive manufacturing technology, *Ceramics International*. 42 (2016) 10559–10564. <http://www.elsevier.com/open-access/userlicense/1.0/> (accessed April 9, 2022).
- [10] B. Cheng, S. Shrestha, Y.K. Chou, Stress and deformation evaluations of scanning strategy effect in selective laser melting, in: ASME 2016 11th International Manufacturing Science and Engineering Conference, Blacksburg, VA, 2016.
- [11] E.R. Denlinger, J. Irwin, P. Michaleris, Thermomechanical Modeling of Additive Manufacturing Large Parts, *Journal of Manufacturing Science and Engineering*. 136 (2014) 061007. <https://doi.org/10.1115/1.4028669>.

- [12] E.R. Denlinger, M. Gouge, J. Irwin, P. Michaleris, Thermomechanical model development and in situ experimental validation of the Laser Powder-Bed Fusion process, *Additive Manufacturing*. 16 (2017) 73–80. <https://doi.org/10.1016/j.addma.2017.05.001>.
- [13] S.M. Thompson, L. Bian, N. Shamsaei, A. Yadollahi, An overview of Direct Laser Deposition for additive manufacturing; Part I: Transport phenomena, modeling and diagnostics, *Additive Manufacturing*. 8 (2015) 36–62. <https://doi.org/10.1016/j.addma.2015.07.001>.
- [14] N. Shamsaei, A. Yadollahi, L. Bian, S.M. Thompson, An overview of Direct Laser Deposition for additive manufacturing; Part II: Mechanical behavior, process parameter optimization and control, *Additive Manufacturing*. 8 (2015) 12–35. <https://doi.org/10.1016/j.addma.2015.07.002>.
- [15] A. Mostafaei, E.L. Stevens, J.J. Ference, D.E. Schmidt, M. Chmielus, Binder jetting of a complex-shaped metal partial denture framework, *Additive Manufacturing*. 21 (2018) 63–68. <https://doi.org/10.1016/j.addma.2018.02.014>.
- [16] T. Do, T.J. Bauder, H. Suen, K. Rego, J. Yeom, P. Kwon, Additively Manufactured Full-Density Stainless Steel 316L With Binder Jet Printing, in: *Proceedings of the ASME 2018 International Manufacturing Science and Engineering Conference MSEC2018*, College Station, TX, 2018: pp. 1–10. <https://doi.org/10.1115/MSEC2018-6681>.
- [17] A. Levy, A. Miriyev, A. Elliott, S.S. Babu, N. Frage, Additive manufacturing of complex-shaped graded TiC/steel composites, *Materials & Design*. 118 (2017) 198–203. <https://doi.org/10.1016/j.matdes.2017.01.024>.
- [18] D. Hong, D.-T. Chou, O.I. Velikokhatnyi, A. Roy, B. Lee, I. Swink, I. Issaev, H.A. Kuhn, P.N. Kumta, Binder-jetting 3D printing and alloy development of new biodegradable Fe-Mn-Ca/Mg alloys, *Acta Biomaterialia*. 45 (2016) 375–386. <https://doi.org/10.1016/j.actbio.2016.08.032>.
- [19] A. Mostafaei, K.A. Kimes, E.L. Stevens, J. Toman, Y.L. Krimer, K. Ullakko, M. Chmielus, Microstructural evolution and magnetic properties of binder jet additive manufactured Ni-Mn-Ga magnetic shape memory alloy foam, *Acta Materialia*. 131 (2017) 482–490. <https://doi.org/10.1016/j.actamat.2017.04.010>.
- [20] P. Nandwana, A.M. Elliott, D. Siddel, A. Merriman, W.H. Peter, S.S. Babu, Powder bed binder jet 3D printing of Inconel 718: Densification, microstructural evolution and challenges☆, *Current Opinion in Solid State and Materials Science*. 21 (2017) 207–218. <https://doi.org/10.1016/j.cossms.2016.12.002>.
- [21] A. Mostafaei, P.R. De Vecchis, I. Nettleship, M. Chmielus, Effect of powder size distribution on densification and microstructural evolution of binder-jet 3D-printed

- alloy 625, *Materials & Design*. 162 (2018) 375–383. <https://doi.org/10.1016/j.matdes.2018.11.051>.
- [22] C.L. Cramer, H. Armstrong, A. Flores-Betancourt, L. Han, A.M. Elliott, E. Lara-Curzio, T. Saito, K. Nawaz, Processing and properties of SiC composites made via binder jet 3D printing and infiltration and pyrolysis of preceramic polymer, *International Journal of Ceramic Engineering & Science*. 2 (2020) 320–331. <https://doi.org/10.1002/ces2.10070>.
- [23] R. Sreeja, B. Swaminathan, A. Painuly, T. v. Sebastian, S. Packirisamy, Allylhydridopolycarbosilane (AHPCS) as matrix resin for C/SiC ceramic matrix composites, *Materials Science and Engineering B: Solid-State Materials for Advanced Technology*. 168 (2010) 204–207. <https://doi.org/10.1016/j.mseb.2009.12.033>.
- [24] A. Mostafaei, A.M. Elliott, J.E. Barnes, F. Li, W. Tan, C.L. Cramer, P. Nandwana, M. Chmielus, Binder jet 3D printing—Process parameters, materials, properties, modeling, and challenges, *Progress in Materials Science*. 119 (2021). <https://doi.org/10.1016/j.pmatsci.2020.100707>.
- [25] R.K. McGeary, Mechanical Packing of Spherical Particles, *Journal of the American Ceramic Society*. 44 (1961) 513–522. <https://doi.org/doi:10.1111/j.1151-2916.1961.tb13716.x>.
- [26] G.P. Bierwagen, T.E. Sanders, Studies of the Effects of Particle Size Distribution on the Packing Efficiency of Particles, *Powder Technology*. 10 (1974) 111–119. [https://doi.org/10.1016/0032-5910\(74\)80036-7](https://doi.org/10.1016/0032-5910(74)80036-7).
- [27] LEE, D. L., Packing of Spheres and its Effect on the Viscosity of Suspension, *J. Paint Technol*. 42 (1970) 579–584.
- [28] T. Fan, A. Lauder, E.E. Sachs, M.J. Cima, The Surface Finish in Three Dimensional Printing, in: *The Third International Conference on Rapid Prototyping*, University of Dayton, Dayton, 1992: pp. 63–72.
- [29] T. Fan, *Droplet-Powder Impact Interaction in Three Dimensional Printing*, Massachusetts Institute of Technology, 1995.
- [30] S. Shrestha, G. Manogharan, Optimization of Binder Jetting Using Taguchi Method, *Jom*. 69 (2017) 491–497. <https://doi.org/10.1007/s11837-016-2231-4>.
- [31] E. Sachs, M. Cima, J. Cornie, D. Brancazio, J. Brecht, A. Curodeau, T. Fan, S. Khanuja, A. Lauder, J. Lee, S. Michaels, Three-Dimensional Printing: The Physics and Implications of Additive Manufacturing, *CIRP Annals - Manufacturing Technology*. 42 (1993) 257–260. [https://doi.org/10.1016/S0007-8506\(07\)62438-X](https://doi.org/10.1016/S0007-8506(07)62438-X).
- [32] A. Mostafaei, E.L. Stevens, E.T. Hughes, S.D. Biery, C. Hilla, M. Chmielus, Powder bed binder jet printed alloy 625: Densification, microstructure and mechanical

- properties, *Materials and Design*. 108 (2016) 126–135. <https://doi.org/10.1016/j.matdes.2016.06.067>.
- [33] M.Yu. Bal'shin, N. V. Zakharyan, N. V. Manukyan, Calculation of the relationship between compaction pressure and the density of metal powders, *Soviet Powder Metallurgy and Metal Ceramics*. 12 (1973) 372–375. <https://doi.org/10.1007/BF00791261>.
- [34] N.I. Shcherban, Effect of porosity on the Mechanical Properties of Materials Produced by Powder Metallurgy Techniques, *Powder Metallurgy and Metal Ceramics*. 12 (1973) 736–748.
- [35] S.D. Brown, R.B. Biddulph, P.D. Wilcox, A Strength-Porosity Relation Involving Different Pore Geometry and Orientation, *Journal American Ceramic Society*. 47 (1964) 320–322.
- [36] A. Yegyan Kumar, J. Wang, Y. Bai, S.T. Huxtable, C.B. Williams, Impacts of process-induced porosity on material properties of copper made by binder jetting additive manufacturing, *Materials & Design*. 182 (2019) 108001. <https://doi.org/10.1016/j.matdes.2019.108001>.
- [37] K. Torii, M. Kawamura, A STUDY ON THE RELATIONSHIP BETWEEN STRENGTH PORE SIZE DISTRIBUTION IN COMPACTED STABILIZED AND SOILS, *Proceedings of the Japan Society of Civil Engineers*. (1988) 131–140. https://doi.org/10.2208/jscej.1988.400_131.
- [38] D. Hou, D. Li, P. Hua, J. Jiang, G. Zhang, Statistical modelling of compressive strength controlled by porosity and pore size distribution for cementitious materials, *Cement and Concrete Composites*. 96 (2019) 11–20. <https://doi.org/10.1016/J.CEMCONCOMP.2018.10.012>.
- [39] M. Zakeri, A. Samimi, M. Shafiee Afarani, A. Salehirad, Effects of porosity and pore size distribution on mechanical strength reliability of industrial-scale catalyst during preparation and catalytic test steps, *Particulate Science and Technology*. 36 (2018) 96–103. <https://doi.org/10.1080/02726351.2016.1220437>.
- [40] K. Kapat, P. Kumar Srivas, A. Prabhu Rameshbabu, P. Prasanna Maity, S. Jana, J. Dutta, P. Majumdar, D. Chakrabarti, S. Dhara, Influence of Porosity and Pore-Size Distribution in Ti 6 Al 4 V Foam on Physicomechanical Properties, Osteogenesis, and Quantitative Validation of Bone Ingrowth by Micro-Computed Tomography, *ACS Applied Materials & Interfaces*. 9 (2017) 39235–39248. <https://doi.org/10.1021/acsami.7b13960>.
- [41] F.H. Froes, Developments in Titanium Powder Metallurgy, *JOM*. 32 (1980) 47–54. <https://doi.org/10.5357/koubyou.56.453>.
- [42] H. Wang, Z. Fang, P. Sun, A critical review of mechanical properties of powder metallurgy titanium, *International Journal of Powder Metallurgy*. 46 (2010) 45–57.

- [43] Y. Chiang, D.P. Birnie, W.D. Kingery, *Physical ceramics*, J. Wiley, 1997.
- [44] R.L. Coble, Sintering crystalline solids. I. intermediate and final state diffusion models, *Journal of Applied Physics*. 32 (1961) 787–792. <https://doi.org/10.1063/1.1736107>.
- [45] R.T. DeHoff, A Cell Model for Microstructural Evolution during Sintering, in: *Materials Science Research*, Springer US, Boston, MA, 1984: pp. 23–34. https://doi.org/10.1007/978-1-4613-2761-5_2.
- [46] R.H.R. Castro, D. Gouvea, Sintering and Nanostability: The Thermodynamic Perspective, *Journal of the American Ceramic Society*. 99 (2016) 1105–1121. <https://doi.org/10.1111/jace.14176>.
- [47] W.B. Burdett, P. Hurrell, A. Gilleland, Hot Isostatic Pressing of Austenitic Stainless Steel Powders for Pressure Retaining Applications, in: *Fracture Methodologies and Manufacturing Processes*, ASME, 2004: pp. 153–160. <https://doi.org/10.1115/PVP2004-2311>.
- [48] V. Samarov, C. Barre, E. Khomyakov, R. Haykin, Net Shape HIP For Complex Shape PM Parts As A Cost-Efficient Industrial Technology, in: *Proceedings of 2005 International Conference on Hot Isostatic Pressing*, Paris, 2005: pp. 48–52.
- [49] J.D. Hansen, R.P. Rusin, M.-H. Teng, D.L. Johnson, Combined-Stage Sintering Model, *Journal of the American Ceramic Society*. 75 (1992) 1129–1135. <https://doi.org/10.1111/j.1151-2916.1992.tb05549.x>.
- [50] J.-M. Ting, R.Y. Lin, Effect of particle-size distribution on sintering Part I Modelling, *JOURNAL OF MATERIALS SCIENCE*. 29 (1994) 1867–1872.
- [51] C.H. Hsueh, A.G. Evans, R.L. Coble, Microstructure development during final/intermediate stage sintering—I. Pore/grain boundary separation, *Acta Metallurgica*. 30 (1982) 1269–1279. [https://doi.org/10.1016/0001-6160\(82\)90145-6](https://doi.org/10.1016/0001-6160(82)90145-6).
- [52] J.-M. Ting, R.Y. Lin, Effect of particle size distribution on sintering Part II Sintering of alumina, *JOURNAL OF MATERIALS SCIENCE*. 30 (1995) 2382–2389.
- [53] F.F. Lange, Sinterability of Agglomerated Powders, *Journal of the American Ceramic Society*. 67 (1984) 83–88.
- [54] C. Herring, Effect of Change of Scale on Sintering Phenomena, *Journal of Applied Physics*. 21 (1950) 301–303. <https://doi.org/10.1063/1.1699658>.
- [55] I. Nettleship, T. Chen, K. Ewsuk, Characterization of Heterogeneous Microstructure Evolution in ZrO₂-3 mol%Y₂O₃ during Isothermal Sintering, *Journal of the American Ceramic Society*. 90 (2007) 3793–3799. <https://doi.org/10.1111/j.1551-2916.2007.02052.x>.

- [56] T. Chen, I. Nettleship, R.J. McAfee, T.R. Hinklin, K.G. Ewsuk, An Experimental Measurement of Effective Diffusion Distance for the Sintering of Ceramics, *Journal American Ceramic Society*. 92 (2009) 1481–1486. <https://doi.org/10.1111/j.1551-2916.2009.02954.x>.
- [57] K.S. Hwang, R.M. German, E. v Lenel, Capillary Forces between Spheres during Agglomeration and Liquid Phase Sintering, *METALLURGICAL TRANSACTIONS A*. 18A (1987) 11–17. <https://link.springer.com/content/pdf/10.1007/BF02646216.pdf> (accessed August 13, 2019).
- [58] R. Tandon, R.M. German, Supersolidus-Transient Liquid Phase Sintering Using Superalloy Powders, *The International Journal of Powder Metallurgy*. 30 (1994) 435–443.
- [59] R. German, An Update on the Theory of Supersolidus Liquid Phase Sintering, 2003. <http://www.cavs.msstate.edu/publications/docs/2003/07/2003-15.pdf> (accessed July 25, 2019).
- [60] J. Kanters, U. Eisele, J. Rödel, Cosintering Simulation and Experimentation: Case Study of Nanocrystalline Zirconia, *Journal of American Ceramic Society*. 84 (2001) 2757–2763.
- [61] G. Okuma, S. Watanabe, K. Shinobe, N. Nishiyama, A. Takeuchi, K. Uesugi, S. Tanaka, F. Wakai, 3D multiscale-imaging of processing-induced defects formed during sintering of hierarchical powder packings, *Scientific Reports*. 9 (2019). <https://doi.org/10.1038/s41598-019-48127-y>.
- [62] O. Guillon, L. Weiler, J. Rödel, Anisotropic Microstructural Development During the Constrained Sintering of Dip-Coated Alumina Thin Films, *Journal of the American Ceramic Society*. 90 (2007) 1394–1400. <https://doi.org/10.1111/J.1551-2916.2007.01565.X>.
- [63] A. International, Standard Test Methods for Determining Average Grain Size, ASTM Standards E112. (2014). <https://doi.org/10.1520/E0112-13>.
- [64] I. Nettleship, Quantitative Analysis of Microstructures during Sintering, (n.d.).
- [65] N.J. SHAW, R.J. BROOK, Structure and Grain Coarsening During the Sintering of Alumina, *Journal of the American Ceramic Society*. 69 (1986) 107–110. <https://doi.org/10.1111/j.1151-2916.1986.tb04711.x>.
- [66] I. Nettleship, R. McAfee, Microstructural pathways for the densification of slip cast alumina, *Materials Science and Engineering A*. 352 (2003) 287–293. [https://doi.org/10.1016/S0921-5093\(02\)00899-7](https://doi.org/10.1016/S0921-5093(02)00899-7).

- [67] E.H. Aigeltinger, R.T. DeHoff, Quantitative determination of topological and metric properties during sintering of copper, *Metallurgical Transactions A*. 6 (1975) 1853–1862. <https://doi.org/10.1007/BF02646849>.
- [68] R.T. Whitaker, Xinwei Xue, Variable-conductance, level-set curvature for image denoising, in: *International Conference on Image Processing, IEEE*, 2001: pp. 142–145. <https://doi.org/10.1109/ICIP.2001.958071>.
- [69] G. Farin, N. Sapidis, Curvature and the Fairness of Curves and Surfaces, *IEEE Computer Graphics and Applications*. 9 (1989) 52–57.
- [70] H.-W. Shi, Y.-W. Shi, Y.-G. Yin, Food bacteria auto identification method based on image treatment, *Jilin Daxue Xuebao (Gongxueban)/Journal of Jilin University (Engineering and Technology Edition)*. 42 (2012) 1049–1053.
- [71] B. Ilkanaiv, D.B. Kearns, G. Ariel, A. Beer, Effect of Cell Aspect Ratio on Swarming Bacteria, *Physical Review Letters*. 118 (2017). <https://doi.org/10.1103/PhysRevLett.118.158002>.
- [72] F. Nellros, M.J. Thurley, H. Jonsson, C. Andersson, S.P.E. Forsmo, Automated measurement of sintering degree in optical microscopy through image analysis of particle joins, *Pattern Recognition*. 48 (2015) 3451–3465. <https://doi.org/10.1016/j.patcog.2015.05.012>.
- [73] R.J. McAfee, *A Study of Microstructural Evolution During Sintering Using Tessellation*, University of Pittsburgh, 2004.
- [74] R.J. McAfee, I. Nettleship, A Mesoscale Description of Microstructure Evolution For the Sintering of Ceramics, *Acta Materialia*. 53 (2005) 4305–4311. <https://doi.org/10.1016/j.actamat.2005.05.028>.
- [75] C.V. Howard, M.G. Reed, *Unbiased Stereology*, in: BIOS Scientific Publishers Limited, Oxford, UK, 1998: p. 231.
- [76] H. Safari, B.J. Balcom, A. Afrough, Characterization of pore and grain size distributions in porous geological samples – An image processing workflow, *Computers and Geosciences*. 156 (2021). <https://doi.org/10.1016/J.CAGEO.2021.104895>.
- [77] Z. Fang, B. Patterson, Modeling particle size distributions by the Weibull distribution function, *Mater Charact*. 31 (1993) 177–182.
- [78] D.M. Schwartz, A general method of calculating particle size distributions, *Journal of Microscopy*. 96 (1972) 25–35. <https://doi.org/10.1111/j.1365-2818.1972.tb03740.x>.

- [79] L.J. Paul, Distribution curves of sectional areas through some families of convex particles, *Journal of Microscopy*. 122 (1981) 165–172. <https://doi.org/10.1111/j.1365-2818.1981.tb01255.x>.
- [80] J. Wasén, R. Warrén, True grain size distribution of WC–Co alloy, *Materials Science and Technology*. 5 (1989) 222–226. <https://doi.org/10.1179/mst.1989.5.3.222>.
- [81] H. Bjorklund, J. Wasen, L.K.L. Falk, Quantitative Microscopy of b-Si₃N₄ Ceramics, *Journal American Ceramic Society*. 80 (1997) 3061–3069.
- [82] J.-H. Han, D.-Y. Kim, Determination of three-dimensional grain size distribution by linear intercept measurement, *Acta Materialia*. 46 (1998) 2021–2028. [https://doi.org/10.1016/S1359-6454\(97\)00442-4](https://doi.org/10.1016/S1359-6454(97)00442-4).
- [83] A. Thorvaldsen, The intercept method - 1. Evaluation of grain shape, *Acta Materialia*. 45 (1997) 587–594. [https://doi.org/10.1016/S1359-6454\(96\)00197-8](https://doi.org/10.1016/S1359-6454(96)00197-8).
- [84] A. Thorvaldsen, The intercept method - 2. Determination of spatial grain size, *Acta Materialia*. 45 (1997) 595–600. [https://doi.org/10.1016/S1359-6454\(96\)00198-X](https://doi.org/10.1016/S1359-6454(96)00198-X).
- [85] Y. Liu, R.M. German, R.G. Iacocca, Microstructure quantification procedures in liquid-phase sintered materials, *Acta Materialia*. 47 (1999) 915–926. [https://doi.org/10.1016/S1359-6454\(98\)00395-4](https://doi.org/10.1016/S1359-6454(98)00395-4).
- [86] R.M. Bevensee, *Maximum Entropy Solutions to Scientific Problems*, Englewood Cliffs, 1993.
- [87] H.J. Barba, P. Fenster, J. Gil, The use of local entropy measures in edge detection for cytological image analysis, *Journal of Microscopy*. 156 (1989) 125–134. <https://doi.org/10.1111/j.1365-2818.1989.tb02911.x>.
- [88] K.J. Woolfe, K. Michibayashi, “BASIC” entropy grouping of laser-derived grain-size data: An example from the Great Barrier Reef, *Computers and Geosciences*. 21 (1995) 447–462. [https://doi.org/10.1016/0098-3004\(94\)00092-9](https://doi.org/10.1016/0098-3004(94)00092-9).
- [89] W.E. Full, R. Ehrlich, S. Kennedy, R. Ehrlich, S. Kennedy, Optimal Definition of Class Intervals of Histograms or Frequency Plots, in: *Particle Characterization in Technology*, CRC Press, 2018: pp. 135–146. <https://doi.org/10.1201/9781351075367-11>.
- [90] C.E. Shannon, Weaver W., *The Mathematical Theory of Communication*, University of Illinois Press, Urbana, 1964.
- [91] A.C. Kak, M. Slaney, *Principles of Computerized Tomographic Imaging*, IEEE, New York, 1988.

- [92] W.R. Webb, W.E. Brant, N.M. Major, *Fundamentals of Body CT*, Elsevier Health Sciences, 2019.
- [93] D.W. Holdsworth, M.M. Thornton, Micro-CT in small animal and specimen imaging, *Trends in Biotechnology*. 20 (2002) 34–39. [https://doi.org/10.1016/S0167-7799\(02\)02004-8](https://doi.org/10.1016/S0167-7799(02)02004-8).
- [94] M. TerPogossian, *Physical Aspects of Diagnostic Radiology*, Hoeber, New York, 1968.
- [95] M.S. Kaczmarz, Approximate Solution of Systems of Linear Equations, *Bull. Intern. Acad. Polonaise Sci. Lettres*. (1937).
- [96] K. Tanabe, Projection method for solving a singular system of linear equations and its applications, *Numerische Mathematik*. 17 (1971) 203–214. <https://doi.org/10.1007/BF01436376>.
- [97] S. Brown, D.L. Bailey, K. Willowson, C. Baldock, Investigation of the relationship between linear attenuation coefficients and CT Hounsfield units using radionuclides for SPECT, *Applied Radiation and Isotopes*. 66 (2008) 1206–1212. <https://doi.org/10.1016/J.APRADISO.2008.01.002>.
- [98] C. Denison, W.D. Carlson, Three-dimensional quantitative textural analysis of metamorphic rocks using high-resolution computed X-ray tomography: Part II. Application to natural samples, *Journal of Metamorphic Geology*. 15 (1997) 45–57. <https://doi.org/10.1111/j.1525-1314.1997.00007.x>.
- [99] J.K. Jasti, G. Jesion, L. Feldkamp, Microscopic Imaging of Porous Media With X-Ray Computer Tomography, *SPE Formation Evaluation*. 8 (1993) 189–193.
- [100] K. Moritz, T. Moritz, Electrophoretically Deposited Porous Ceramics and their Characterisation by X-Ray Computer Tomography, *Key Engineering Materials*. 412 (2009) 255–260. <https://doi.org/10.4028/www.scientific.net/KEM.412.255>.
- [101] C. Jaeggi, R. Mooser, V. Frauchiger, P. Wyss, 3D characterization of open porous vacuum plasma sprayed titanium coatings by means of high resolution micro computer tomography, *Materials Letters*. 63 (2009) 2643–2645. <https://doi.org/10.1016/j.matlet.2009.09.023>.
- [102] A. du Plessis, S.G. le Roux, Standardized X-ray tomography testing of additively manufactured parts: A round robin test, *Additive Manufacturing*. 24 (2018) 125–136. <https://doi.org/10.1016/j.addma.2018.09.014>.
- [103] A. du Plessis, P. Sperling, A. Beerlink, W.B. du Preez, S.G. le Roux, Standard method for microCT-based additive manufacturing quality control 4: Metal powder analysis, *MethodsX*. 5 (2018) 1336–1345. <https://doi.org/10.1016/j.mex.2018.10.021>.

- [104] A. du Plessis, P. Sperling, A. Beerlink, W.B. du Preez, S.G. le Roux, Standard method for microCT-based additive manufacturing quality control 1: Porosity analysis, *MethodsX*. 5 (2018) 1102–1110. <https://doi.org/10.1016/j.mex.2018.10.021>.
- [105] A. du Plessis, P. Sperling, A. Beerlink, L. Tshabalala, S. Hoosain, N. Mathe, S.G. le Roux, Standard method for microCT-based additive manufacturing quality control 2: Density measurement, *MethodsX*. 5 (2018) 1117–1123. <https://doi.org/10.1016/j.mex.2018.09.006>.
- [106] A. Brueckner-Foit, I. Bacaicoa, M. Luetje, M. Wicke, A. Geisert, M. Fehlbier, 3D characterization of the fracture mechanisms of a Fe-rich Al-Si-Cu alloy, *MATEC Web of Conferences*. 165 (2018) 1–8. <https://doi.org/10.1051/mateconf/201816504006>.
- [107] R.S. Bradley, Y. Liu, T.L. Burnett, X. Zhou, S.B. Lyon, P.J. Withers, A. Gholinia, T. Hashimoto, D. Graham, S.R. Gibbon, B. Hornberger, Time-lapse lab-based x-ray nano-CT study of corrosion damage, *Journal of Microscopy*. 267 (2017) 98–106. <https://doi.org/10.1111/jmi.12551>.
- [108] D. Bernard, D. Gendron, J.M. Heintz, S. Bordère, J. Etourneau, First direct 3D visualisation of microstructural evolutions during sintering through X-ray computed microtomography, *Acta Materialia*. 53 (2005) 121–128. <https://doi.org/10.1016/j.actamat.2004.09.027>.
- [109] A. Vagnon, J.P. Rivière, J.M. Missiaen, D. Bellet, M. Di Michiel, C. Josserond, D. Bouvard, 3D statistical analysis of a copper powder sintering observed in situ by synchrotron microtomography, *Acta Materialia*. 56 (2008) 1084–1093. <https://doi.org/10.1016/j.actamat.2007.11.008>.
- [110] L. Olmos, T. Takahashi, D. Bouvard, C.L. Martin, L. Salvo, D. Bellet, M. Di Michiel, Analysing the sintering of heterogeneous powder structures by in situ microtomography, *Philosophical Magazine*. 89 (2009) 2949–2965. <https://doi.org/10.1080/14786430903150225>.
- [111] F. Wakai, O. Guillon, Evaluation of sintering stress from 3-D visualization of microstructure: Case study of glass films sintered by viscous flow and imaged by X-ray microtomography, *Acta Materialia*. 66 (2014) 54–62. <https://doi.org/10.1016/j.actamat.2013.11.070>.
- [112] C. Zheng, A. Mostafaei, P.R. de Vecchis, I. Nettleship, M. Chmielus, Microstructure evolution for isothermal sintering of binder jet 3D printed alloy 625 above and below the solidus temperature, *Additive Manufacturing*. 47 (2021) 102276. <https://doi.org/10.1016/j.addma.2021.102276>.
- [113] A. Mostafaei, Powder bed binder jet 3D printing of Alloy 625: Microstructural evolution, densification kinetics and mechanical properties, University of Pittsburgh, 2018.

- [114] A. Mostafaei, J. Toman, E.L. Stevens, E.T. Hughes, Y.L. Krimer, M. Chmielus, Microstructural evolution and mechanical properties of differently heat-treated binder jet printed samples from gas- and water-atomized alloy 625 powders, *Acta Materialia*. 124 (2017) 280–289. <https://doi.org/10.1016/j.actamat.2016.11.021>.
- [115] Metallography and Microstructures of Nonferrous Alloys, in: *ASM Handbook Volume 9: Metallography and Microstructures*, 2004: pp. 711–751.
- [116] M.R. Stoudt, E.A. Lass, D.S. Ng, M.E. Williams, F. Zhang, C.E. Campbell, G. Lindwall, L.E. Levine, The Influence of Annealing Temperature and Time on the Formation of δ -Phase in Additively-Manufactured Inconel 625, *Metall Mater Trans A Phys Metall Mater Sci*. 49 (2018). <https://doi.org/10.1007/s11661-018-4643-y>.
- [117] A. Mostafaei, P. Rodriguez De Vecchis, I. Nettleship, M. Chmielus, Effect of powder size distribution on densification and microstructural evolution of binder-jet 3D-printed alloy 625, *Materials and Design*. 162 (2019) 375–383. <https://doi.org/10.1016/j.matdes.2018.11.051>.
- [118] J. Schindelin, I. Arganda-Carreras, E. Frise, V. Kaynig, M. Longair, T. Pietzsch, S. Preibisch, C. Rueden, S. Saalfeld, B. Schmid, J.-Y. Tinevez, D.J. White, V. Hartenstein, K. Eliceiri, P. Tomancak, A. Cardona, Fiji: an open-source platform for biological-image analysis, *Nature Methods*. 9 (2012) 676–682. <https://doi.org/10.1038/nmeth.2019>.
- [119] M.J. Cieslak, T.J. Headley, T. Kollie, A.D. Romig, A Melting and Solidification Study of Alloy 625, 19A (1988). <https://link.springer.com/content/pdf/10.1007/BF02645056.pdf> (accessed August 25, 2019).
- [120] D. Ulrich, B. van Rietbergen, A. Laib, P. Rueggsegger, R. Rueggsegger, The Ability of Three-Dimensional Structural Indices to Reflect Mechanical Aspects of Trabecular Bone, *Bone*. 25 (1999) 55–60.
- [121] I.F. Sbalzarini, P. Koumoutsakos, Feature point tracking and trajectory analysis for video imaging in cell biology, *Journal of Structural Biology*. 151 (2005) 182–195. <https://doi.org/10.1016/j.jsb.2005.06.002>.
- [122] R Core Team, R: A language and environment for statistical computing., (2021).